INSTITUT OBERFLÄCHENTECHNIK

Lehrstuhl für Oberflächentechnik im Maschinenbau
Rheinisch-Westfälische Technische Hochschule Aachen
Prof. Dr.-Ing. K. Bobzin

Towards Digital Shadow in Plasma Spraying

Seyed Ruhollah Dokhanchi

Oktober 2023

Schriftenreihe Oberflächentechnik, Band 74

Hrsg.: Prof. Dr.-Ing. K. Bobzin

Partner im
LABORATORIUM
FÜGETECHNIK
OBERFLÄCHENTECHNIK

RWTH AACHEN UNIVERSITY

Towards Digital Shadow in Plasma Spraying

Auf dem Weg zum Digitalen Schatten im Plasmaspritzen

Von der Fakultät für Maschinenwesen der Rheinisch-Westfälischen Technischen Hochschule Aachen zur Erlangung des akademischen Grades eines Doktors der Ingenieurwissenschaften genehmigte Dissertation

vorgelegt von

Seyed Ruhollah Dokhanchi

Berichter/in: Univ.-Prof. Dr.-Ing. Kirsten Bobzin

Univ.-Prof. Dr.-Ing. Thomas Bergs

Tag der mündlichen Prüfung: 08.08.2023

Schriftenreihe Oberflächentechnik

Band 74

Seyed Ruhollah Dokhanchi

Towards Digital Shadow in Plasma Spraying

Shaker Verlag
Düren 2023

Bibliographic information published by the Deutsche Nationalbibliothek
The Deutsche Nationalbibliothek lists this publication in the Deutsche Nationalbibliografie; detailed bibliographic data are available in the Internet at http://dnb.d-nb.de.

Zugl.: D 82 (Diss. RWTH Aachen University, 2023)

Printed in Germany.

ISBN 978-3-8440-9268-4
ISSN 1864-0796

Shaker Verlag GmbH • Am Langen Graben 15a • 52353 Düren
Phone: 0049/2421/99011-0 • Telefax: 0049/2421/99011-9
Internet: www.shaker.de • e-mail: info@shaker.de

A Dedication to My Mother

تقدیم به مادرم

Acknowledgment

First and foremost, I would like to express my gratitude to Prof. Kirsten Bobzin for the fascinating research topic and the opportunity to pursue my doctoral studies at the Surface Engineering Institute (IOT) at RWTH Aachen University. I extend my heartfelt thanks to Prof. Thomas Bergs for agreeing to be the second reviewer for my dissertation. I would like to convey my appreciation to Prof. Carlo Holly for serving as the chair of the examination committee.

This dissertation was completed during my tenure as a research assistant in the Thermal Spraying research group at IOT. The results presented in this work stem from the research projects "CoE-IoP - Cluster of Excellence; Internet of Production" and "TS-Footprint - Development of a Method for In-situ Determination of Deposition Efficiency in Thermal Spraying". I am grateful to the German Research Foundation (DFG) for the financial support of these projects.

I extend my thanks to the former and current chief engineers and team leaders, Dr. Mehmet Öte, Dr. Wolfgang Wietheger, Hendrik Heinemann, and Dr. Martin Knoch, for their guidance and motivation during my academic journey at IOT. Their mentorship and encouragement were instrumental in shaping my research path. I am particularly grateful to Dr. Lidong Zhao for his wealth of knowledge and profound insights shared during our discussions, which significantly enriched my understanding of the subject matter. I am thankful to Metin Yüceer for not only providing crucial support during the experiments conducted in this work but also for the delightful tea breaks that provided moments of respite and inspiration.

I would like to express my sincere gratitude to Dr. Martin Knoch, Andreas Schacht, Hendrik Heinemann, Elisa Burbaum, Marvin Schulz, and Dr. Ilkin Alkhasli for their substantial contributions, whether it was in meticulous proofreading of my dissertation or offering invaluable ideas and corrections for my doctoral presentation. Their input was crucial in refining my work. I extend my warmest thanks to Lukas Johann, Kevin Jasutyn, Carsten Vogels, Katja Radermacher, and Jessica Görtz for engaging in instructive scientific discussions. To all my current and former colleagues at IOT, I express my heartfelt appreciation for their invaluable assistance with experimental, administrative, or IT-related matters. I also want to thank them for the stimulating conversations, which covered both scientific and non-scientific topics. Together, we fostered a collaborative and friendly atmosphere that I deeply cherish.

I am eternally grateful to my beloved family, Dr. Hossein Dokhanchi, Dr. Zeinab Dokhanchi, and Dr. Najmeh Dokhanchi, for their unwavering support in both my academic and personal life. My deepest and most special gratitude goes to the cornerstone of my life, my mother, for all the sacrifices she has made for me. Without her invaluable support, I would not have achieved this milestone. I dedicate this work wholeheartedly to my mother.

Abstract

Atmospheric Plasma Spraying (APS) is a versatile coating technology, which offers a broad range of functional features. Deposition efficiency (DE) is a major performance measure in APS, which is determined by dozens of intrinsic and extrinsic influencing factors. Because of the nonlinear and complicated interdependencies of the contributing variables, enhancing DE has always been a challenging task in the process development of APS. Hence, employing an ensemble of computer-aided methods is inevitable to understand and control these correlations in such a complex coating technology. The concept of the so-called *Digital Shadow* combines domain-specific models with data-driven techniques of Artificial Intelligence (AI), inferred by autonomous agents to create a sufficiently accurate image of the production process including all relevant data. This dissertation is devoted to the development of the primary steps towards a Digital Shadow in APS with the ultimate goal of improving the process efficiency.

Modern AI methods, namely Support Vector Machine (SVM) and Adaptive Neuro-Fuzzy Inference System (ANFIS), were used in this work to predict DE. For this purpose, both simulation and experimental data from the entire process chain of APS were employed to train the AI models, and combine them in the frame of an expert system. These data include process parameters, in-flight particle properties and DE on the substrate.

The developed expert system consists of two subsystems: one for predicting in-flight particle properties from process parameters using SVM technique and another for predicting DE from particle properties using ANFIS. To tackle the problem of insufficient data for training the aforementioned AI models two approaches were pursued: 1) A method was developed for in situ determination of spatially resolved deposition efficiencies on the substrate, namely Local Deposition Efficiency (LDE). By using LDE, sufficient amount of data for learning algorithms could be generated, while providing that much data for ex situ measurements of global DE and their corresponding particle properties would be impractical. 2) Simulation data for the in-flight particle properties were generated by using the simulation models of the plasma jet already developed at IOT. The combination of these two strategies provided the aggregated and purpose driven data sets required for a Digital Shadow in APS. The developed expert system can be used as a tool to adjust the process parameters to produce sustainable and cost-effective coatings, and subsequently improves the integration of coating process into production chain.

Zusammenfassung

Atmosphärisches Plasmaspritzen (APS) ist eine vielseitige Beschichtungstechnologie, die ein breites Spektrum an funktionellen Eigenschaften bietet. Der Auftragswirkungsgrad (DE) ist ein wichtiges Leistungsmerkmal des APS, das durch Dutzende von intrinsischen und extrinsischen Einflussfaktoren bestimmt wird. Aufgrund der nichtlinearen und komplizierten Wechselwirkungen zwischen den Einflussgrößen stellt die Verbesserung der DE eine große Herausforderung bei der Prozessentwicklung des APS dar. Daher ist der Einsatz eines Ensembles computergestützter Methoden unumgänglich, um diese Zusammenhänge in einer derart komplexen Beschichtungstechnologie zu verstehen und zu kontrollieren. Das Konzept des so genannten *Digitalen Schattens* kombiniert domänenspezifische Modelle mit datengetriebenen Techniken der Künstlichen Intelligenz (KI), die von autonomen Agenten abgeleitet werden, um ein hinreichend genaues Abbild des Produktionsprozesses einschließlich aller relevanten Daten zu erstellen. Diese Dissertation widmet sich der Entwicklung der primären Schritte in Richtung eines Digitalen Schattens im APS mit dem Hauptziel der Verbesserung der Prozesseffizienz.

Moderne KI-Methoden, nämlich Support Vector Machine (SVM) und Adaptive Neuro-Fuzzy Inference System (ANFIS), wurden in dieser Arbeit verwendet, um DE vorherzusagen. Zu diesem Zweck wurden sowohl Simulations- als auch experimentelle Daten aus der gesamten Prozesskette des APS verwendet, um die KI-Modelle zu trainieren und sie im Rahmen eines Expertensystems zu kombinieren. Diese Daten umfassen Prozessparameter, Partikeleigenschaften und die DE auf dem Substrat. Das entwickelte Expertensystem besteht aus zwei Teilsystemen: A) Vorhersage der Partikeleigenschaften im Flug aus den Prozessparametern unter Verwendung der SVM-Technik und B) Vorhersage der DE aus den Partikeleigenschaften mittels ANFIS. Um das Problem der unzureichenden Daten für das Training der KI-Modelle zu lösen, wurden zwei Ansätze verfolgt: 1) Es wurde eine Methode zur In-situ-Bestimmung räumlich aufgelöster DE auf dem Substrat, nämlich Local Deposition Efficiency (LDE), entwickelt. 2) Simulationsdaten für die Partikeleigenschaften wurden durch die Verwendung der bereits am IOT entwickelten Simulationsmodelle des Plasmastrahls erzeugt. Die Kombination dieser beiden Strategien lieferte die aggregierten und zweckgebundenen Datensätze, die für einen Digitalen Schatten im APS benötigt werden. Das entwickelte Expertensystem kann als Werkzeug zur Anpassung der Prozessparameter verwendet werden, um nachhaltige und kosteneffiziente Beschichtungen zu erzeugen, und verbessert somit die Integration des Beschichtungsprozesses in die Produktionskette.

Table of Contents

1 Introduction

Thermal Spraying (TS) is a coating technology in which the feedstock material is introduced into a high-temperature free jet to deposit a coating. The resultant molten or semi-molten particles are accelerated in the free jet towards a prepared substrate and their successive impingements build a coating with a typical thickness of 50 µm < $d_{coating}$ < 400 µm [Bob13]. TS is considered as the most versatile coating technology due to its numerous process variants, which enable the deposit of a wide range of feedstock materials. Metals and metal alloys, oxide and nonoxide ceramics, plastics, cermets and composites can be applied using diverse process variants of TS. Furthermore, TS offers a broad range of functional features including wear, oxidation and corrosion resistance as well as electrical and thermal insulation. Other special characteristics of this coating technology include equipment portability, wide range of coating thicknesses and minimal thermal degradation to substrate [Dav04].

The quality of a thermally sprayed coating can be evaluated, among others, through the following coating properties with regard to a given application: thickness, thermal conductivity, tensile bond strength between the coating and the substrate, surface roughness and coating hardness, porosity and oxide content. To provide an example, porosity is discussed below as one of the most important coating properties. Porosity has its advantages and disadvantages depending on the functionality of the coating. For example, the thermal barrier coatings must have a low thermal conductivity and consequently a relatively high porosity in the range of 10-20 % [BV17]. In the tribological field, the open pores, e.g. on the inner walls of the plain bearings or cylinder bores, act as microcavities that can store lubricants. This additional oil retention improves the frictional behavior of the components. On the contrary, the corrosion or wear-resistant coatings must have a low porosity or, ideally, a porosity close to zero. In this case, porosity is considered as an inherent defect for the coating.

TS-processes are categorized according to the type of the energy source. Atmospheric plasma spraying (APS) represents one of the most important process variants of TS, in which an electric arc discharge inside a plasma generator is used as the energy source for heat generation and acceleration of the process gas [FMV+06]. One or more direct current (dc) arcs superheat an inert gas, commonly argon or an argon-hydrogen mixture, to generate the plasma.

The operating principle of a multi-arc APS process, which is the focus of this work, is depicted in Figure 1-a. Process temperatures in the plasma jet core can range roughly between 6,000 °C < T_g < 15,000 °C [Dav04], allowing the processing of high-melting ceramic materials in particular. Feedstock material in form of powder is introduced into the plasma jet via an inert carrier gas inside a hose following a particle injector. The size of the injected particles are typically in the range of 20 µm < D_p < 90 µm and the particle velocities can reach up to v_p = 800 m/s [Paw08]. A cross-section of an Al_2O_3 coating is depicted in Figure 1-b. The coating microstructure is made up of deposited particles that produce the conventional lamellae shape by deforming to different extents. Immediately after impact on the substrate, the heated particles spread out, deform and solidify. The main adhesion mechanism of sprayed coatings is referred to as mechanical interlocking. This is defined as the mechanical anchorage of the splats to irregularities of the substrate by the force arising from liquid shrinkage [Paw08]. These irregularities result from grit blasting of the substrate as a pre-spray surface preparation.

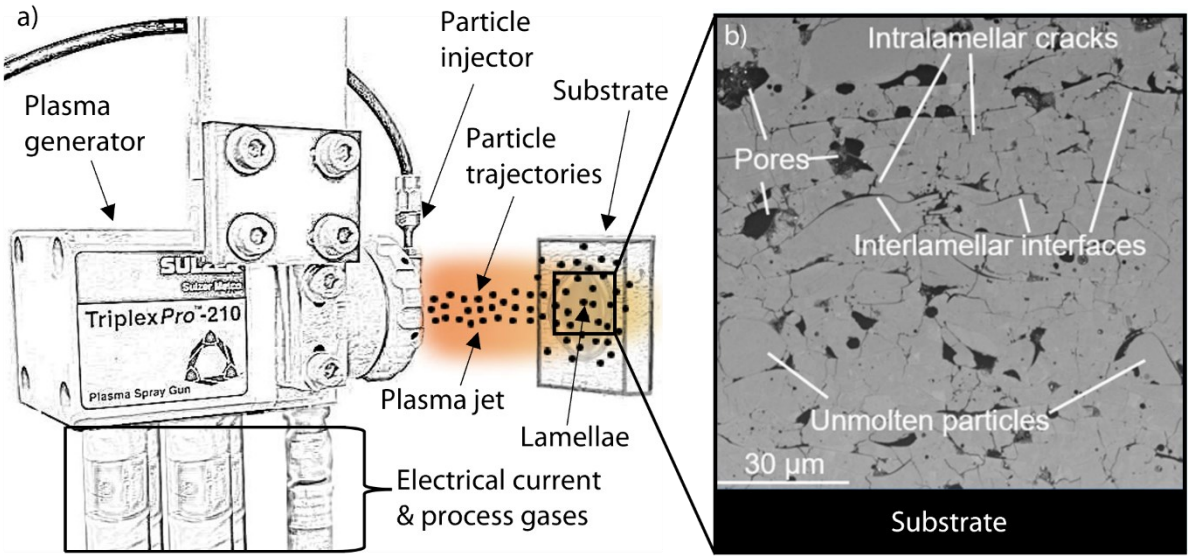

Figure 1: a) Schematic illustration of the APS process and b) cross-section image of an Al_2O_3 coating applied with the APS process

Dc plasma arc spraying systems are one of the most flexible and at the same time sophisticated variants of TS-processes [Dav04]. The complexity of plasma spraying is related not only to the manufacturing of the plasma guns for the harsh environment of high temperatures and enthalpies, but also to the enormous quantity and diversity of the influencing factors. These

influencing factors result from the combination of intrinsic and extrinsic parameters. The directly adjustable extrinsic parameters include, for instance, the electrical current and the volume flow rates of the process gases. The resulting intrinsic parameters, such as in-flight particle velocities and temperatures, can only be influenced indirectly [SBD+06]. All these parameters are interrelated and usually follow nonlinear relationships. For example, the variation of the current or the process gas flow to change the particle temperatures and velocities at impact, also generally requires adjusting the parameters for injection the feedstock material to obtain thermally and kinematically matched parameters. Moreover, the parameter combinations are also influenced by disturbance variables, such as fluctuations of the arc or the wear of the system components, e.g. electrodes and injectors.

A large number of overviews of the influencing variables in plasma spraying are available in the literature. A comprehensive list of the main setting parameters is given by Lugscheider [Lug02], see Table 1. In this table, some of these parameters with their direct influences on the different parts of the APS system are listed. These are only the main parameters that must be controlled and recorded in practice during plasma spraying. If the peripheral influencing variables such as torch travel speed, substrate variables, feedstock material influences, etc. are added, the overall number of influencing factors in APS is estimated to be more than 200 [Lug02]. It should be emphasized that the intricate nonlinear relationships among these factors further increase the complexity of the overall APS system. Taking the above aspects into account, the question of robust methods for quantifying the complex interactions between the dozens of influencing factors in APS arises. It turns out that computer-aided algorithms can best fulfill this challenging undertaking.

Table 1: Adjustable parameters in plasma spraying (without peripheral influences) according to [Lug02]

Area	Parameter	Direct influence on
Nozzle (Anode)	▪ Nozzle diameter ▪ Nozzle length ▪ Nozzle shape	▪ Plasma velocity ▪ Arc length, plasma energy ▪ Plasma velocity, plasma temperature
Powder injection	▪ Injector diameter ▪ Number of injectors ▪ Injector position, injector angle ▪ Powder feed rate ▪ Powder carrier gas flow	▪ Max. flow rate, particle trajectories ▪ Max. flow rate ▪ Particle trajectories ▪ Max. Particle melting ▪ Particle trajectories
Power	▪ Arc current intensity ▪ Arc voltage	▪ Plasma energy, viscosity ▪ Plasma energy, viscosity
Plasma gases	▪ Gas composition ▪ Gas flows ▪ Gas pressures ▪ Angle of swirl	▪ Plasma enthalpy, thermal conductivity, viscosity ▪ Plasma energy ▪ Plasma velocity ▪ Arc and plasma swirl ⇒ nozzle lifetime, particle injection
Cooling power	▪ Coolant flow rate ▪ Coolant inlet temperature and pressure	▪ Torch efficiency ▪ Torch service life
Spray distance	Spray distance	Particle velocity and temperature, Substrate heating
Atmosphere	Pressure	Plasma energy density, Plasma velocity

The term "*Industrie 4.0*", since its introduction as the fourth industrial revolution by a team of scientists in Germany, has been used increasingly for all kinds of fundamental concepts that are related to the digital transformation in production [LFK+14]. Industrie 4.0 offers the potential for technical system networking and real-time optimization of complex value-added systems based on big data processing, and consequently forecasting the future events in production. This is what is truly revolutionary about Industrie 4.0, and not the digitization of products and their production per se. The processing of big data became possible by the rapid expansion of computer resources, specifically High-Performance Computing (HPC), which largely contributed the development of Industrie 4.0. The fourth industrial revolution has also brought innovation and competition back to engineers and managers in the production workplace. The networking of supply chains on the basis of digital technologies and the resulting changes in supply chain systems represent a major paradigm shift for all production managers. Wrong decisions due to a lack of information and inadequate assessment of risks and technology potentials can lead to massive competitive disadvantages and endanger the long-term existence of the companies concerned.

The main focus of Industrie 4.0 is on integrating cyber-physical production systems (CPPS) with processes and stakeholders along the whole value-added chain [BDJ+22]. Thereby, Industrie 4.0 can be facilitated by CPPS, depending on the most recent and foreseeable advancements in computer science, information and communication technologies, and manufacturing science and technology. CPPS consist of autonomous and cooperative elements and subsystems that interact with each other depending on the situation, across all levels of production, from processes to machines to humans and logistic networks [Mon14]. The main issue is to investigate the connections between autonomy, cooperation, optimization, and responsiveness. This makes the integration of simulation-based and analytical methodologies more important than before. The simulation permits dynamic investigation of production systems and supports in both operational and strategic planning [ULS17].

The concept of "*Digital Twin*" (DT) is one of the most promising enablers of smart manufacturing as well as realization of CPPS and subsequently Industrie 4.0 [TZL+19]. DT is referred to as a virtual or computerized representation of a physical entity, which may be a product or a process, including all the data and information that tie the physical entity and its twin together [BCF19]. This digital replication occurs mainly by integration of the Artificial

Intelligence (AI) methods, with the aim of system optimization, controlling and monitoring, maintenance as well as prediction.

A DT is far more than just pure data, a simple model or simulation. The difference lies in the level of data integration between the physical and its digital counterpart. Digital representations can range from fully integrated with real-time data exchange to manually modeled ones that are not related to any physical objects. A basic digital model, for instance, is a digital representation of a current or future physical entity that does not include any automated data exchange. However, in the context of DT the data and information are continuously exchanged and updated, so if the state of the physical object changes, the state of the digital object will correspondingly alter, and vice versa [KKT+18]. Hence, a DT is a living, intelligent and evolving counterpart of a physical entity [BCF19]. Additionally, the proposed virtual-physical coupling requires a method to uniquely identify the physical product in order to enable a one-to-one (bijective) connection between the DT and its physical counterpart. Therefore, each DT is linked to its physical twin through a unique key [RHO+15].

Due to the enormous amounts of data that a virtual copy of a product, machine or production facility would require, developing a complete DT is typically not practical. Hence, the Digital Twins that are utilized in practice, are mostly collections of many data sets and models, each of which represents a distinct feature of the real object, rather than being complete digital replicas [BDJ+22]. Beside the concept of DT, the term "*Digital Shadow*" (DS) has been often used in the context of the Industrie 4.0. According to the definition of Schuh et al. [SBR+16, SWL+16], Digital Shadow describes a sufficiently accurate representation of key data involved in various areas such as production technology and order processing. The main difference between DS and DT lies in the level of data integration, in a way that DS has an automated one-way data flow from the existing physical object to its digital object [KKT+18]. In the context of DS, a change in the state of the physical object results into a state change in the digital object, but not vice versa, see Figure 2. Hence, DT extends the definition of DS by automatically influencing the physical object as well [BBD+21].

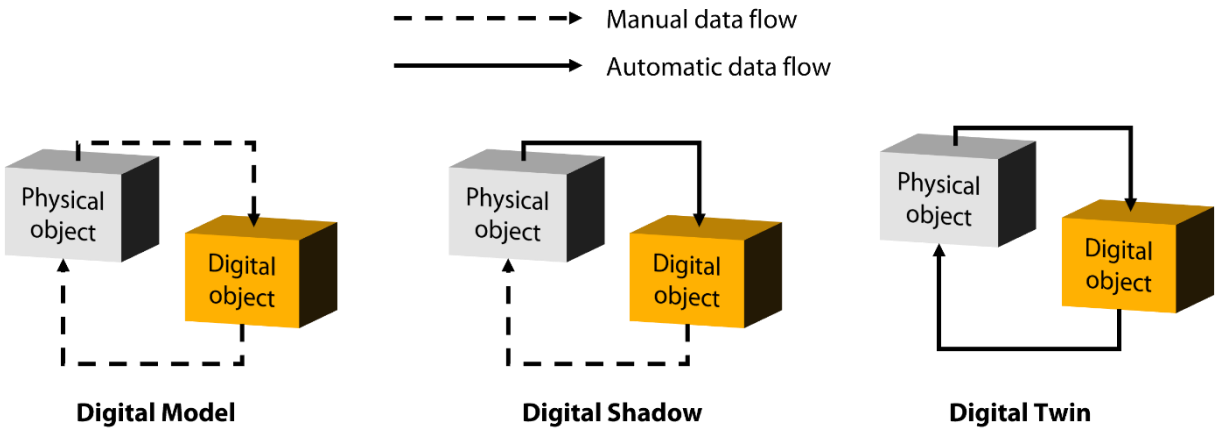

Figure 2: Data flow in a Digital Model, a Digital Shadow and a Digital Twin according to [KKT+18]

In the context of manufacturing technology, DS combines domain-specific models with data-driven AI techniques inferred by autonomous agents to create a sufficiently accurate image of the production processes including all relevant data [BGA+21, BDJ+22]. DS is considered as a suitable solution for production engineering applications, since multi-modal views with task-specific granularity can provide higher performance than a fully integrated DT [BDJ+22].

Figure 3 shows the sequential steps of the road map towards Digital Shadows for enterprises according to [SWL+16]. Since the Digital Shadow is to be designed depending on the given production environment, the migration path takes place in a circular manner and has to be retraced when the environment changes. These steps can be structured overall to four research fields: 1) create data structure/data model, 2) multimodal data acquisition, 3) multimodal data fusion and 4) consistency/plausibility check [SBR+16]. The road map begins with the definition of the goal of Digital Shadows and leads up to implementation and continuous data collection.

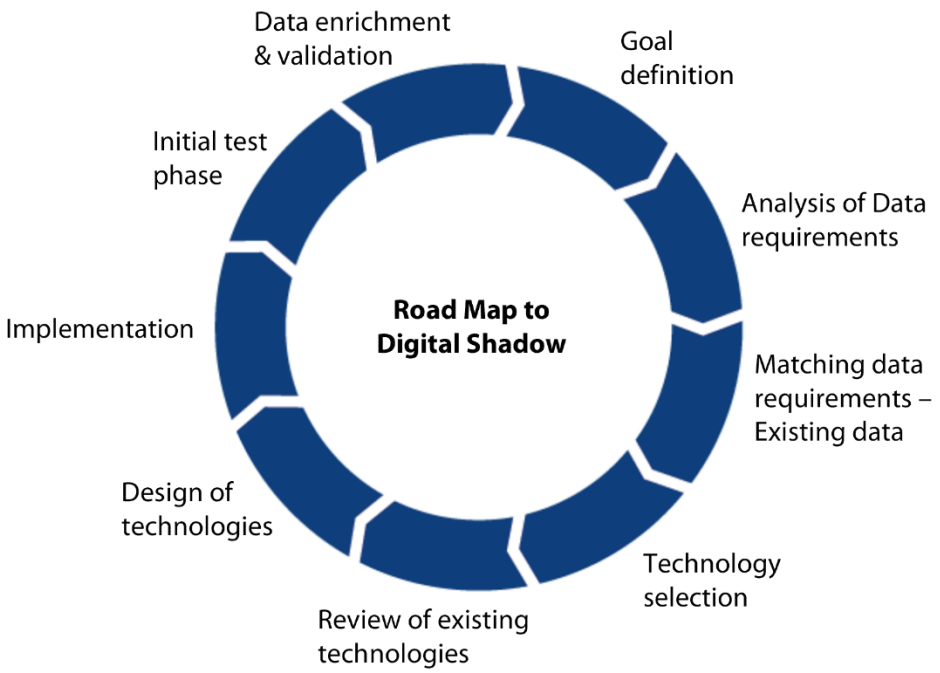

Figure 3: Road map to Digital Shadow according to [SWL+16]

As a first step, it is necessary to specify the objectives of the Digital Shadow before initiating any action involving data collecting. For instance, the objective of a DS can be increasing the energy efficiency of a production system. Based on the goal definition, the analysis of the required data takes place in the second step. For this purpose, among other things, the appropriate data granularity and the required data format must be determined. Then it must be checked which data already exist and which must be newly included. The existing and required data must be examined with regard to their scope and the required format.

Selection of appropriate technologies to collect the necessary data for each designated data point is crucial in accordance with the multimodal data acquisition. Granularity, frequency, data format, interfaces of data acquisition technology, etc. can all be used as selection factors. A unified general concept is desired when a variety of technologies are feasible. It is also necessary to assess the technologies that have previously been implemented, if any, in terms of their applicability and integration into a coherent overall concept. Furthermore, an operational design must be created before the chosen technology concept can be launched. After new technologies have been implemented, it must be checked whether they correctly supply and store the predefined data. To reduce the effort of this initial test phase, a suitable sample has to

be defined depending on the goal of the DS. After a successful test phase, the developed DS is continuously transferred to productive operation. In this final step, DS must be validated in terms of satisfying the requirements, for example by checking the continuous collection of data at the defined data points and its storage according to specifications. If necessary, the available data can be enriched by purposeful generation of new data in order to improve the performance of the developed DS. In the event that modifications are made to the production environment, such as adjustments to the production line or programmable logic controllers (PLCs), the road map needs to be repeated again, beginning with the goal definition.

With respect to the aforementioned definitions, this dissertation is devoted to the development of Digital Shadows in plasma spraying with the ultimate goal of improving the process efficiency. To this end, modern AI methods were used to develop and combine domain-specific models using simulation and experimental data from the entire process chain of APS. These data include machine or process parameters, in-flight particle properties and deposition efficiency on the substrate. Furthermore, to tackle the problem of insufficient data for AI models two approaches were pursued: 1) A methodology for in situ determination of spatially resolved deposition efficiencies on the substrate and 2) generating simulation data by using the simulation models of the plasma jet developed at the Surface Engineering Institute (IOT) at the RWTH Aachen University. The combination of these two strategies provided the aggregated and purpose-driven data sets required for Digital Shadows in plasma spraying.

2 Theory and State of the Art

This chapter describes the theory and the state of the art of the prerequisite stages for digital transformation in plasma spraying in view of improving process efficiency. It starts with section 2.1 about an introduction to Artificial Intelligence. In section 2.2, the use of AI methods for process control or quality prediction in APS is reviewed. The development of sensors in thermal spraying for in-flight particle diagnostic measurements is then covered in section 2.3 as a crucial intermediate stage of the coating process. Following that, section 2.4 gives an overview of the current state of the art for determining deposition efficiency. A summary is provided at the end of this chapter.

2.1 Introduction to Artificial Intelligence

There is no universally accepted definition for Artificial Intelligence in the literature, because both the terms "*artificial*" and "*intelligence*" are not well defined and understood in this context. Many researchers have attempted to provide a robust definition for AI [RN16]. Among these, the definition by Elaine Rich [Ric87] has received the most attention, since it avoids the philosophical issues that dominate the attempts to define the meaning of either *artificial* or *intelligence*:

"Artificial Intelligence is the study of how to make computers do things at which, at the moment, people are better."

This definition by Rich briefly characterizes what AI researchers have been doing until now and it will be probably up to date even in future. As an example, a person entering an unknown room recognizes the environment within fractions of a second and, if necessary, makes decisions and takes actions very quickly. So far, this task is too challenging for autonomous robots [Ert11]. Therefore, with respect to Rich's definition, this is a task for AI.

Machine Learning (ML) is the central sub-discipline of AI. It is applicable in complex tasks that involve lots of data and many variables, but for which no formula or equation exists. Then, ML is utilized to generate an evaluation function that is as close as possible to optimal with an iterative process [Ert11]. Machine learning uses generally two types of techniques: supervised learning and unsupervised learning. The objective of supervised learning is to find a mapping from the inputs to outputs whose correct values, namely targets, are provided by a supervisor.

Then, the learned model on known input and output data, namely training data, can predict future outputs. In unsupervised learning, there is no such supervisor, so we only work with input data. The goal of unsupervised learning is to find hidden patterns or intrinsic structures in input data. Supervised learning uses *classification* and *regression* techniques to develop predictive models, while unsupervised learning uses *clustering* techniques to group or interpret the input data [Alp10]. This work deals with supervised learning techniques for regression, since its focus is on development of prediction models based on the provided training data. There are dozens of ML algorithms, each of which takes a different approach for learning. There is no general or best method that is fitted for all cases. Therefore, choosing the right algorithm often requires trading one criterion for another, such as model speed, accuracy and complexity. Figure 4 shows an overview of some machine learning techniques.

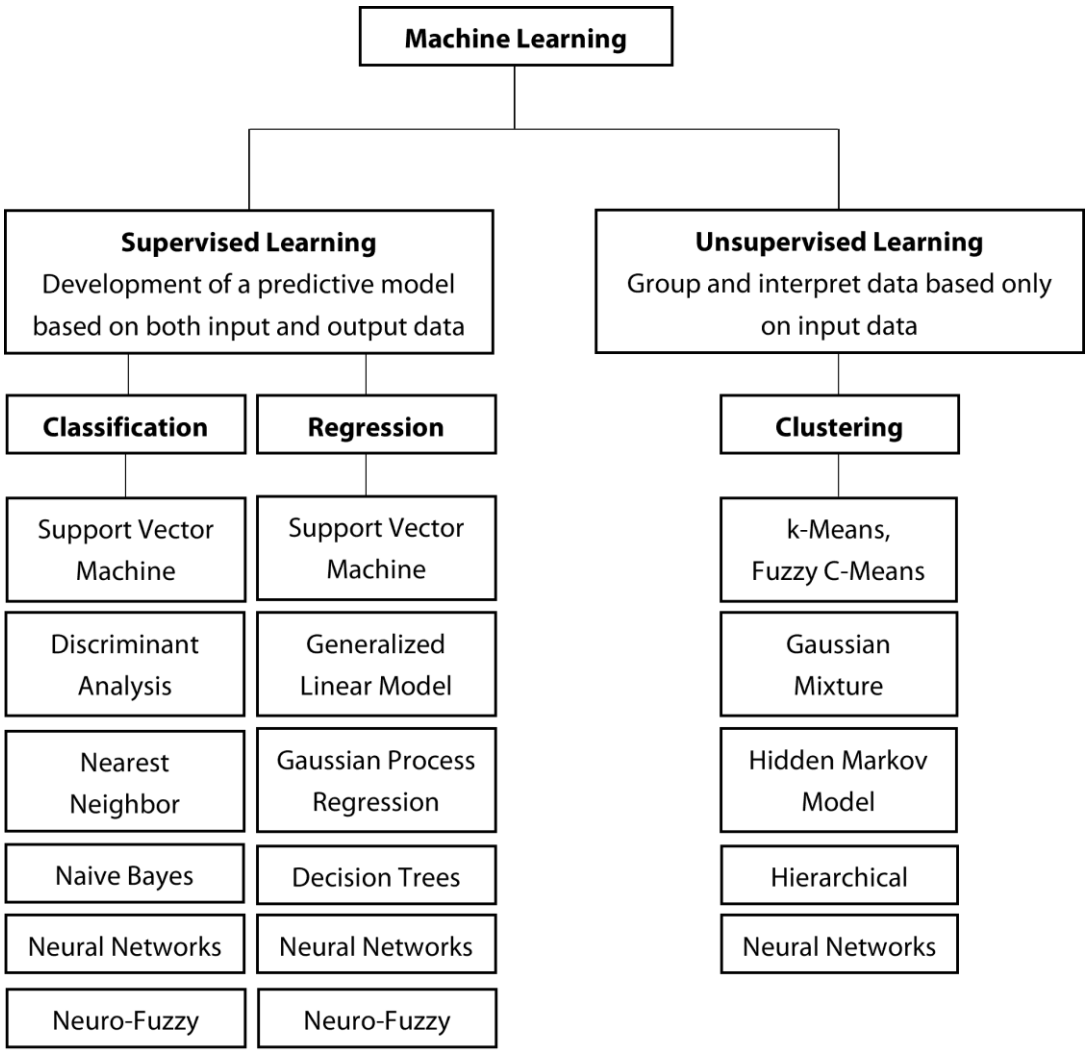

Figure 4: Overview of some machine learning techniques according to [NN23a]

2.1.1 Artificial Neural Networks (ANNs)

ANNs are inspired from the biological architecture of the human brain, which consists of billions of nerve cells or neurons that are connected in a network-like fashion. The neurons and their connections in the brain are responsible for consciousness, associations, thoughts and learning ability. The biological network served as inspiration for mathematical modeling of information processing. Figure 5 shows the schematic architecture of the a) biological neural networks and b) artificial neural networks. ANNs are considered as one of the most significant subsets of ML that can be used for both supervised and unsupervised learning techniques. McCulloch and Pitts [MP43] pioneered this subject in 1940s by presenting a mathematical model of biological nervous systems. Interested readers may refer to [ARP88] for a complete historical evolution of ANNs.

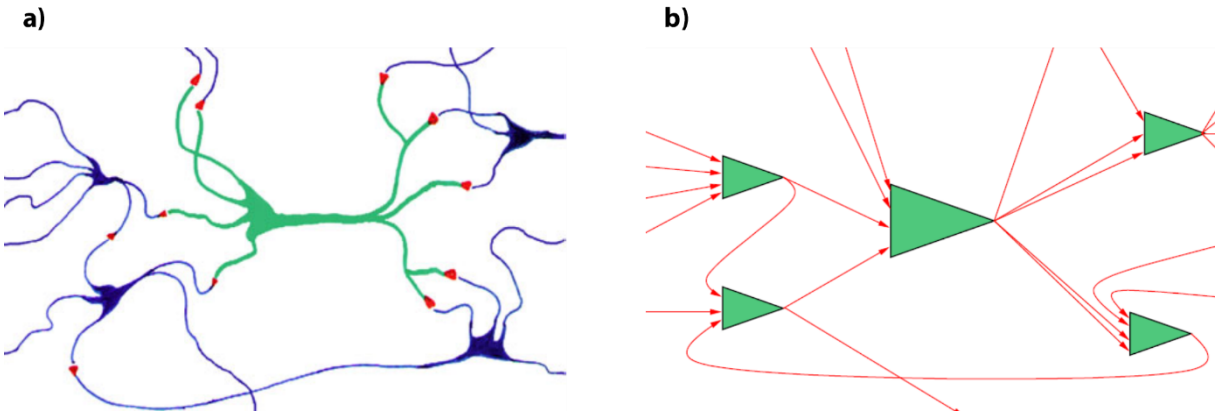

Figure 5: Schematic illustration of a) biological neural networks and b) artificial neural networks [Ert11]

ANNs are composed of some information-processing units called neurons or nodes. The computational model of a neuron labeled with k is presented as a block diagram in Figure 6. An artificial neuron receives inputs from other neurons at its entrance. Each input is associated with a numeric weight, which determines the strength of its connection link. The neuron is either activated or remains inactive depending on its total weighted input [Kro08]. The activation level of the neuron is the output generated by the activation function.

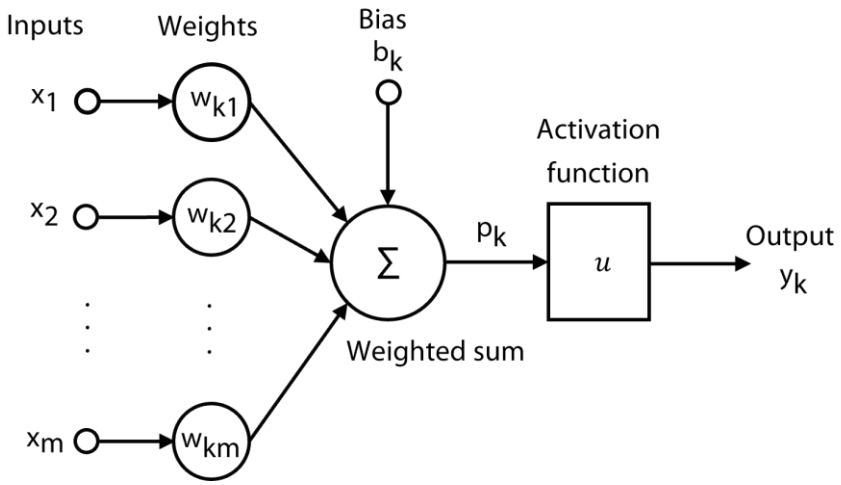

Figure 6: Block diagram of the computational model of a neuron labelled with k [Hay09]

The neural model presented in Figure 6 also contains an externally induced bias that is denoted by b_k. The bias b_k causes the net input of the activation function to be increased or decreased depending on whether it is positive or negative respectively. In mathematical terms, this neural model can be described by the pair of equations

$$p_k = \sum_{j=1}^{m} w_{kj}\, x_j + b_k \qquad \text{Eq. 1}$$

and

$$y_k = u\,(p_k). \qquad \text{Eq. 2}$$

- p_k Induced local field or activation potential of neuron k
- $x_1, x_2, \ldots, x_m$ Neuron inputs
- $w_{k1}, w_{k2}, \ldots, w_{km}$ Neuron weights
- b_k Bias parameter
- y_k Neuron output
- u Activation function

The first subscript in w_{kj} in Eq. 1 refers to the neuron in question, and the second subscript refers to the input to which the weight corresponds [Hay09]. The activation function can be linear or nonlinear. Some possibilities for the activation function are depicted in Figure 7.

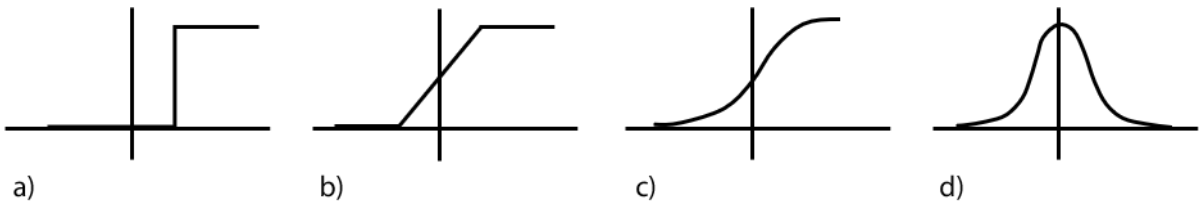

Figure 7: Different examples for activation functions: a) threshold, b) piecewise linear, c) sigmoid, and d) Gaussian [JMM96]

Two or more of the neurons described above can be joined in a layer, and a network may comprise one or more such layers. The network gains knowledge from its environment through a learning process. The connection strengths between neurons, known as synaptic weights, are responsible to store the gained knowledge. The capability of learning is central to the theory of neural networks. The structure of neurons in a neural network is tied closely to the learning algorithm used to train the network. ANNs can be divided into two main categories in terms of network architecture: 1) Feedforward networks, where the connections have no loops, and 2) recurrent networks, in which loops occur due to feedback connections [JMM96].

Figure 8 shows the architecture of a) feedforward neural network (FNN) and b) recurrent neural network (RNN) exemplarily. The neurons in multilayer networks are arranged in three different layers: an input layer, one or more hidden layers, and an output layer. The computation units of the hidden layers are correspondingly called hidden neurons, which serve as information processing units that intervene between the input and the network output in a useful manner. The network can extract higher-order statistics from its input by adding one or more hidden layers [Hay09]. In FNN, the information flows in only one direction from input to output. RNN is distinguished from FNN by the presence of at least one feedback loop. The backwards transmission of information in RNN allows the network to exhibit dynamic temporal behavior and process any sequence of inputs using internal memory [Suz11]. Many types of data, such as natural language and sound tracks, include extra information in the order in which they are presented, creating a sequence of data points. Typically, the term *time series* is used to describe

this kind of sequencing data [TPT22]. A simple example of using RNNs is to classify time series. RNNs have been applied for human activity recognition of daily living by using mobile and wearable sensors [NTA+18].

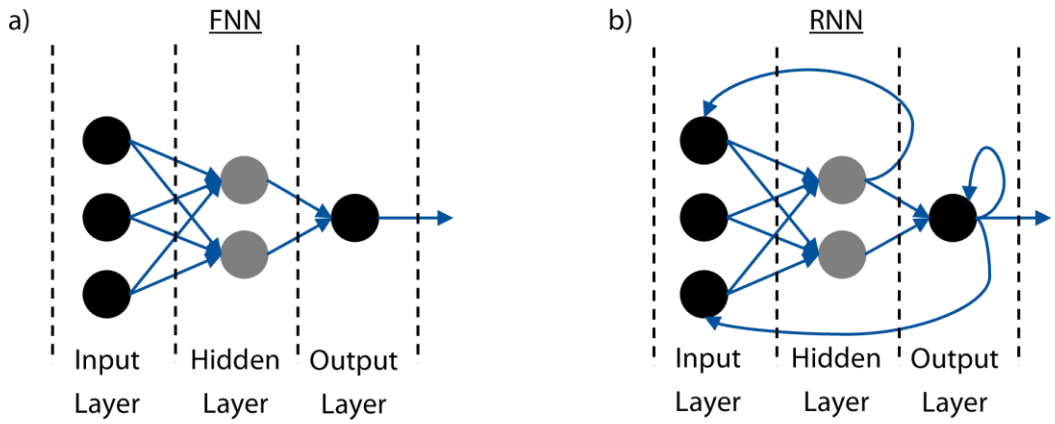

Figure 8: Exemplary architecture of a) feedforward neural network (FNN) and b) recurrent neural network (RNN)

A feedforward neural network with one or more hidden layers is also referred to as *multilayer perceptron*. One of the widely used methods for the training of a multilayer perceptron is the *backpropagation* algorithm, which uses the *gradient descent* method. The backpropagation process occurs in two phases: the forward phase and the backward phase. During the forward phase the input signal is propagated forwards through all the layers of the network till it reaches the output, while the synaptic weights remain unchanged. In the backward phase the generated output signal during the previous phase, is compared to a target value, resulting in an error signal. The obtained error signal is propagated through all the layers of the network, but this time the propagation is carried out backwards. The synaptic weights are successively adjusted throughout this second phase. The changes are relatively simple to handle for the output layer, but these weight adjustments are significantly more difficult for the hidden layers [Hay09].

2.1.2 Support Vector Machine (SVM)

SVM is one of the relatively new and promising supervised learning techniques for classification and regression. SVM demonstrates a strong mathematical foundation in statistical learning theory proposed by Vapnik [Vap99]. In general, SVM originated from a robust theory of implementation, whereas ANN progressed heuristically from application to theory. SVM, in

contrast to ANN, is a deterministic algorithm that uses the concept of *kernel trick* [Hol14]. The kernel trick is a method that maps the original inputs into a higher-dimensional feature space, where the optima of a convex optimization problem can be found analytically rather than heuristically, which is the case with other ML techniques [AK15]. By solving the convex optimization problem analytically, SVM training always finds a global minimum [SS11].

The performance of a ML model on a known set of training data is measured by the so-called *empirical error* or the empirical risk. The term *generalization* refers to the ability of the ML model to adapt properly to unseen data sets, not encountered during training. SVM has good generalization properties by using *Structural Risk Minimization* (SRM). This makes it particularly powerful over the traditional methods based on the empirical risk minimization, like the neural networks. SRM proposes a trade-off between the complexity of the machine and the empirical error. Thereby, SRM considers the expected gap between the training error and the test error.

Figure 9 illustrates how the error of the ML model varies with its complexity index. The error is considerable for non-complex models since a simple model cannot account for all the complexity of the data, leading to an *underfitting* state. The error decreases for the best model, indexed with h^*, as the complexity index rises before beginning to rise once again. For high model indices, the model begins tailoring its learning to the training data, leading to *overfitting*, which lowers the training error and raises the model complexity, but worsens the test error. By minimizing the structural risk, i.e. balancing the model complexity against its empirical risk, SVM avoids the problem of overfitting better than other ML approaches [AK15]. Hence, SVM is one of the most popular ML approaches for supervised learning because of its resilience, strong generalization ability, and unique global optimal solutions. However, the main restriction of SVM is the rapid growth in computing and storage requirements as the number of training data sets increases [Hay09].

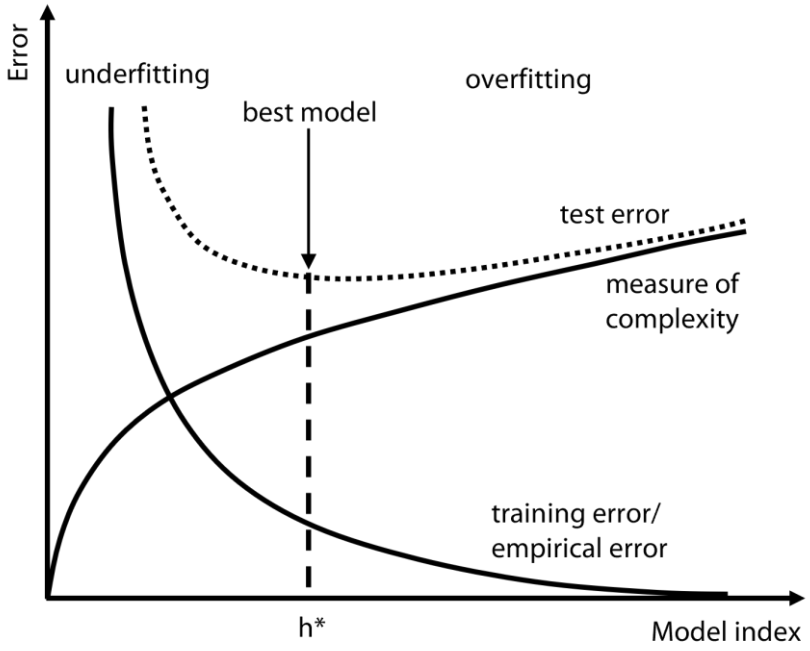

Figure 9: Relationship between error trends and model index [AK15]

SVM is a supervised learning method that can be applied to both classification and regression problems. In this context, classification is basically categorizing a set of data into classes and the term regression stands for data prediction. In the following, SVM classification will be explained first and this is then used to describe SVM regression.

2.1.2.1 SVM Classification

In SVM classification, a set of objects is divided into classes in such a way that the distances between the class boundaries are as large as possible, and thus minimizing errors. For this purpose, hyperplanes are used for the separation of the classes. In this context, a hyperplane is an affine subspace with dimension n-1. For example, if the space is two-dimensional, its hyperplanes are one-dimensional lines. Figure 10 shows sample objects with two different features, red and blue, in a two-dimensional space. Three hyperplanes, i.e. H1, H2 and H3, are placed in this space. The goal is to select a hyperplane that provides optimal separation with as few misclassified vectors as possible. Among the three illustrated hyperplanes, no classification was done by hyperplane H1 and therefore it is left out of consideration. On the other hand, a feature separation of the sample objects by both hyperplanes H2 and H3 took place. It can be shown that maximizing the margin of a hyperplane results in the optimal separating hyperplane

[BGV92]. Margin in this context stands for the minimum distance of a data point to the hyperplane. Thereby, a uniquely determined optimal hyperplane exists. Based on the aforementioned criterion, the hyperplane H3 in Figure 10 provides an optimal separation and this is called "*maximum margin hyperplane*". The points at the edge of the separation region, namely P1 and P2, are called "*support vectors*". In SVM problems, the determination of the optimal separating hyperplane is an optimization problem which is solved analytically.

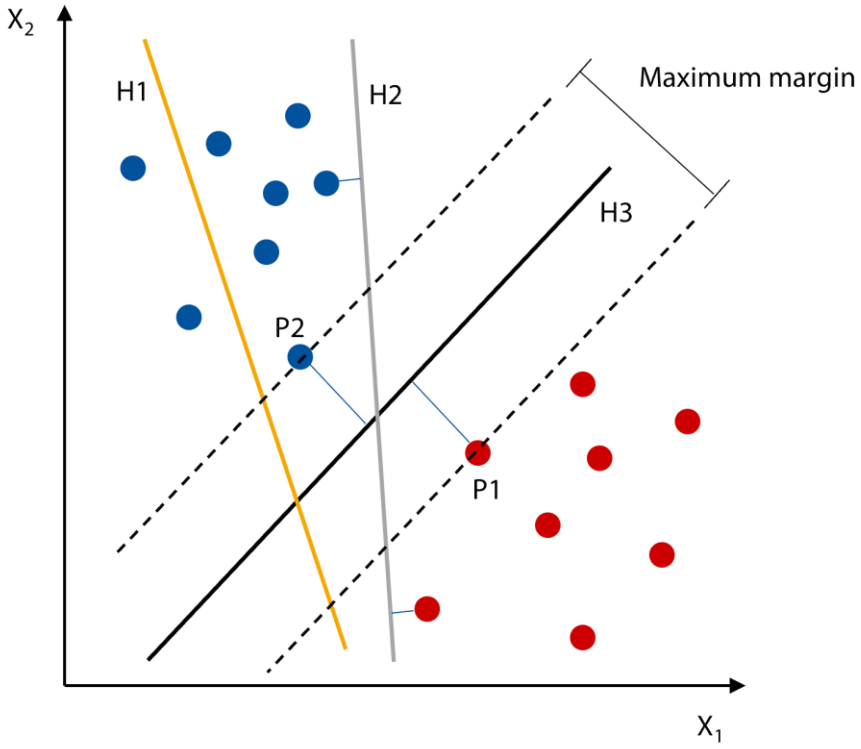

Figure 10: Separation planes in SVM classification

In contrast to the sample data shown in Figure 10, the training data is mostly not linearly separable. In this case, the SVM uses the so-called *kernel trick*. This involves transferring the input space to a higher dimensional space by using a kernel function, where the objects are linearly separable. Subsequently, the SVM algorithm is applied much simpler in the new feature space with higher dimension to determine the optimal hyperplane. Figure 11 illustrates the principle of a kernel function for SVM classification schematically. There are many different types of kernel functions which can be used to create the higher dimensional space, such as linear, polynomial, sigmoid, Radial Basis Function (RBF) or Gaussian. It is also possible to

construct new kernels by combining simpler kernels. A kernel function is good if we have better separation of the sample data in its corresponding space [Alp10].

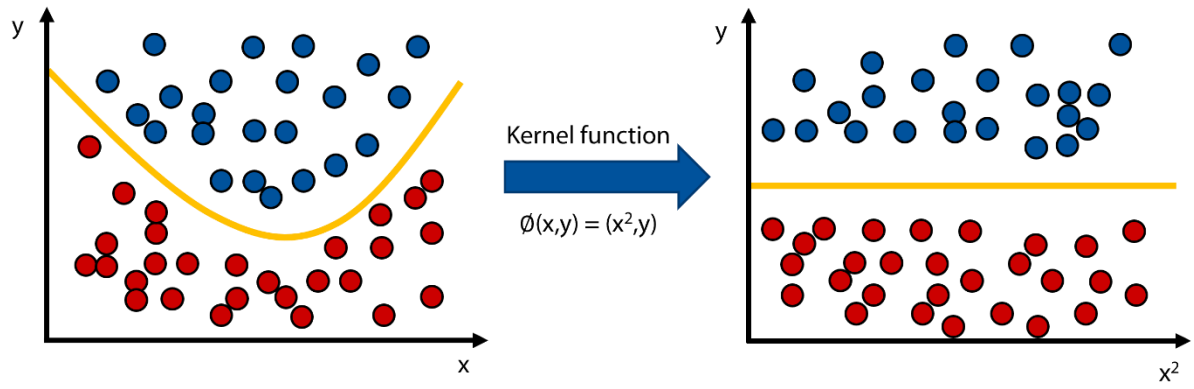

Figure 11: Schematic illustration of the principle of a kernel function for transformation into a linear problem in SVM classification

2.1.2.2 SVM Regression

The regression problem is an extension of the classification problem in which the model produces a continuous-valued output instead of a finite-valued output. In other words, a regression model estimates a multivariate function with continuous values. SVM can also be used as a regression method, keeping all the main features that characterize its classification algorithm, such as the maximum margin and the kernel function. In the following, the main mathematical formulations of the SVM regression technique are discussed.

The goal of linear SVM regression is to find an approximated hyperplane for the target model f in the form of

$$g(x) = \langle w, \phi(x) \rangle + b. \qquad \text{Eq. 3}$$

- $g(x)$ Prediction values
- w Normal vector of approximated hyperplane g
- ϕ Mapping function, which could initially be considered as identity function
- b Bias parameter

The predicted values from g should have a bounded deviation not more than ε from the target values $f(x)$, i.e.,

$$|g(x) - f(x)| \leq \varepsilon \qquad \text{Eq. 4}$$

The distance between the hyperplane g and the farthest point away is called margin and it is proportional to $\frac{1}{\|w\|}$. The boundary of a maximal margin is referred to as a support vector, as shown in Figure 12. Furthermore, g should be maximally flat, i.e. $\|w\|$ should be as small as possible and the margin as large as possible [SS18].

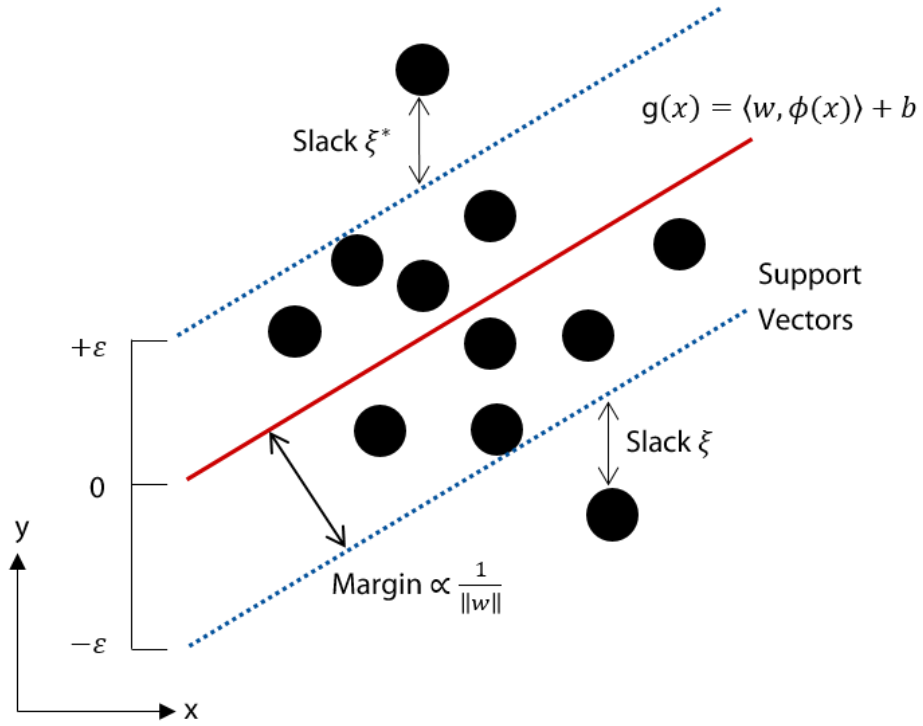

Figure 12: Illustration of the support vectors, margins and slack variables in SVM [BWH+21]

This kind of hyperplane is not always guaranteed to exist in practical cases. In order to cope with otherwise infeasible constraints, the slack variables ξ and $\xi^*$are introduced to construct a soft margin hyperplane. As a result, the constrained optimization problem could be formulated as the following equations [SS04]:

Minimize: $\frac{1}{2}\|w\|^2 + C\sum_i(\xi_i + \xi_i^*)$ Eq. 5

Subject to: $g(x) - f(x) \leq \varepsilon + \xi_i^*$ Eq. 5.1

$f(x) - g(x) \leq \varepsilon + \xi_i$ Eq. 5.2

$\xi_i, \xi_i^* \geq 0 \ \forall i = 1, \ldots, |\Omega|$ Eq. 5.3

- Ω Input variable space
- $C > 0$ Constant that determines the penalties for training errors

A closed form representation of the regression hyperplane g could be derived from the dual form of the optimization problem above, according to Eq. 6

$$g(x) = \sum_i (\alpha_i^* - \alpha_i)\langle x_i, x\rangle + b \quad \text{Eq. 6}$$

where α_i, α_i^* are Lagrange multipliers [SS04].

The already introduced linear form of SVM regression could be transformed into a nonlinear feature space via a nonlinear mapping $\phi : \Omega \rightarrow \widetilde{\Omega}$. The dot product in $\widetilde{\Omega}$ is expressed by the kernel function $k(x_i, x_j) = \langle \phi(x_i), \phi(x_j)\rangle$. With the implicit mapping of kernel function k, it is possible to directly compute the hyperplane g in the nonlinear feature space. With the so-called kernel trick, the final form of the approximated hyperplane can be expressed as Eq. 7

$$g(x) = \sum_i (\alpha_i^* - \alpha_i)\, k(x_i, x) + b \quad \text{Eq. 7}$$

where the corresponding constrained optimization problem is now formulated in the transformed feature space $\widetilde{\Omega}$ instead of in the original input variable space Ω, with the help of the implicit mapping ϕ and the kernel function k [SC04]. Figure 13 illustrates the principle of a kernel function for nonlinear regression problems schematically. As discussed above, the search for the best hyperplane in SVM regression, like in SVM classification, can be formulated as an optimization problem. One important advantage of SVM is that although the training

involves nonlinear optimization, the corresponding objective function is convex, and therefore, any local solution represents also a global optimum [BN06]. Furthermore, another primary advantage of SVM, as compared to ANN, is its good generalization ability, especially with limited number of training samples [SL12].

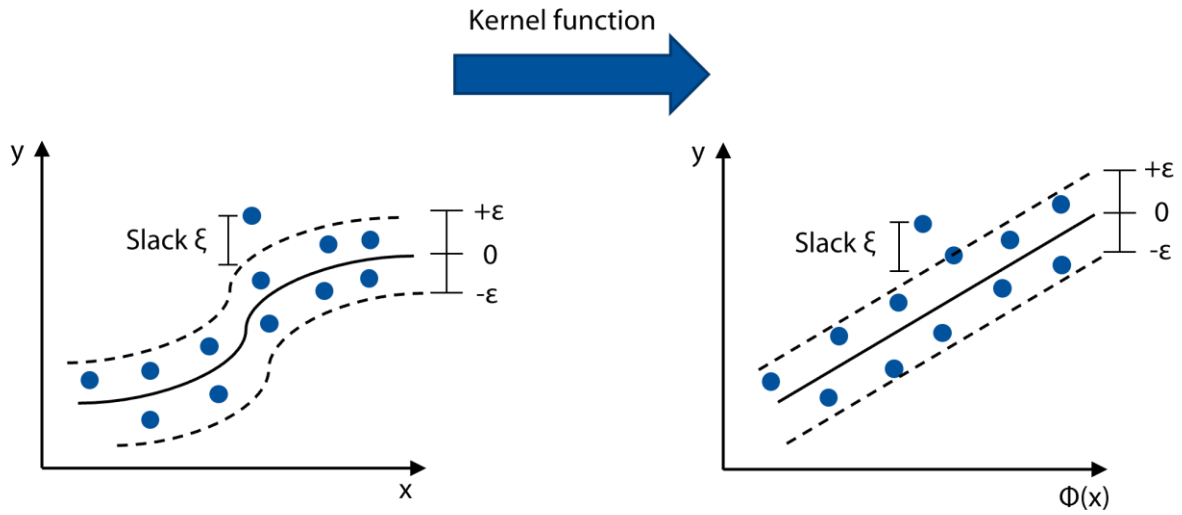

Figure 13: Schematic illustration of the principle of a kernel function in SVM regression for nonlinear problems

2.1.3 Fuzzy Logic (FL)

In addition to data-driven machine learning approaches, knowledge-based techniques are suitable for solving problems that cannot be adequately formulated mathematically. A Knowledge-based System (KBS) belongs to the artificial intelligence approaches that aim to retrieve knowledge from data/information in response to specific queries, along with learning and justification, or to transfer expertise from one domain of knowledge to another [AS09]. KBS in form of the so-called *expert system* can help to capture the knowledge of human experts to support decision-making.

Science frequently employs mathematical models that either result from mathematical reasoning or follow exemplary physical principles for explaining systems. In order to transition from a specific situation to an appropriate mathematical model, considerable idealization is frequently required. Furthermore, the models are usually deficient if the problems under consideration are not fully understood or are too complex. In this case, a suitable approach is

to tolerate a portion of vagueness and uncertainty in the modeling process at the beginning. Thereby, fuzzy and non-precise inferences are used rather of an expensive accurate inference. Thus, complexity reduction is achieved compared to other systems. With the introduction of *Fuzzy Logic* (FL) by Lotfi A. Zadeh in the 1960s [Zad65], a new era began for KBS and expert systems in particular. FL is a type of knowledge-based strategy that allows handling with complex and ill-defined problems that are characterized by cognitive uncertainty, imprecision or fuzziness/vagueness. Thereby, diverse phenomena in the inference process may emerge, e.g.:

- Uncertainty: "Coating porosity is almost certainly lower at high particle melting ratios."
- Imprecision: "Electrical current is between 500 and 540 A."
- Fuzziness: "Influence of electrode wear on coating properties is very high."

The basic idea of FL is to incorporate expert knowledge and experience when the creation of an exact mathematical model is very time-consuming or impossible due to the complexity of the system. FL works with the so-called *fuzzy sets*. Unlike ordinary sets, where elements belong uniquely to a set or not, fuzzy sets allow arbitrary membership degree between 0 and 1. A function describing such fuzzy sets is called a *membership function* (MF), see Figure 14.

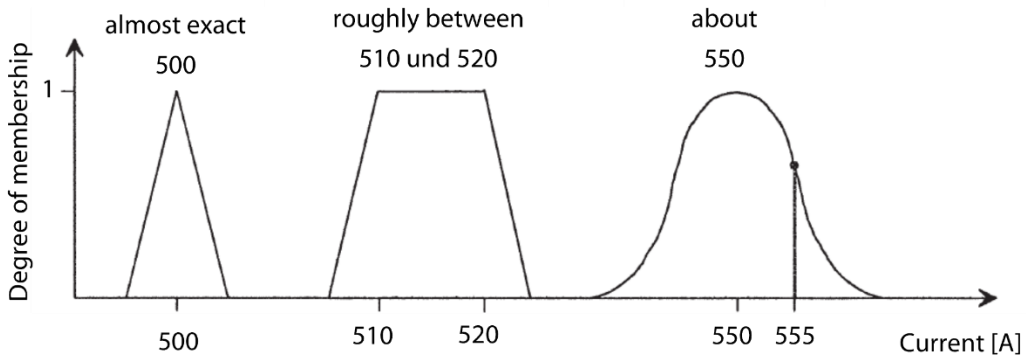

Figure 14: Some typical forms of membership functions

FL describes the complex system by means of linguistically formulated rules or *rule base*. The rules establish relationships between input and output of the system. Linguistic rules based on human experience allow for the qualitative characterization of a system without relying on exact quantitative analysis of nonlinear correlations among input and output parameters. A *fuzzy inference system* (FIS) basically comprises a fuzzifier, a block of database and rule base that is jointly referred to as knowledge base, a decision-making unit and a defuzzifier, see Figure 15.

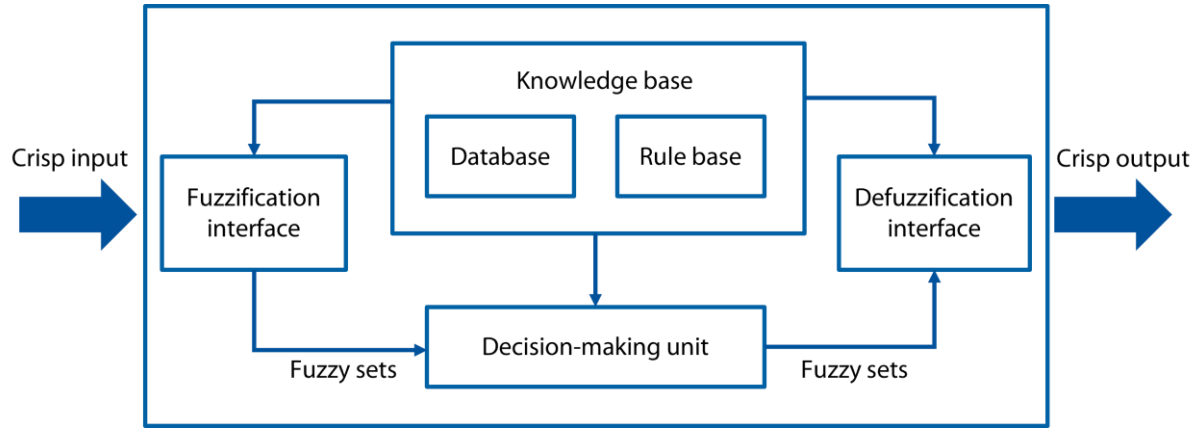

Figure 15: General architecture of a fuzzy inference system [BHD22]

The fuzzification interface converts the crisp inputs into degrees of match with linguistic values. The rule base contains a number of fuzzy if-then rules and the database defines the membership functions of the fuzzy sets used in the fuzzy rules. As described earlier, MF quantifies the degree to which an input element belongs to a particular fuzzy set. The values mapped by a MF are known as grade or degree of membership, and they range from 0 to 1. The inference operations on the rules are performed by the decision-making unit and finally the defuzzification interface transforms the fuzzy results of the inference into a crisp output. Fuzzy if-then rules are expressions in form of IF x is A THEN z is B, where A and B are labels for fuzzy sets characterized by suitable membership functions. The IF part is also called premise and the THEN part is referred to as consequence. This brief form of problem description facilitates the integration of human knowledge to deal with an uncertain and imprecise environment.

2.1.4 Adaptive Neuro-Fuzzy Inference System (ANFIS)

Due to insufficient knowledge, faults, or the complexity of the ill-defined system, FL is not optimal for achieving desired results in certain situations. For instance, developing a knowledge base for the stochastic process of plasma spraying depends on instinct and experience and is therefore an iterative and challenging task [JLC07]. Moreover, the human-determined membership functions differ from person to person and from time to time. On the other hand, ANN provides interesting benefits such as learning capability, adaptability, optimization and generalization. In the 1990s, Jyh-Shing Roger Jang [Jan93] integrated the best features of ANN and FL, and proposed his novel architecture under the terminology Adaptive Neuro-Fuzzy

Inference System (ANFIS). ANFIS uses a feed-forward neural network to automatically construct and tune rule bases and MF parameters from given sample data sets. Therefore, it leverages not only the advantages of neural networks but also the idea of conditional statements for uncertain systems. Figure 16 shows the general architecture of ANFIS with five layers, each of which is made up of several nodes. The inputs of each layer are obtained by the nodes from the previous layer, similar to a neural network.

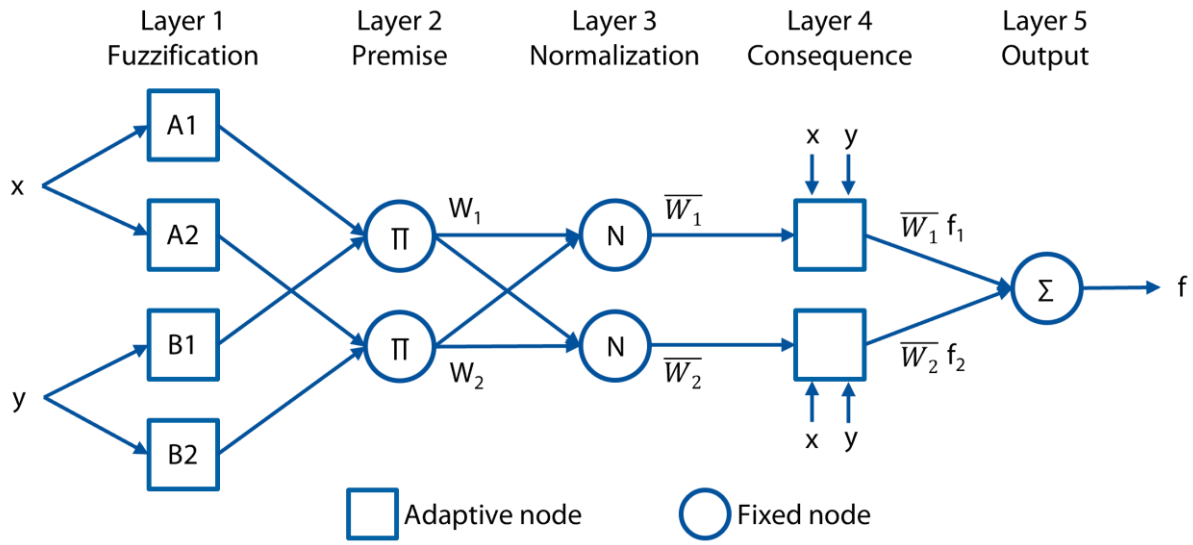

Figure 16: General architecture of ANFIS with two inputs, one output and two fuzzy if-then rules [BHD22]

For the sake of simplicity, the considered system is assumed to have two inputs x and y, one output z and two fuzzy if-then rules as follows [Jan93]:

Rule 1: If x is A_1 and y is B_1, then $f_1 = h_1 x + q_1 y + r_1$

Rule 2: If x is A_2 and y is B_2, then $f_2 = h_2 x + q_2 y + r_2$

where A_i and B_i in the premise part are linguistic labels that are represented by fuzzy sets and characterized by an appropriate MF, while h_i, q_i and r_i are the consequent parameters of the i-th rule. The node functions in each layer are described below.

Layer 1: Every node i in the first layer is an adaptive node and has the output O_i^1 with a node function according to Eq. 8

$$O_i^1 = \mu_{A_i}(x) \qquad \text{Eq. 8}$$

where μ_{A_i} denotes the MF of A_i and it specifies the degree to which the given x satisfies the quantifier A_i.

In this work, Gaussian membership functions have been used according to Eq. 9, where $\{a_i, c_i\}$ is the parameter set that can be adapted to form various forms of Gaussian MFs. Parameters in this layer are referred to as premise parameters [Jan93].

$$\mu_{A_i}(x) = exp\left[-\left(\frac{x - c_i}{a_i}\right)^2\right] \qquad \text{Eq. 9}$$

Layer 2: Every node in this layer is a fixed (non-adaptive) node labeled with $\prod$ that multiplies the incoming signals and sends the product out. A sample node function in this layer is given in Eq. 10, where w_i represents the so-called *firing strength* or degree of match with the premise part of the i-th rule.

$$w_i = \mu_{A_i}(x) \times \mu_{B_i}(y), \qquad i = 1, 2 \qquad \text{Eq. 10}$$

Layer 3: Every node in this layer is a fixed node labeled with N. The node function in this layer calculates the ratio of the i-th rule's firing strength to the sum of all rules' firing strengths according to Eq. 11. The term $\overline{w}_i$ is referred to as *normalized firing strength*.

$$\overline{w}_i = \frac{w_i}{w_1 + w_2}, \qquad i = 1, 2 \qquad \text{Eq. 11}$$

Layer 4: Every node in this layer is an adaptive node. The node output of the fourth layer is the product of the respective previously found normalized firing strength with the consequent part of the respective rule, as given in Eq. 12.

$$O_i^4 = \overline{w}_i f_i = \overline{w}_i (h_i x + q_i y + r_i) \quad \text{Eq. 12}$$

In Eq. 12, $\overline{w}_i$ is the output of the third layer and $\{h_i, q_i, r_i\}$ is the set of adaptive parameters of the fourth layer, namely consequent parameters.

Layer 5: The single node in this layer is a fixed node labeled with $\sum$ that computes the overall output O_i^5 as the summation of all incoming signals according to Eq. 13. The final output of the system is the weighted average over all rule outputs.

$$O_i^5 = \sum_i \overline{w}_i f_i = \frac{\sum_i w_i f_i}{\sum_i w_i} \quad \text{Eq. 13}$$

In the literature, several kinds of fuzzy reasoning have been introduced [Lee90]. *Mamdani* [MA75] and *Takagi-Sugeno* [TS85] are the two most well-known types of FIS. The most fundamental difference between these two FIS types is the way the crisp output is generated from the fuzzy inputs. Mamdani employs defuzzification of a fuzzy output, whereas Sugeno computes the crisp output using weighted average. As a result, the computationally expensive defuzzification process is bypassed in Sugeno [HG08]. The type of FIS in Figure 16 is Sugeno. This can be noticed from the two earlier stated rules, as the fuzzy sets are involved only in the premise parts, while the consequent parts are described by a non-fuzzy equation of the input variable. The Mamdani-type has a more interpretable rule base and is well-suited to human input; a good example of its application field would be medical diagnostics. The Sugeno-type has more flexibility in system design, is computationally efficient and works well with optimization and adaptive techniques [HG08]. Hence, the Sugeno-type FIS has been also implemented in this work.

2.2 Artificial Intelligence in Plasma Spraying

The coating properties in atmospheric plasma spraying (APS) are a function of three interdependent subsystems in general: 1) the generation of the plasma jet, 2) the injection and interaction of the feedstock material with the plasma jet that meanwhile mixes with the surrounding gas and 3) the impact and solidification of the particles on the substrate [VMT+15]. During each subsystem, several physicochemical mechanisms occur, which lead to the formation of a coating. These mechanisms include momentum and heat transfers from the

plasma jet to the particles prior to impact and during solidification, as well as mass transfers caused by partial vaporization of the particles in the plasma plume. Therefore, each subsystem has a large number of variables that influence the plasma spraying process.

The number of influencing factors in APS is estimated to be more than 200 variables [SBD+06]. It should be emphasized that many of these factors are intimately connected by complicated nonlinear relationships. These interactions further increase the complexity of the overall APS system. Taking the above aspects into account, the question of robust methods for quantifying the complex interactions between the dozens of influencing factors in APS arises. It turns out that computer-aided algorithms can best fulfill this challenging undertaking. Artificial intelligence (AI) methods are suitable tools to investigate complex processes with parameter dependencies.

Previous research studies have used AI approaches to mainly forecast process parameters in order to attain the desired in-flight particle properties or coating characteristics. According to the literature, ANN is the most commonly used method of AI in plasma spraying. There are only few works that have employed SVM in TS [XH17, GAU+20]. There have already been studies at the Surface Engineering Institute (IOT) at the RWTH Aachen University to analyze process data, coating properties and plasma jet characteristics using ANN and Design of Experiment (DoE) [See05, Ern07]. In other studies, Guessasma et al. [GMG+03] developed an ANN model to predict the in-flight particle properties of plasma sprayed Al_2O_3 13 wt.% TiO_2 feedstock material. Kanta et al. [KMV+08] implemented ANN and FL to predict the in-flight particle properties as a function of process parameters for deposition of alumina-titania by APS. They concluded that the ANN model appeared well suited for process prediction, whereas the FL model seemed more adapted for process control. In another work of Kanta et al. [KMB+11], an expert system was created by ANN and FL to control and adjust the process parameters so that constant values for the in-flight particle properties can be maintained. They aimed to account for the instabilities and intrinsic fluctuations inherent in the APS process based on the pre-defined rules of the FL model. Liu et al. [LPK+13] developed an expert system by implementation of ANN models and FL controllers to predict and control the in-flight particle properties and operating parameters. Similar to the work of Kanta et al., they predefined the fuzzy rules manually according to experimental data.

As the use of ANN and FL revealed drawbacks such as reliance on a significant quantity of experimental data and taking too much time in construction of the rules, the ANFIS technique was employed in subsequent works due to its high prediction accuracy and low execution time [PGN+15]. Datta et al. [DPB13] aimed to predict coating properties from process parameters in APS by developing an ANFIS, which was tuned using a genetic algorithm (GA) and particle swarm optimization (PSO) algorithm, separately. They found that the PSO-based approach performed better than the GA-based optimization in predicting the responses. Furthermore, in [Wu15] an empirical model was developed by combination of ANN and ANFIS to investigate the effect of process parameters on the coating properties in APS.

Although studies have been conducted to develop AI models for predicting particle or coating properties, the research in investigating the interactions between process parameters, in-flight particle properties and *deposition efficiency* (DE) remains limited. One of the obstacles in this regard is the lengthy and time-consuming data collection to measure DE and the corresponding particle properties for different process parameters. One possible solution to tackle this problem is to produce data by employing simulation and modeling approaches like the Computational Fluid Dynamics (CFD). The advantage of using simulation results is the opportunity to cover a broad range of process parameters, while providing that much experimental data is barely possible. The majority of prior research works have used experimental data sets to create predictive models for the TS process variants. There are only few studies in the literature that used simulation data sets for training ML models in TS [ZWK+20]. While simulation and modeling approaches can help to produce sufficient data of in-flight particle properties, the problem of data collection for DE still remains. In order to address this issue in terms of experimental data, first an analysis of the methods and equipment available to capture the in-flight particle properties is required. Following that, the state of the art regarding measurement of DE will be discussed.

2.3 In-flight Particle Diagnostics

Particle diagnostic methods support the coating development process by allowing the observation of particle properties in the free jet. These include measurements of particle size, velocity and temperature. The evolution of sensors in thermal spraying for particle in-flight diagnostic measurements has progressed considerably in recent years. Particle diagnostic systems have broadened our understanding of the spraying process and improved the reproducibility of the coatings.

Different diagnostic devices show deficits in the number of detected particles and this depends, among others, on the sensor measurement volume and the stand-off distance [Lan06, FV10]. The diagnostic sensors employ mainly two different techniques: local measurement and ensemble measurement. In case of the local measurement, the observation of a single particle is possible. The ensemble measurement technique does not distinguish between individual particles and give only average values [FV10]. In conventional spray processes, numerous particle diagnostic methods and systems have been developed, such as Phase Doppler Anemometry (PDA), Accuraspray, DPV-2000, SprayWatch and HiWatch. The PDA technique is unable to measure the particles with an angular and blocky morphology. The Accuraspray is categorized as ensemble measurement and delivers a single mean value from the captured particle data in the whole measurement volume. The DPV-2000 is a well-established diagnostic system, which operates based on the principle of two-wavelength pyrometry. This diagnostic system utilizes the local measurement technique and has a relatively small measurement volume (< 1 mm^3). The DPV-2000 can detect only relatively hot particles and measure their size, velocity and temperature. In case of using a laser to illuminate the cold particles, it is not possible to measure the particle temperature. This is prominently due to the laser-induced alterations in particle radiation, disrupting conventional temperature measurement techniques. SprayWatch is a particle diagnostic system especially for HVOF and HVAF processes, however, it works well also on the other processes. It measures particle velocities and temperatures, but not particle sizes. The HiWatch system consists of a camera and a pulsed laser diode to illuminate the particles. It can measure particle sizes and velocities, but not particle temperatures. The functional principle of this device is discussed later in detail in Chapter 4. The HiWatch system has a larger measurement volume (6.5 mm × 9 mm × 2 mm) compared to DPV, and is capable of observing a single particle. Furthermore, it has the advantage to capture both cold and hot particles.

The temperature and velocity of the particles vary significantly in the plasma jet, depending whether the particles are in the hot core of the jet or in its relatively cold outer part. Due to this temperature and velocity difference in the plasma jet, the deposition behavior of the particles on the substrate depends on their individual trajectory. Hence, in order to find a practical compromise between deposition efficiency and particle properties, the detection of the entire plasma jet is necessary.

In principle, the particle diagnostic systems focus on one point or one focal plane and therefore, they can only partially capture the free jet. This point or plane is usually chosen in view of the maximum concentration of the particles and then a rotationally symmetrical free jet is assumed. This assumption is generally not correct due to incessant plasma fluctuations. In addition, given the dynamic range and signal-to-noise ratio of the diagnostic sensors, only particles within a certain measurable range are detected [WRT+10]. Thus, particle diagnostic systems show deficits in measured data and do not allow a holistic recording of the free jet. The detection of the entire free jet as well as the verification of the diagnostic measurements represent a central research need in the field of thermal spraying.

2.4 Deposition Efficiency

During a thermal spray process, only part of the injected feedstock material adheres to the component surface and creates a coating. The deposition rate, [g/s] or [kg/h], of a coating process is defined by this part that adheres to the substrate. The part that does not adhere is lost as the so-called *overspray*. The ratio between the mass of the coating and the mass of the feedstock material supplied to the process defines the deposition efficiency (DE) [%] and determines the overall efficiency of the process. In industrial production, high DE has been always one of the central goals in the process development of thermal spraying to achieve cost-effective coatings.

Previous studies aimed mainly to seek a compromise between input process parameters and deposition efficiency of the plasma-sprayed coatings [WXZ+17, BM12]. For instance, there is a general tendency that the DE initially increases and then decreases with the increase of the electrical current, voltage and primary gas flow [VSY+09]. Furthermore, few studies have tried to build up the spray footprint profiles with simulation models [WM13]. However, simulative

determination of DE in thermal spraying, due to lack of physical equation sets for adhering the particles on the substrate, is not yet state of the art.

The DE in thermal spraying is intimately related to the in-flight particle properties. The particle properties can be influenced through several adjustable as well as nonadjustable factors. The adjustable parameters include the flow rates of plasma and carrier gas, input electrical power of the torch and the injector geometry design [BÖK+20, GMC05]. The nonadjustable influencing factors are, among others, the wear of the electrodes and entrainment of the surrounding cold gas [MVS11]. Due to the multitude of influencing factors and their nonlinear interactions, the determination of the correlations between particle properties and DE is currently based on the experience of the operator and is mostly done by ex situ experiments [SSV+09]. Accordingly, the prediction of particle properties leading to a coating process with the desired DE is largely based on time-consuming trial and error. This approach complicates the coating development process and significantly extends the coating development time. Furthermore, available studies are limited to the average particle properties, which are commonly captured at the centerline of the free jet. There has not been an in situ mechanism yet to correlate the in-flight particle properties in the entire free jet with their DE on the substrate locally, see Figure 17. Therefore, an in situ determination of DE is necessary in order to investigate the influences of process parameters and in-flight particle properties on the adhesion of the particles to the substrate.

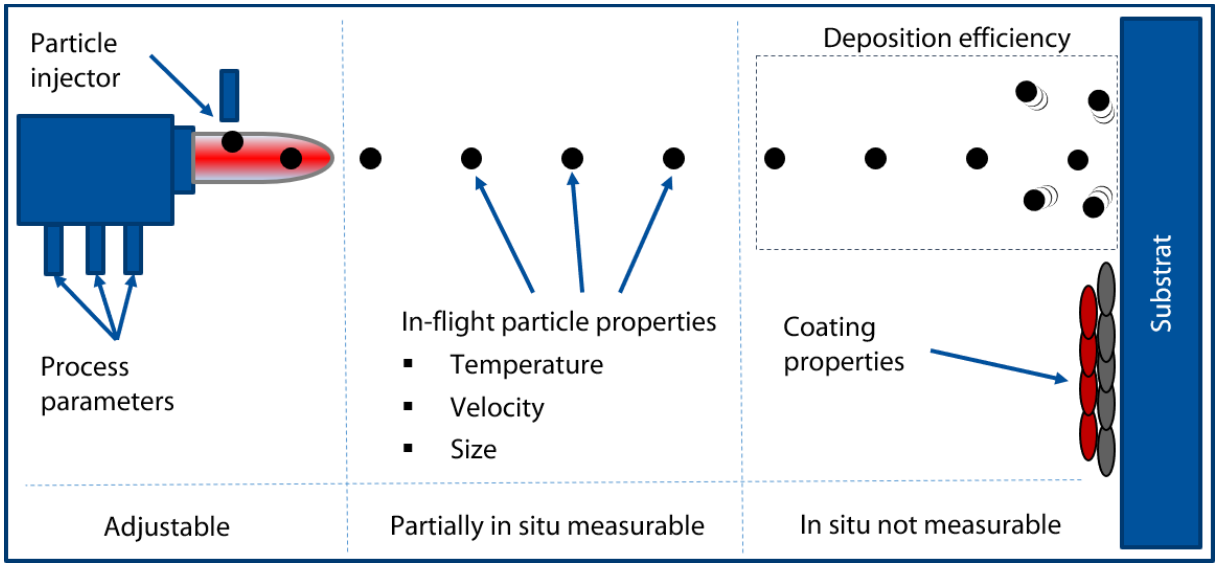

Figure 17: Detectability of different variables in TS according to the state of the art

2.5 Conclusion

The coating properties in atmospheric plasma spraying (APS) is a function of numerous influencing factors, which have intricate nonlinear relationships. The complexity of the plasma spraying system arises the question of robust methods for quantifying the complex interactions between the dozens of influencing factors. The methods of artificial intelligence (AI) can best fulfill this challenging undertaking.

Deposition efficiency (DE) serves as a key performance indicator in plasma spraying, which is also determined by dozens of intrinsic and extrinsic influencing factors. Finding a compromise between process parameters, in-flight particle properties and DE can help to improve the productivity, efficiency and consequential sustainability of the APS process. The main step toward this aim, is to gather the already available data or to provide new data in an efficient manner. Since multiple experiments to measure particle properties and DE in plasma spraying are a lengthy way to generate data, a novel approach to address this issue must be found. The amount of training data and their quality are the most important requirements for developing precise AI models to improve the efficiency of the process.

The literature review on employing AI techniques to find a compromise between process parameters, in-flight particle properties and DE can be summarized as follows:

- The majority of prior research has focused on developing AI models to predict coating or particle properties.
- According to the literature, ANN is the most commonly used method of AI in plasma spraying. There are small number of works in TS that have employed deterministic ML models with structural risk minimization, like SVM.
- Only few studies have been done specifically to create expert systems for prediction and increase of DE.
- It is lengthy and time-consuming to collect sufficient data on DE and the corresponding particle properties for different process parameters.
- The benefit of using simulation data sets for particle properties to train ML models has rarely been considered.
- Since the deposition behavior of the particles on the substrate depends on their individual trajectory, the detection of the entire plasma jet is necessary for DE correlations.
- A new approach is needed for in situ determination of DE to tackle the problem of insufficient experimental data.

3 Aim and Solution Approach

To fill the literature gaps mentioned in the previous chapter, this dissertation is dedicated to the development of a Digital Shadow in plasma spraying with the ultimate goal of improving the process efficiency. For this purpose, modern AI methods, such as SVM and ANFIS, were used to develop and combine domain-specific models using simulation or experimental data from the entire process chain of APS. These data include process parameters, in-flight particle properties and deposition efficiency on the substrate. Furthermore, to tackle the problem of insufficient data for AI models two approaches were pursued: 1) A methodology for in situ determination of spatially resolved deposition efficiencies on the substrate and 2) generating simulation data by recycling the simulation models of the plasma jet developed at the Surface Engineering Institute (IOT) at the RWTH Aachen University. The term "data recycling" refers to the reuse of data from already developed models [Nia20]. It should be noted that the reused simulations have already been validated by comparing the numerical results of the particle properties with experimental measurements [BÖS+17]. The combination of these two strategies provided the aggregated and purpose-driven data sets required for Digital Shadows in plasma spraying.

Figure 18 depicts the proposed solution approach for the development of a Digital Shadow in plasma spraying with the ultimate goal of improving the process efficiency. The main steps leading up to the proposed Digital Shadow in this work are briefly outlined below.

- Development of a methodology to estimate the particle mass flow rate in the entire plasma jet using in-flight particle diagnostics
- In situ determination of spatially resolved deposition efficiencies on the substrate, namely local deposition efficiency (LDE), based on the particle mass flow rate in the plasma jet
- Generating simulation data sets of in-flight particle properties with their corresponding process parameters by recycling the already developed simulation models at the IOT
- Prediction of in-flight particle properties using SVM with simulation data sets
- Prediction of LDE using ANFIS with experimental data sets
- Development of an expert system by combination of SVM and ANFIS models to predict LDE in plasma spraying
- Demonstrate the proof of concept to predict the global DE out of the developed expert system trained with the LDE data sets

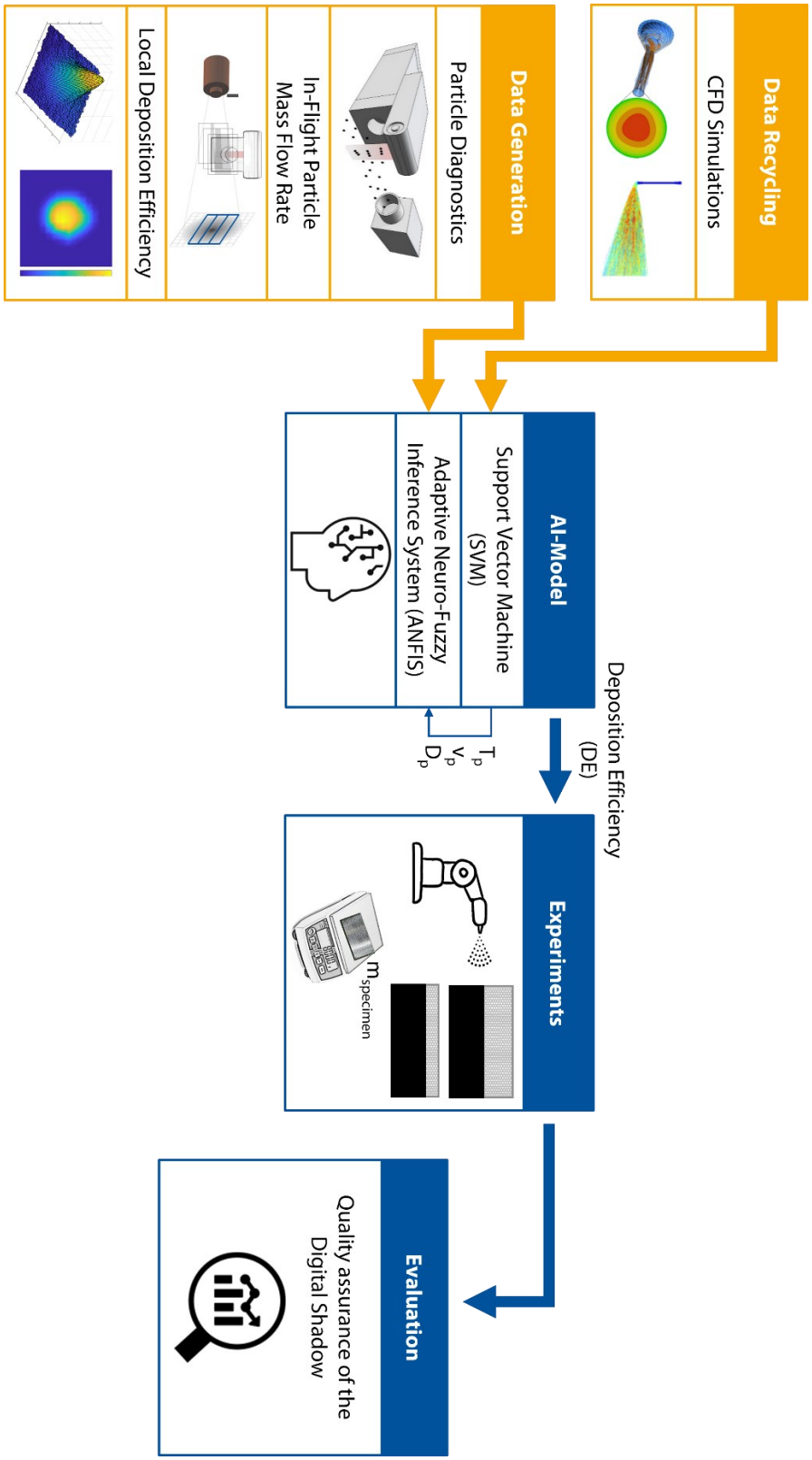

Figure 18: Solution approach for the development of a Digital Shadow in plasma spraying with the ultimate goal of improving the process efficiency

4 Particle Mass Flow Rate (PMFR) in Plasma Jet

In this chapter, a novel method is presented to estimate the particle mass flow rate (PMFR) throughout the plasma jet, which has been already published in [BWK+20]. This approach serves as a prerequisite for the calculation of local deposition efficiency in the next chapter. An in situ measurement of the PMFR in the plasma jet is a technically challenging issue, which can be significant to attain efficient utilization of the feedstock powder and to reduce overspray. The main challenge is that capturing the average particle properties at the plasma jet center would not be sufficient to measure the PMFR. Thereby, it is necessary to capture the entire plasma jet to attain a good estimation of the PMFR based on the absolute values of the particle properties existing in the jet. To this end, the entire free jet transverse section is divided into several non-overlapping focal planes. Optical particle diagnostics have been carried out to measure the size and velocity of the in-flight particles at these focal planes. A mathematical model is proposed to derive the PMFR in the free jet based on the measured in-flight particle sizes and velocities. The PMFR of the powder feeder is then utilized as a reference to validate the diagnostic measurements. Subsequently, the determined PMFR distributions at the entire free jet are compared to the generated *experimental footprints*. The cumulative deposition profile of the impacted particles on a prepared substrate is known as spray footprint or spray pattern. Accordingly, the PMFR distribution at the entire free jet is referred to simply as *digital footprint* in this work.

4.1 Spray Parameters and Feedstock Materials

The single-cathode plasma generator F4MB-XL (Oerlikon Metco, Wohlen, Switzerland) and the three-cathode plasma generator TriplexPro™-210 (Oerlikon Metco) were used to do the experiments. The plasma generators were mounted on a six-axis robot (KUKA AG, Augsburg, Germany). The APS system was equipped with an external powder feeder with a transverse particle injection system relative to the horizontal gun axis. A conventional injector with the diameter of Ø = 2 mm was used. Two commercial feedstock materials were used to conduct the diagnostic measurements: Aluminum oxide (AMDRY 6062, Oerlikon Metco) and aluminum bronze (Metco 51NS, Oerlikon Metco). The volume-based particle size distributions as well as other properties of the feedstock powders used in this study are given in Table 2. The size distribution of the particles was determined by the particle analysis system Morphologi G2 (Malvern Panalytical Ltd, Malvern, England).

Table 2: Properties of the feedstock powders

Property	Al_2O_3	Cu10Al
D [v, 0.05], µm	17.6	28.58
D [v, 0.5], µm	31.85	75.06
D [v, 0.95], µm	50.3	125.7
Density, g/cm³	3.98	7.57
Manufacture	fused and crushed	gas atomized
Morphology	angular / blocky	spheroidal

The morphology of the powder particles was examined using a scanning electron microscope (SEM). The obtained SEM result is shown in Figure 19. The SEM image indicates an angular and blocky morphology of the particles.

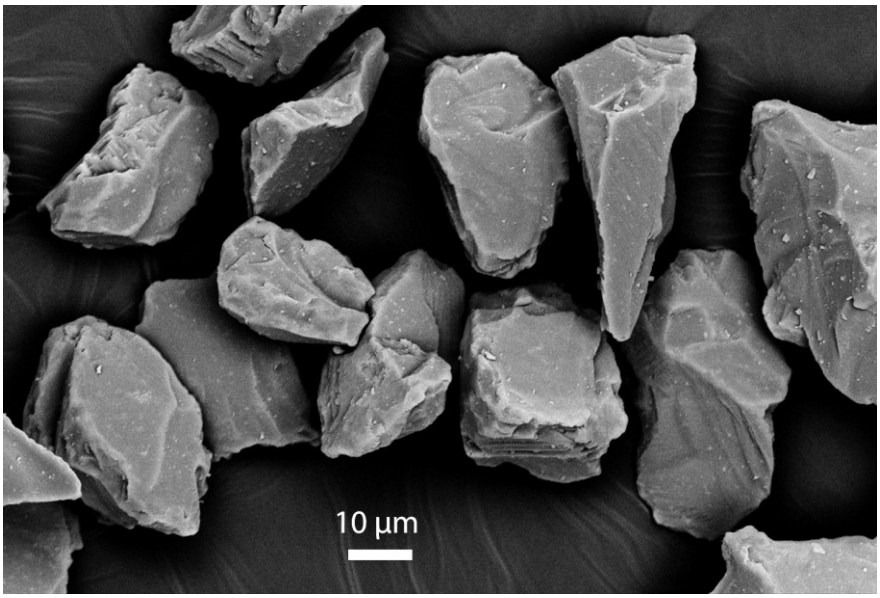

Figure 19: Morphology analysis of the alumina feedstock particles using SEM

Figure 20 shows the result of the morphology analysis using SEM for the Cu10Al spray particles. In comparison with fused and crushed powders, which have an irregular particle shape, gas atomized powders have a spherical shape. The resulted SEM image for the gas atomized Cu10Al confirms this matter.

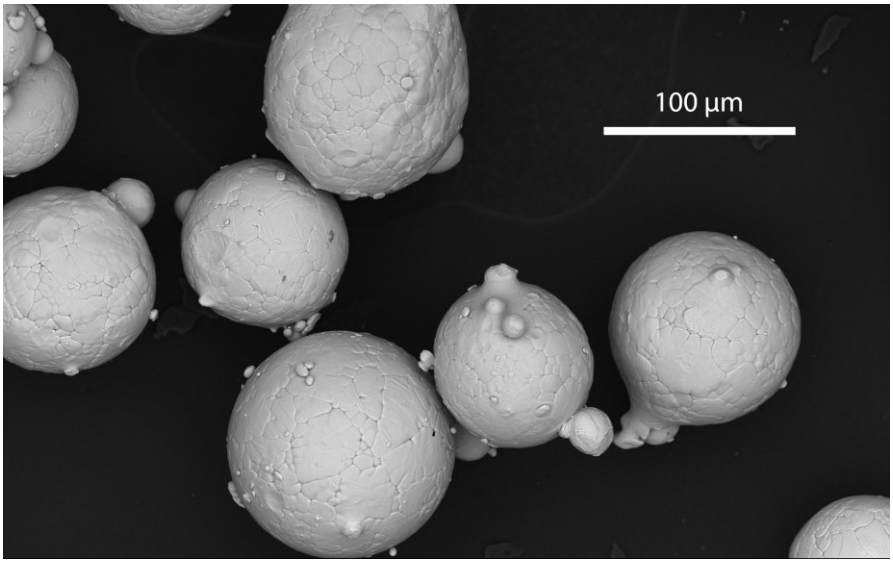

Figure 20: Morphology analysis of the Cu10Al particles using SEM

The spray powders used for the diagnostic experiments were selected based on different particle sizes and morphologies. The spray parameters with regard to the plasma torches and feedstock powders are listed in Table 3.

Table 3: Spray parameters used for particle diagnostic experiments

Parameter	Single-cathode gun	Single-cathode gun	Three-cathode gun
Feedstock material	Al_2O_3	Cu10Al	Al_2O_3
Current [A]	600	500	500
Input power [kW]	35.6	25.5	48.4
Argon [SLPM]	42	50	60
Hydrogen [SLPM]	9	2	-
Carrier gas (Ar) [SLPM]	5.5	3.5	5.5
Nozzle diameter [mm]	6	6	9

4.2 Experimental Footprints

The cumulative deposition profile of the impacted particles on a prepared substrate is known as spray footprint or spray pattern. Experimental footprints were produced to determine the section of the free jet in which most particles are located. The point with maximum particle

intensity was then considered as the reference point for the particle diagnostic experiments. Furthermore, the determined PMFR distributions at the entire free jet are compared to the profile of the experimental footprints. The PMFR distribution at the entire free jet will be referred to simply as "*digital footprint*" for the remainder of this thesis.

To generate footprints, the plasma gun was held at a spray distance of d = 100 mm in front of the substrate for 5 seconds. Figure 21 shows a) the principle of generating a footprint schematically and b) an experimental footprint with the three-cathode plasma gun and alumina spray powder.

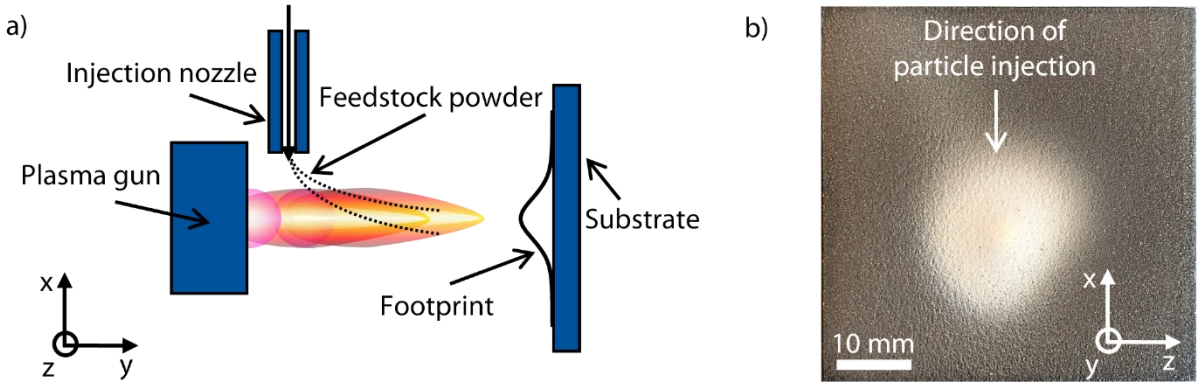

Figure 21: a) Schematic illustration of generating a footprint and b) an experimental footprint with the three-cathode plasma gun and alumina spray powder [BWH+20]

Flat samples made of S235JR structural steel with the dimension of 50 × 50 × 5 mm³ were used as substrates. Before producing the footprints, a grit blasting system was utilized to roughen the substrates with a pressure of p = 0.4 MPa and corundum with a grit size of F16. To ascertain the height profiles of the experimental footprints, a confocal laser-scanning microscope (VK-X 210 Keyence, Osaka, Japan) was used with a 10X optical magnification. Figure 22 illustrates a) the 3D height profile of the experimental footprint and b) the substrate under the laser-scanning microscope.

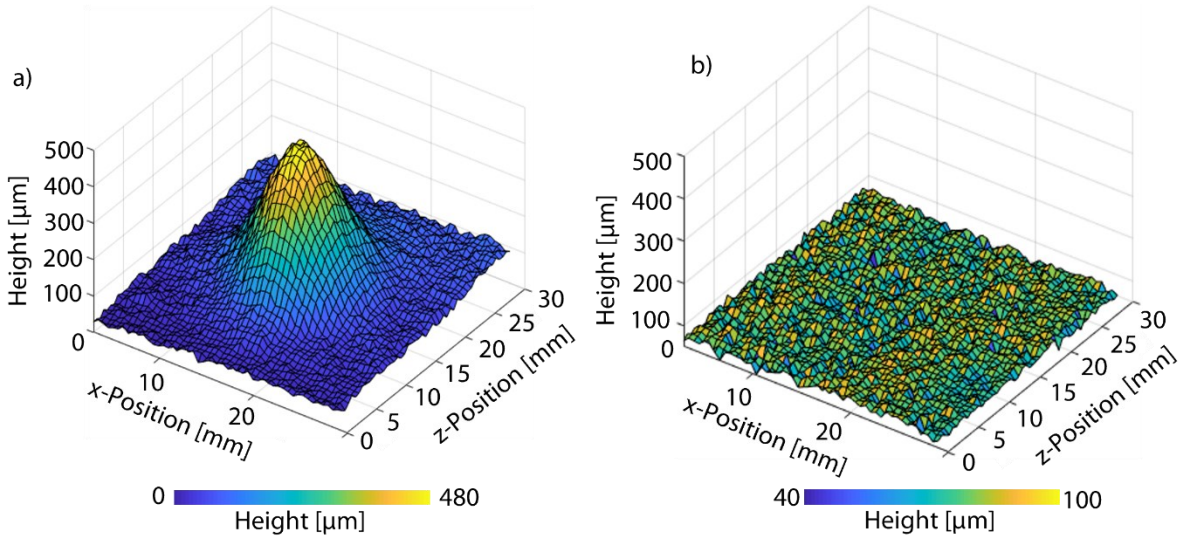

Figure 22: a) 3D height profile of the footprint and b) substrate under the laser-scanning microscope [BWH+20]

4.3 Particle Diagnostics

The particle diagnostic system HiWatch CS (Oseir Ltd, Tampere, Finland) was used to conduct the particle diagnostic measurements. The output data of this diagnostic tool are, among others, the size, velocity and position of the particles. The device package consists of a pre-aligned assembly of a camera and a pulsed diode laser head with a power of 50 W. The HiWatch system measures the particle properties based on the stroboscobic image analysis, where the particles on certain transverse section of the free jet are recorded using triple-exposure imaging. The functional principle of the HiWatch system is schematically illustrated in Figure 23.

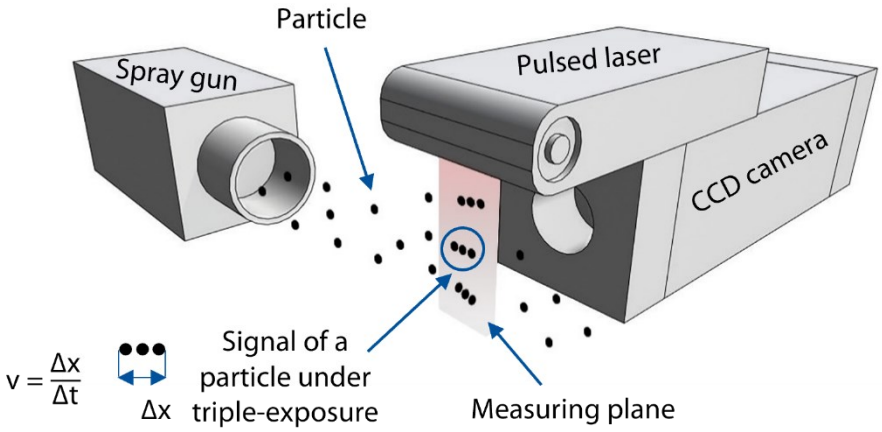

Figure 23: Schematic configuration of the particle diagnostic system HiWatch [BWK+20]

The measuring area with standard optics for HiWatch is 6.5 mm in the spray direction and 9 mm perpendicular to the spray direction, see Figure 24. The depth of field of the camera lens in z direction is about 2 mm. The object space resolution is 6.8 µm/pixel.

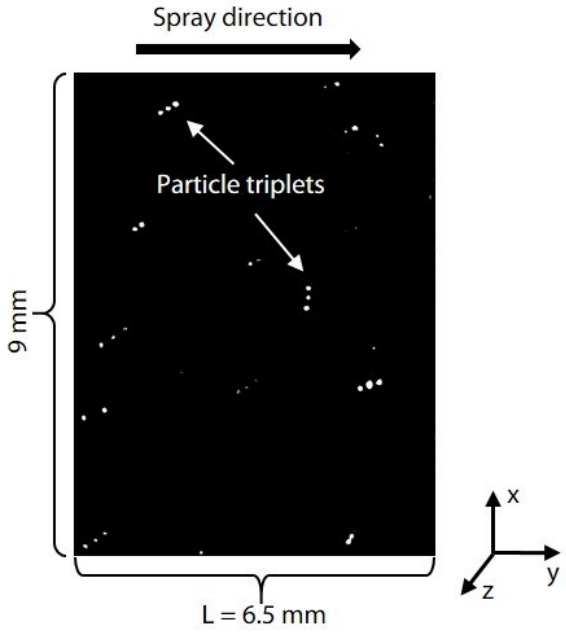

Figure 24: Sample measurement image of the HiWatch at a particular focal plane in the free jet [BWK+20]

The HiWatch determines the particle sizes by the average reflection intensity of the multiple images of a particle. In contrast to the emissivity, the reflectivity of the particles under the applied laser illumination with a wavelength of $\lambda = 810$ nm is almost independent of the particle temperature. Therefore, both hot and cold particles can be captured by the HiWatch. The particle velocities are calculated by the travel distance in the image and the laser pulse time interval. Fast particles are detected with a relatively smaller pulse interval compared to the settings for detecting slower particles. To detect particles in different velocity ranges, the laser pulse interval was set in the range of $0.3 < t_{interval} < 25$ µs and the pulse duration in the range of $0.16 < t_{duration} < 0.5$ µs. The laser settings for the individual measurements were subject to the measurement location in the free jet. Optimal laser settings were adjusted using the live view option to capture as many particle triplets as possible while avoiding overlapping of these triplets.

4.4 PMFR of the Powder Feeder

The determined PMFR in the free jet is validated using the PMFR of the powder feeder as a reference. Figure 25 shows the powder feeder of the spraying system with a schematic drawing of its main components. The spray powder is conveyed by the carrier gas, which is argon in this case. The carrier gas is regulated by a mass flow controller. The stirrer, controlled by the stirrer motor, maintains the powder movement. To discharge any potential static that may build up in the feeder, the hopper is grounded. The PMFR of the powder feeder is controlled volumetrically by the speed of the rotating metering disk that receives the powder from the powder hopper. The operator can control the metering disk speed by changing the setting of the metering disk in terms of percentage. After metering the rotational speed of the disk by the entered percentage value, the powder is transported with the carrier gas through a powder hose, which ends in a particle injector. The powder particles are then injected into the plasma jet.

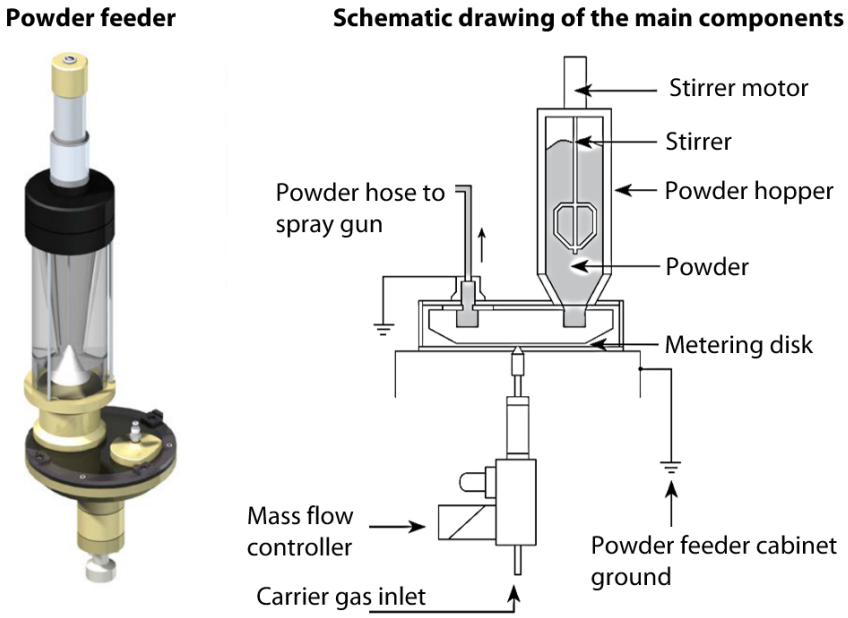

Figure 25: Functional principle of the powder feeder according to [NN23b]

The PMFR of the powder feeder at different metering disk settings was calculated by weighing the amount of powder that was injected into a closed can over a predetermined period of time, see Figure 26. The particle-gas mixture conveyed in the hose is injected into the can from one side. The inserted filter on the other side allows only the gas to escape. The mass flow rate of the feedstock material supplied to the spraying process can be determined by weighing the powder injected into the can within a certain time. The measurements were conducted three times.

Figure 26: Measuring principle of the PMFR of the powder feeder supplied to the process

The argon carrier gas for the Al_2O_3 powder was set to 5.5 SLPM and for the Cu10Al powder to 3.5 SLPM. In each case, the same carrier gas flow was used as in the diagnostic experiments. Figure 27 shows the average PMFR of the powder feeder for the two feedstock powders against different metering disk settings. The results in Figure 27 indicate that the PMFR increases almost linearly with the increase of the metering disk setting.

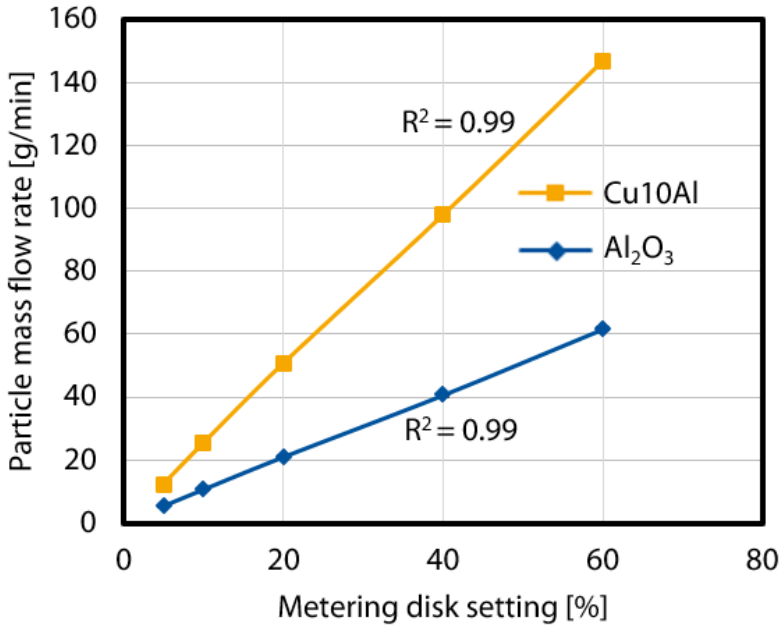

Figure 27: Average PMFR of the powder feeder for the two feedstock powders against different metering disk settings [BWK+20]

4.5 Particle Size Normalization

The particle sizes determined by the HiWatch revealed a deviation compared to the findings of the particle analyzer. One possible explanation is the background subtraction algorithm, which slightly modifies the particle shapes in the recorded images. It should be mentioned that the object space resolution of the HiWatch is not a limitation for the particle detectability. The minimum measurable particle size by the HiWatch is 5 µm. However, due to imaging system non-idealities, the particles appear larger in the images and this leads to an overestimation of the particle sizes, but the position and velocity measurements are not affected by this. The HiWatch system uses the background subtraction algorithm to improve particle detection in the free jet. However, this algorithm may alter the particle shapes in the captured images, resulting in misperceived particle diameters. Additionally, the presence of larger particles may indicate the merging of multiple smaller particles that are melted or semi-melted in the plasma jet. Furthermore, smaller particles may be more challenging to detect by the diagnostic system compared to larger ones.

Hence, to avoid overestimating the PMFR, the measured particle sizes in the entire plasma jet for the both feedstock powders were normalized based on the results of the particle analyzer. To do this, a linear regression was used to normalize the measured particle sizes based on the D [v, 0.05] and D [v, 0.95] of the particles stated in Table 2. Figure 28 shows the volume-based particle size distribution exemplarily for the Al_2O_3 powder using the particle size analyzer as well as the HiWatch diagnostic system before and after normalization. The particle size distribution after normalization shows a good agreement with the distribution measured by the particle analysis system. With respect to this size normalization and the conservation of mass, the particle density in room temperature can be assumed for the in-flight particles as well. Thereby, the vaporization of the particle in the plasma jet has been neglected.

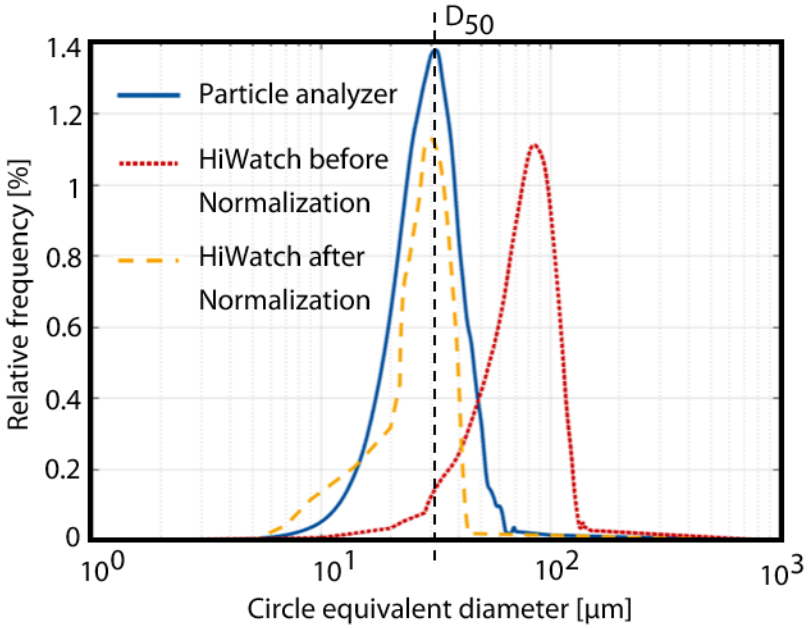

Figure 28: Comparison of exemplarily determined particle sizes before and after normalization by HiWatch with the measurement results of the particle analysis system for Al_2O_3 feedstock powder [BWK+20]

4.6 PMFR Measuring Principle in Free Jet

Experimental footprints were produced to determine the section of the free jet in which most particles are located. The point with maximum particle intensity was then considered as the reference point for the particle diagnostic experiments. Prior to generating the footprints, all substrates were roughened using a grit blasting system. The height profiles of the applied experimental footprints were measured using a confocal laser-scanning microscope. In a next step, these profiles were compared with the digital footprints.

The PMFR of a focal plane from a HiWatch image was calculated based on the following equation:

$$\dot{m} = \sum_{i=1}^{n} \frac{\rho \frac{4}{3} \pi (\frac{D_{p,i}}{2})^3 v_{p,i}}{L} \qquad \text{Eq. 14}$$

- $\dot{m}$ Particle mass flow rate (PMFR)
- ρ Particle density

- D_p Particle diameter
- v_p Particle velocity
- n Number of particles in a HiWatch image
- L Length of a HiWatch image in spray direction

At each focal plane, 250 images were captured and the PMFR of a focal plane corresponds to the average PMFR of all images captured at that focal plane. Figure 29 shows the measured area of the free jet schematically. The free jet transverse section was divided into 15 focal planes in z direction and 3 stages in x direction, see Figure 29.

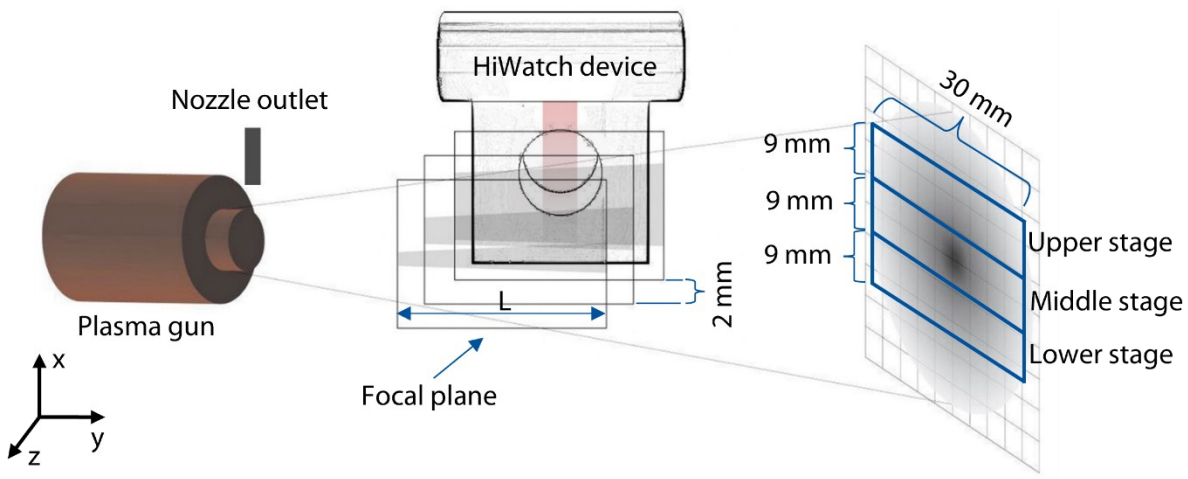

Figure 29: Schematic illustration of the measured area of the free jet by the particle diagnostic device [BWK+20]

The particle diagnostic measurements and the experimental footprints were performed at a spray distance of d = 100 mm. The center of the middle stage corresponds to the point with maximum particle intensity, which was determined by the experimental footprints. At each stage, 15 individual diagnostic measurements were carried out by moving the robot at an increment of 2 mm in z direction, which equals the depth of field of the CCD camera. Therefore, an area of 9×2 mm^2 in xz plane was covered by each individual measurement. Subsequently, the PMFR values for each individual measurement were calculated based on Eq. 14. Finally, the PMFR of the entire measuring area was determined by summation of the obtained PMFR values of the three stages. In this approach, no symmetric distribution of PMFR in the free jet was assumed. It must be pointed out that, as another approach, the PMFR of the focal plane with

maximum particle intensity was also integrated rotationally symmetric over the entire free jet. The results showed an overestimation in the PMFR relative to the PMFR of the powder feeder, which makes the symmetric assumption impermissible.

4.7 Digital Footprint

As mentioned before, the spatial PMFR distribution in the entire free jet is referred to simply as digital footprint. The digital footprints were created based on the determined PMFRs of the all individual measurements described in Figure 29. For better visualization of the digital footprints, the particle positions in each focal plane were considered. The HiWatch system delivers the position of the center of the captured particle triplets in a measurement image, with reference to the upper and left edge of the image. Figure 30 illustrates the covered free jet cross-section by a single measurement together with particle positions schematically. In Figure 30, the particles are sprayed in y direction and the HiWatch captures the particles in z direction. The xz plane was divided into several sections along the x-axis. The PMFR for each section was projected onto the xz plane to create a digital footprint. Afterwards, these digital footprints were compared to the previously produced experimental footprints to validate the results.

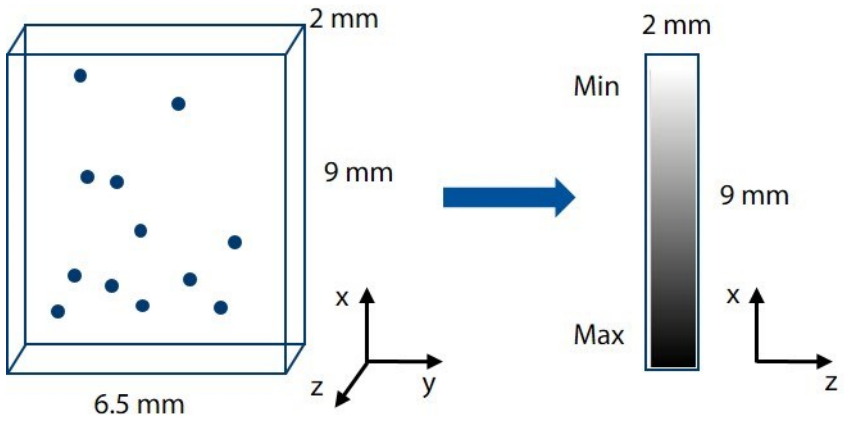

Figure 30: Schematic illustration of an individual measurement in terms of considering the particle positions for precise visualization of the digital footprint [BWK+20]

4.8 PMFR Calibration

Since the particle diagnostic systems are not fully capable to detect all the existing particles in the entire free jet, a calibration of the captured PMFR is necessary. The PMFR directly at the

outlet of the injection nozzle was measured to calibrate the determined PMFR in the free jet, see Figure 31. This allows to capture all injected particles at one focal plane. In this approach, the PMFR at the injection nozzle outlet was calculated and compared with the corresponding PMFR of the powder feeder for different metering disk settings.

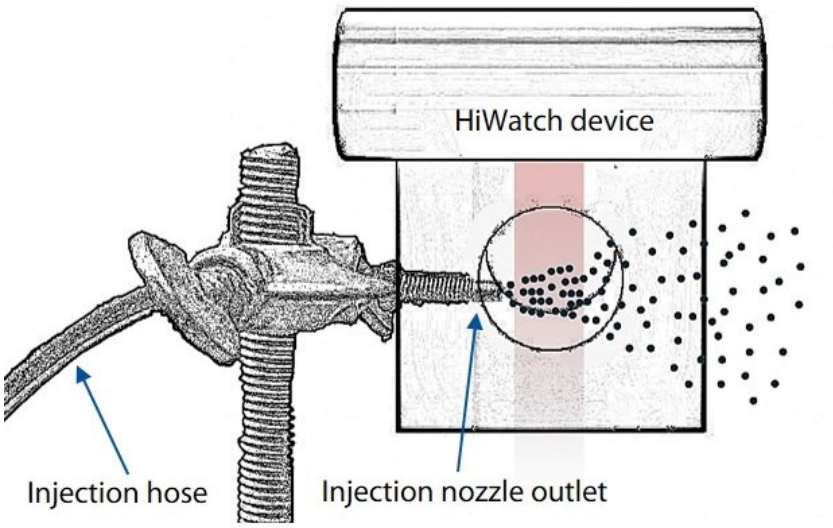

Figure 31: Schematic illustration of capturing the particles directly at the outlet of the injection nozzle [BWK+20]

The PMFR of the Al_2O_3 feedstock material at the injector outlet and the corresponding PMFR of the powder feeder are given in Table 4 for different metering disk settings. The PMFR values at the injector outlet were calculated according to Eq. 14. The corresponding PMFR values of the powder feeder were measured according to the measuring principle described in section 4.4. The proportion of the detected PMFR at the injector outlet, denoted by Ψ_i, is calculated based on dividing the detected PMFR at the injector outlet by the corresponding PMFR of the powder feeder. In other words, this shows the proportion of the particles recorded by the HiWatch at the injector outlet. The index "*i*" in Ψ_i refers to the injector.

The results show that up to a metering disk setting of 5 %, almost a constant proportion of the PMFR was obtained. With higher metering disk settings, due to a dense crowd of particles at the focal plane, the measured values are not reliable. The typical setting of the metering disk, depending on the feedstock material, is between 20 and 30 % in APS. However, in order to avoid

overlapping of the particles and thus incorrect measurements by the HiWatch, the setting of the metering disk was not increased to the maximum typical range.

Table 4: Results of the determined PMFR directly at the injector outlet [BWK+20]

Metering disk [%]	Number of particles in 250 images	PMFR [g/min]		Proportion of the detected PMFR (Ψ_i)
		Injector outlet	Powder feeder	
0.5	345	0.28	0.53	0.52
1	762	0.50	1.08	0.46
2	1,502	0.95	2.12	0.45
5	3,575	2.46	5.5	0.44
10	3,088	2.42	10.75	0.23
20	2,229	1.20	21.08	0.06

The HiWatch images at the injector outlet are shown in Figure 32. Ψ_i represents the proportion of the detected PMFR relative to the PMFR of the powder feeder and MD is the metering disk setting in percentage. It is evident that Ψ_i has been greatly decreased in the case of 10 % and 20 % of MD, since the particle triplets overlap with each other and therefore, the HiWatch cannot reliably evaluate the measured images of the overlapped particles. On the contrary, such a high particle concentration was not observed at a focal plane in the free jet. In addition to the overlapping of the particles, the proportion of the detected particles also depends on the particle diameter, since the larger particles can usually be better detected by the diagnostic equipment. It should be mentioned that the particle size is already considered in the calculation of Ψ_i during the calculation of PMFR by Eq. 14.

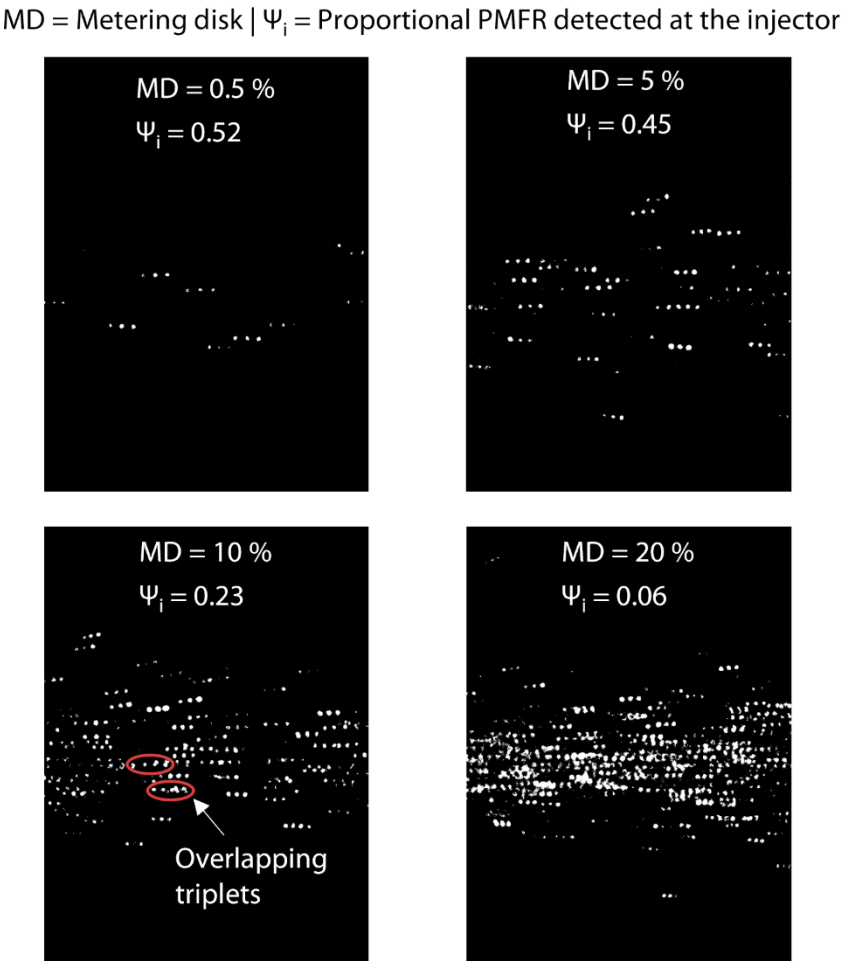

Figure 32: HiWatch images captured directly at the outlet of the injection nozzle

The proportion of the determined PMFR at the injector outlet (Ψ_i) is plotted against the metering disk setting in Figure 33. Up to a metering disk setting of 5 %, almost 47 % of the PMFR of the powder feeder could be obtained. Thus, a factor of roughly 2.1 should be considered to calibrate the PMFR in the free jet. This calibration factor determined at the nozzle outlet was validated afterwards by measuring the PMFR in the free jet in case of different spray powders and plasma generators. These results revealed no dependencies of the calibration factor on the particle size and material. However, this calibration factor may vary for other diagnostic systems. It should be noted that due to the overlapping of the particles directly at the injector outlet, the calibration factor could be measured for a metering disc setting of up to 5 %. In the following results of the PMFR determination in the free jet, it is confirmed that this calibration factor also fits well for higher metering disc settings.

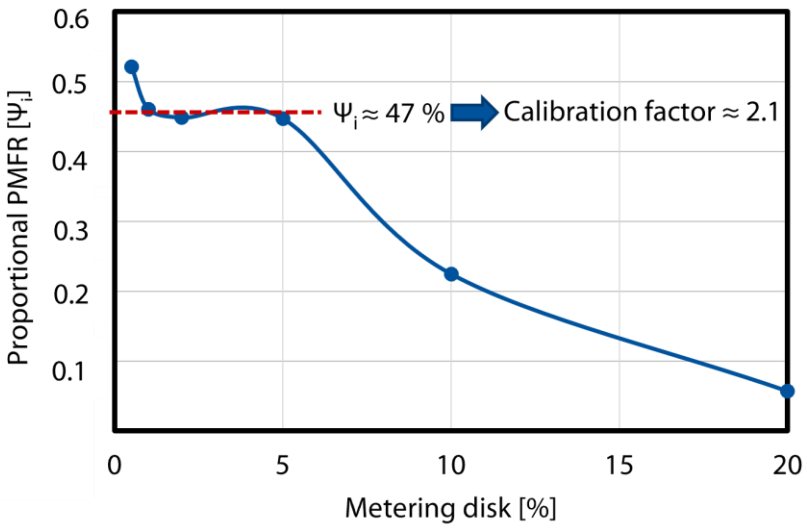

Figure 33: Proportional PMFR detected at the injection nozzle outlet against different metering disk settings [BWK+20]

4.9 Single-Cathode Plasma Torch

The described methodology was implemented in the MATLAB program version R2019b (The MathWorks, Inc., Massachusetts, USA) to calculate the PMFR of each individual measurement and visualize digital footprints based on the PMFR distributions in the free jet. In case of the single-cathode plasma generator, particle diagnostic measurements were carried out for the Al_2O_3 and Cu10Al feedstock powders with different metering disk settings of the powder feeder. The determined PMFR in the free jet and the corresponding PMFR of the powder feeder are given in Table 5. The PMFR in the free jet given in this table was calculated by summation of the PMFR values of all individual measurements based on Eq. 14 without considering the calibration factor at the injector outlet. The corresponding PMFR of the powder feeder was measured according to the description in section 4.4 by weighing the amount of powder that was injected into a closed can within a certain time. The proportion of the recorded PMFR in the free jet, denoted by Ψ_f, is also stated in Table 5. The index "*f*" in Ψ_f refers to the free jet. Ψ_f is calculated based on dividing the detected PMFR in the free jet by the corresponding PMFR of the powder feeder. For this calculation, it is assumed that all injected powder particles enter the free jet.

Table 5: Results of the PMFR determination for different feedstock powders and metering disk settings using single-cathode torch [BWK+20]

Feedstock powder	Metering disk setting [%]	PMFR in free jet [g/min]	PMFR of the powder feeder [g/min]	Proportional PMFR in free jet (Ψ_f)
Al_2O_3	10	5.2	10.75	0.484
Cu10Al	20	25.2	50.66	0.497

The proportion of the detected PMFR in the free jet (Ψ_f) given in Table 5 agrees well with the determined proportional PMFR in Figure 33 directly at the injector outlet ($\Psi_i = 0.47$). This comparison validates the application of the specified calibration factor at the injector outlet also for the PMFR determination in the free jet. Furthermore, with regard to the metering disc settings of 10 % and 20 % used in Table 5, the results confirm that the calibration factor determined for a metering disc setting of up to 5 % at the injector outlet is also well suited for higher metering disc settings for the measurements in the free jet. Considering the average difference between Ψ_f and Ψ_i, the PMFR in the free jet can be estimated with a deviation of less than 5 % compared to the PMFR of the powder feeder. A slight increase in Ψ_f has been observed for the Cu10Al feedstock powder. This can be explained by the fact that the particle diagnostic device can calculate the size of a spherical particle more precisely, since the calculation error for determining the circle equivalent diameter is smaller for a regularly shaped particle. In addition, the HiWatch can determine large particle sizes from a diameter of $d > 50$ µm more accurately. Furthermore, the Cu10Al powder particles possess greater momentum due to their larger particle sizes which leads to less overspray outside the measuring area in comparison with the Al_2O_3 particles.

Figure 34 shows a) the experimentally generated footprint under the laser-scanning microscope and b) the digital footprint based on the PMFR distribution in the free jet for the Al_2O_3 feedstock powder. The profile of the digital footprint closely matches with the experimental footprint. Nonetheless, the higher amounts of PMFR on the boundaries of the digital footprint represent the in-flight particles which have not been deposited on the substrate.

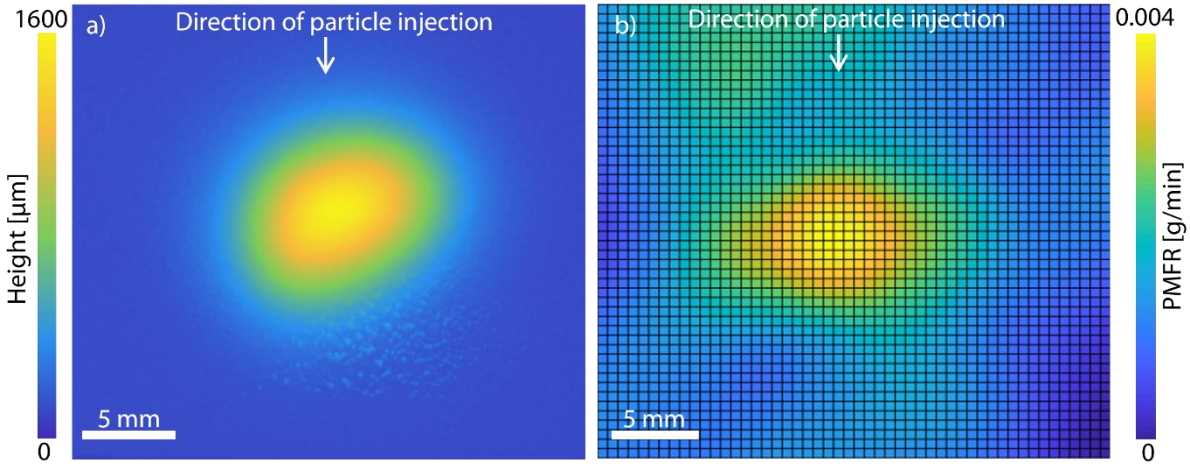

Figure 34: a) Experimental footprint profile under laser-scanning microscope and b) digital footprint using single-cathode gun and Al_2O_3 feedstock powder [BWK+20]

The presence of the unmolten or partially molten in-flight particles is also evident on the periphery of the 3D digital footprint, illustrated in Figure 35. The dense center of the footprint is attributed to the particles with the highest melting ratio. Moving radially out from the center, where fewer particles are dispersed, the plasma temperature decreases relatively and therefore, the particles deposit barely on the substrate.

From the comparison of the experimental and digital footprints in Figure 34, it can be concluded that the most important factor, which affects the particle deposition behavior, is its trajectory. This depends if the particle trajectory lies primarily within the free jet core or outside of it [BBZ+11]. Moreover, the results show that the profile of the PMFR distribution in the plasma jet is not rotationally symmetric about the center.

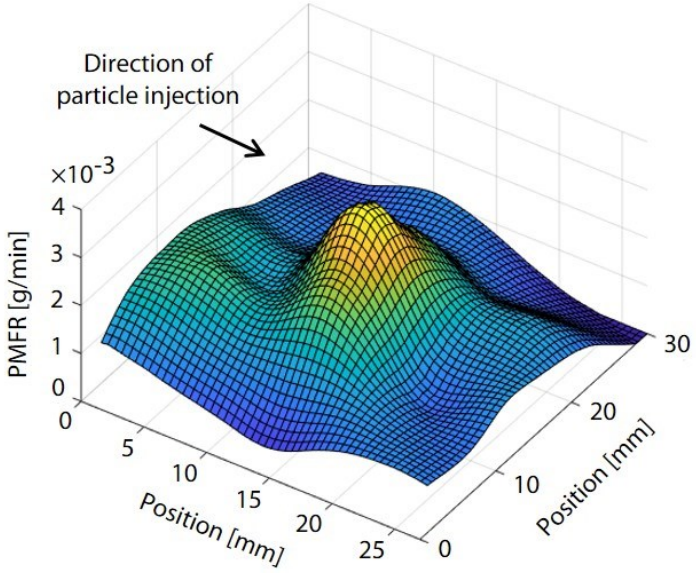

Figure 35: 3D profile of the digital footprint using single-cathode gun and Al_2O_3 feedstock powder [BWK+20]

The profiles of the experimental and digital footprints for the experiments with the Cu10Al feedstock powder and use of the single-cathode gun are illustrated in Figure 36. An irregular bean shaped profile can be observed in both footprints.

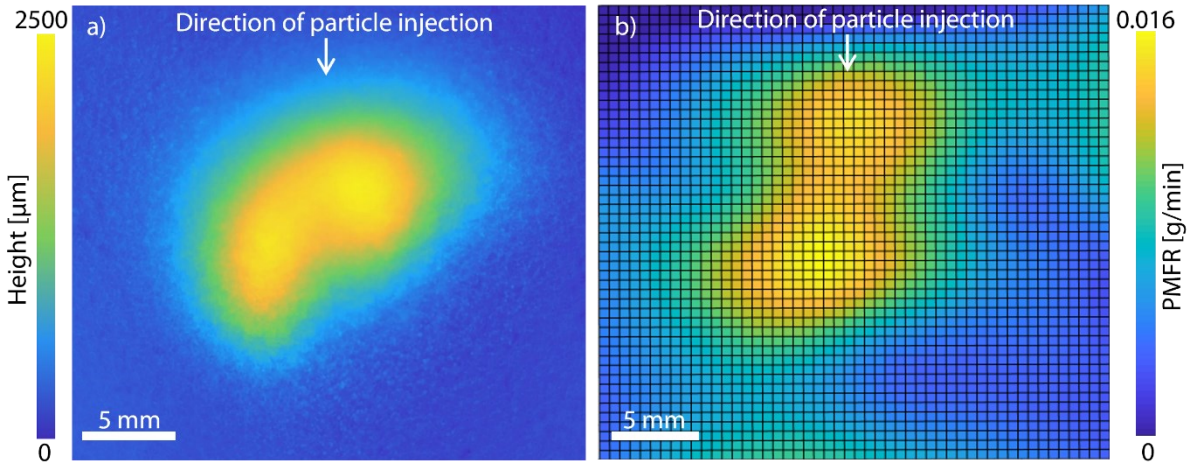

Figure 36: a) Experimental footprint profile under laser-scanning microscope and b) digital footprint using single-cathode gun and Cu10Al feedstock powder [BWK+20]

Figure 37 illustrates the digital footprint in 3D. The two peaks in PMFR values can be attributed to the arc motion fluctuations and restrike inside the torch. Considering the design of the single-cathode plasma gun, the attachment of the electric arc root over the inner surface of the anode can change mainly due to the strong plasma gas flow. This is advantageous to the anode lifetime, since the large heat load can be distributed over the gun nozzle [DGH+01]. However, changing the position of the anode attachment leads to variations in arc length and therefore, results in arc voltage and power fluctuations [LFS09]. Subsequently, these fluctuations inside the single-cathode torch influence the in-flight particle behavior in the plasma jet. It is suggested that the phenomenon of asymmetric footprint is more evident in case of Cu10Al than in Al_2O_3 due to the applied higher metering disc setting and also larger particle size distribution.

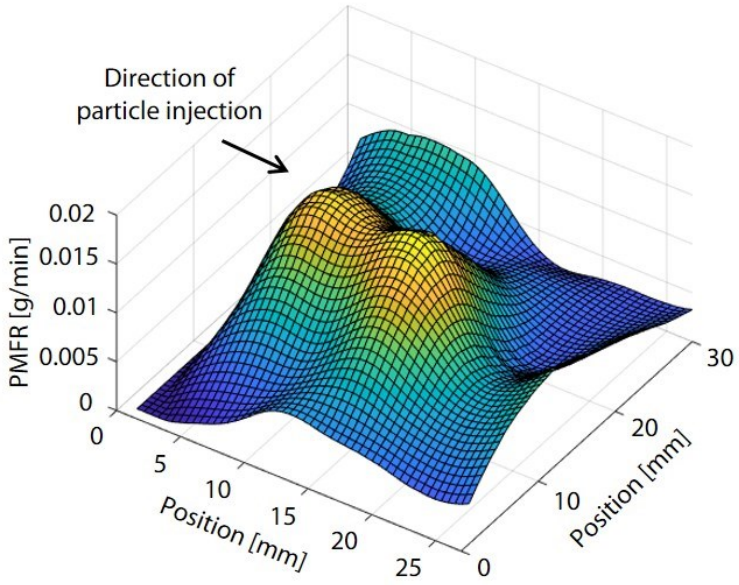

Figure 37: 3D profile of the digital footprint using single-cathode gun and Cu10Al feedstock powder [BWK+20]

The 3D profile of the digital footprint in Figure 37 signifies the capability of the developed method to obtain an asymmetrical spray pattern with regard to the plasma fluctuations. Furthermore, fine particles at the outer part of the free jet tend to oxidize more due to the entrained air from the surrounding atmosphere [Dav04]. This leads to the presence of undeposited particles at the footprint periphery, which are also visible in this figure.

4.10 Three-Cathode Plasma Torch

For the three-cathode plasma gun, diagnostic experiments were conducted using the feedstock material Al_2O_3 for a metering disk setting of 10 %. In this case, the PMFR in the free jet was determined to be 5.6 g/min that leads to a proportional PMFR of $\Psi_f = 0.521$. The results show a minor increase in the proportional PMFR comparing to the single-cathode torch.

Experimental and digital footprints resulting from the three-cathode plasma gun are shown in Figure 38. A nearly symmetric and round-shaped spray pattern is visible in both cases. This can be explained through different construction concepts of the plasma guns. The three-cathode plasma gun utilizes a triple axially symmetrical arc system, which results in decreasing of the local heat load to the anode ring [VMT+15]. Moreover, it features a relative stable plasma jet due to less fluctuation of the electric arc length inside the torch [BBZ+11]. This leads to a homogenous heat treatment of the powder particles in the free jet and consequently a more uniform deposition pattern.

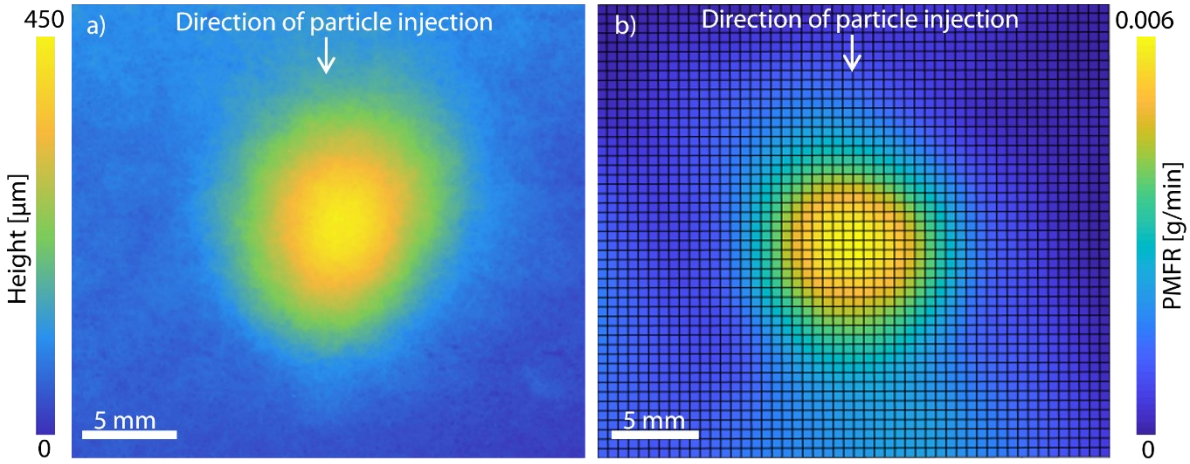

Figure 38: a) Experimental footprint profile under laser-scanning microscope and b) digital footprint using three-cathode gun and Al_2O_3 feedstock powder [BWK+20]

The 3D illustration of the digital footprint is depicted in Figure 39. The PMFR values at the outer part of the footprint, in contrast to the one with the single-cathode torch, are almost homogenously near zero. This observation demonstrates the advantage of the multi-arc plasma

chamber geometry with regard to the stability of the plasma jet under the applied process parameters.

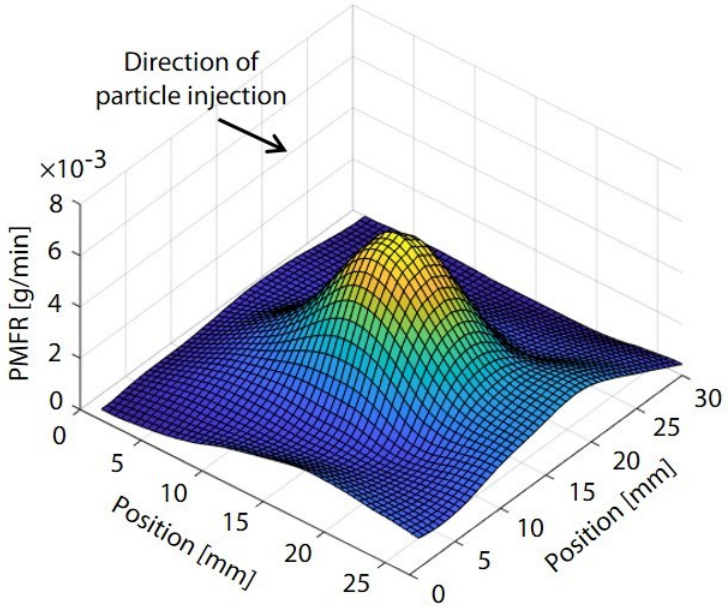

Figure 39: 3D profile of the digital footprint using three-cathode gun and Al_2O_3 feedstock powder [BWK+20]

The cascaded design of the three-cathode plasma gun results in a ring-shaped high viscous flow surrounding the plasma jet that helps the particle trajectories to stay in the high temperature core of the plasma jet, see Figure 40 [BÖS+17]. The process parameters, such as electric current and plasma gas flow rate, have strong influence on the position and intensity of the surrounding viscous flow [BÖ16]. Hence, the multi-arc spray system allows a confining path for particle injection toward the center of the plume, which results in the most efficient particle heating in the free jet [SRL+08]. Consequently, the footprint illustrated in Figure 39 shows less overspray particles.

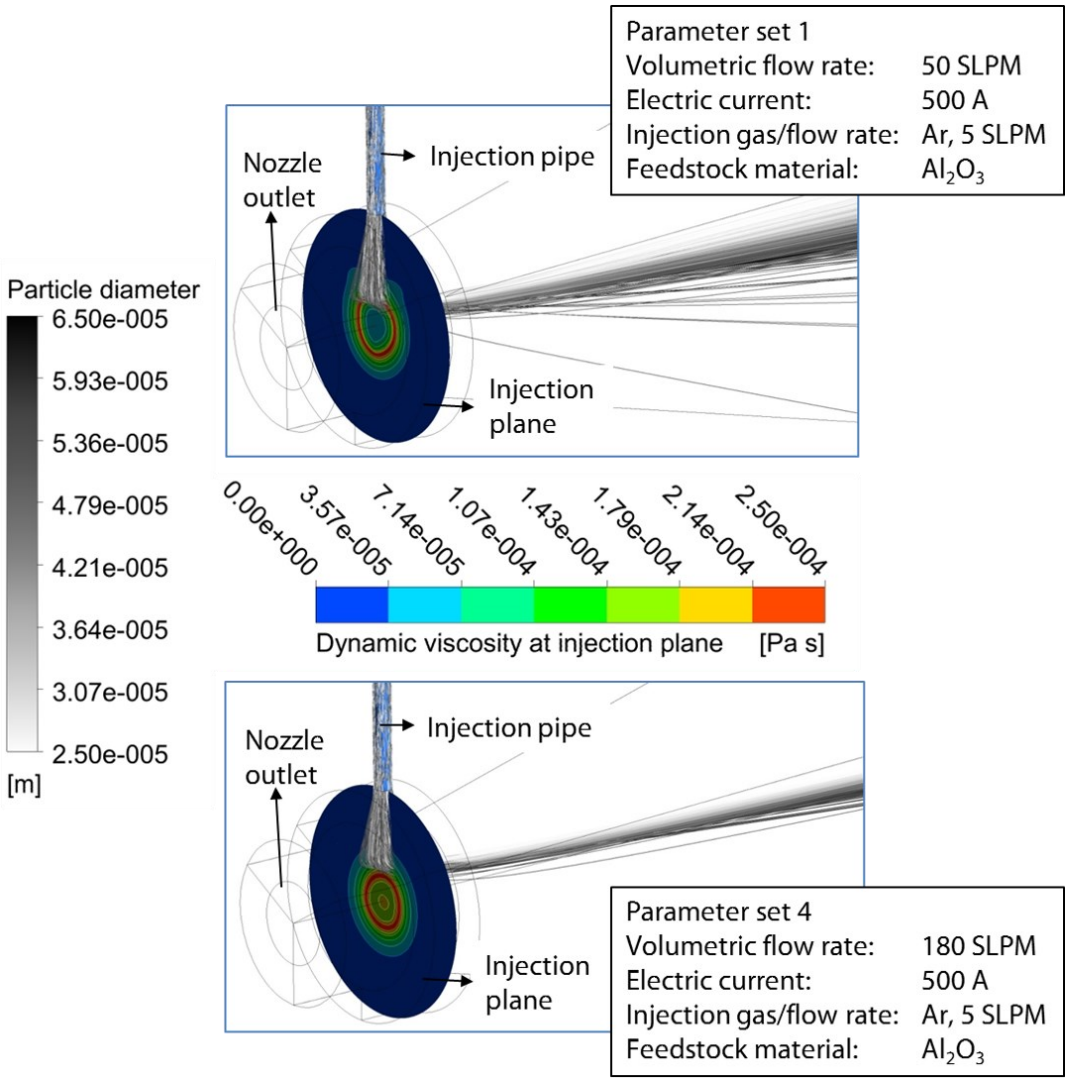

Figure 40: Distribution of dynamic viscosity of process gas over injection plane; ring-shaped high viscous flow surrounding the plasma jet [BÖS+17]

4.11 Conclusion

A novel methodology was presented to estimate the particle mass flow rate (PMFR) in the plasma jet based on capturing the in-flight particle properties at different focal planes. The approach is capable of estimating the PMFR in the free jet with a deviation of less than 5 % compared to the PMFR of the powder feeder. Furthermore, the key benefit of the developed approach is that no rotationally symmetric particle flow has been assumed. This makes the determined PMFR distribution more precise. The results could be replicated with different feedstock powders and plasma guns, demonstrating the capability of the developed method. The spatial PMFR distributions throughout the free jet, referred to as digital footprint, showed

a good agreement with the height profile of the corresponding experimental footprints. Moreover, the results indicated a more accurate determination of the PMFR in the case of utilizing spherical feedstock powder with relatively large particles as well as employing a three-cathode plasma gun. By using the findings of the PMFR estimation in the free jet, the local deposition efficiency on the substrate can be determined according to the next chapter.

5 Local Deposition Efficiency (LDE)

In this chapter, a novel methodology is introduced for in situ determination of spatially resolved deposition efficiencies on the substrate, namely Local Deposition Efficiency (LDE). The results of this chapter have been already published in [BWH+20]. The motivation for using LDE is to generate a sufficient amount of data for learning algorithms, while generating that much data for ex situ measurements of global DE and their corresponding particle properties would be impractical. In addition, LDE data sets allow the entire plasma jet to be considered, instead of its centerline, as it is the case for classical diagnostic measurements. This consideration of widely distributed particle trajectories in the plasma jet can improve the accuracy of deriving correlations between the particle properties and DE.

The spatial distribution of PMFR from the previous section is used in combination with the height profile of the respective experimental footprint to calculate the LDE. Subsequently, the interdependencies between the measured in-flight particle properties and the LDE are studied by SVM method. The generated data sets of LDE together with the corresponding particle properties are used later in Chapter 7 to develop an ANFIS model for prediction of deposition efficiency in plasma spraying.

5.1 Spray Parameters and Feedstock Material

The same experimental setup for the three-cathode plasma generator TriplexPro™-210, described in Chapter 4, is also used here. The main spray parameters are listed in Table 6. The electrical current of the plasma generator was set to 500 A. Argon with the flow rate of 60 SLPM was used as the primary plasma gas. The distance between the particle injector tip and the plasma jet centerline axis was d = 12 mm. The commercially available Al_2O_3 feedstock material (AMDRY 6062, Oerlikon Metco) was used. The properties of this alumina feedstock powder were given in Table 2 in section 4.1.

Table 6: Spray parameters for the three-cathode plasma gun

Parameter	Value
Current [A]	500
Input power [kW]	48.4
Voltage [V]	99.3
Argon [SLPM]	60
Carrier gas [SLPM]	5.5
Nozzle diameter [mm]	9
Powder feed rate [g/min]	11

5.2 Particle Diagnostics

The setup of the particle diagnostics for measuring particle size and velocity is similar to that of the PMFR estimation in Chapter 4. The difference lies in the evaluation of the measurement data, in a way that the captured particles in a HiWatch image are segmented into five parts regarding their positions to visualize the spatial distribution of the particle properties precisely. Furthermore, in this experimental setup, the in-flight particle temperatures are also measured on a specific transverse section of the free jet using the particle diagnostic system DPV-2000. The focus here is on the analysis of the distribution of the in-flight particle properties rather than on the PMFR measurements in the previous chapter. Consequently, the correlations between the particle properties and LDE are investigated. In addition, in the data evaluation of this chapter, the number of particles detected by the HiWatch and DPV diagnostic systems is also analyzed and compared. The aforementioned points are explored in more detail below.

The particle diagnostic system HiWatch CS was employed to determine the size and velocity of the in-flight particles. This device utilizes a pulsed diode laser to capture the particles on a particular transverse section of the free jet based on triple-exposure imaging of each particle. The measuring area for a single measurement is 6.5×9 mm^2. The depth of field of the camera lens is about 2 mm in z-direction, see Figure 41-a. The pulsed laser illumination allows each particle to be captured three times in an image. Along with measuring particle sizes and velocities, the positions of the captured triplets are considered to accurately visualize the spatial distribution of the particle properties. To achieve this, the xz-plane in Figure 41-a was divided into five sections along the x-axis. The particles captured in each measurement were then

divided into the designated sections based on their x-position. Multiple measurements were carried out to cover the entire domain of the free jet. Figure 41-b displays a schematic illustration of the area of the free jet measured by the HiWatch. In this illustration, the particles are sprayed in y-direction. The transverse section of the free jet was divided into 15 focal planes in z-direction and 3 stages in x-direction. At each stage, 15 individual diagnostic measurements were carried out by moving the robot incrementally by $\Delta z = 2$ mm in z-direction. The interval between two consecutive measurements is equivalent to the depth of field of the CCD camera.

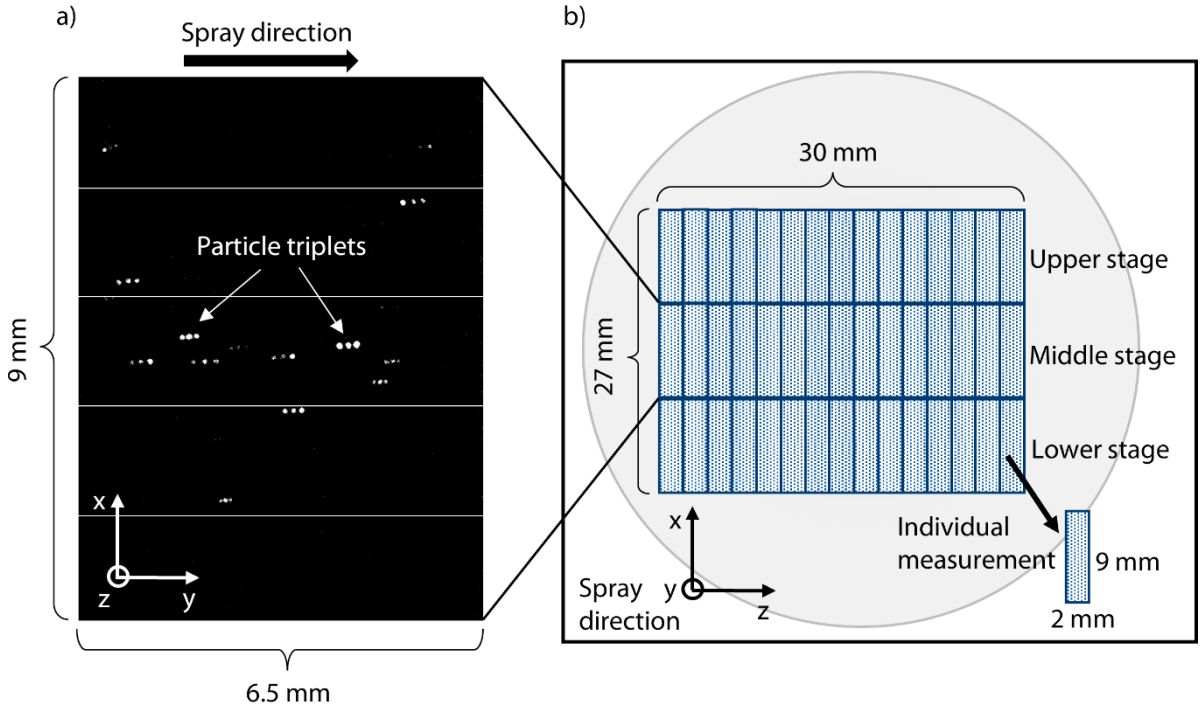

Figure 41: a) An exemplary measurement image of HiWatch at a focal plane in the plasma jet. The captured particles are schematically segmented into five parts along the x-axis to visualize the spatial distribution of the particle properties precisely. b) schematic illustration of the measured area of the plasma jet by diagnostic experiments [BWH+20]

As previously stated, the particles captured at each stage were divided into 5 sections based on their x-position for more accurate visualization of the spatial distributions. At each focal plane, 250 images were taken. The particle size and velocity of a focal plane correspond to the respective average values of the images captured at that focal plane. The spatial distributions for particle size and velocity were then obtained based on all individual measurements in the entire

measuring area of 27 × 30 mm², resulting in 225 measurement points on a grid of 15 × 15 in the plasma jet. The particle diagnostic measurements were performed at the same stand-off distance of y = 100 mm as the experimental footprints. The center of the middle stage corresponds to the point with highest particle intensity, which was determined beforehand by the experimental footprints.

The optical particle diagnostic system DPV-2000 (Tecnar Automation Ltd., St. Bruno, QC, Canada) was utilized to measure the in-flight particle temperatures. The DPV-2000 system uses the principle of two-wavelength pyrometry to measure the surface temperature of particles in the spray plume [MVS07]. The diagnostic experiments to determine the spatial distribution of particle temperatures were performed on a 30 × 30 mm² measurement grid normal to the gun axis at a stand-off distance of 100 mm. A step size of Δx = Δz = 2 mm was selected between each successive measurement. The total measurement area contained 225 grid points. The measurement time for each grid point was 5 seconds. Before beginning the experiments, the central point of the measurement grid was adjusted to the maximum particle flux using the DPV-2000 autocenter function.

5.3 Spatial Distribution of Particle Properties

The programming software MATLAB was used to implement the described method and visualize the spatial distribution of the particle properties in the plasma jet. Figure 42 shows the normalized particle number flux detected by the diagnostic systems a) HiWatch and b) DPV for the entire free jet measurements. Since the two diagnostic systems have different measurement volumes, normalization of the particle number flux is necessary to ensure comparability. It is evident that HiWatch has captured more particles than DPV, since it has a relatively larger measurement volume. However, it should be considered that DPV is unable to capture the cold particles without a laser for particle illumination. Thus, the HiWatch particle diagnostic system was chosen to measure the size and velocity of the particles because of its ability to detect both cold and hot particles with a relatively larger measurement volume.

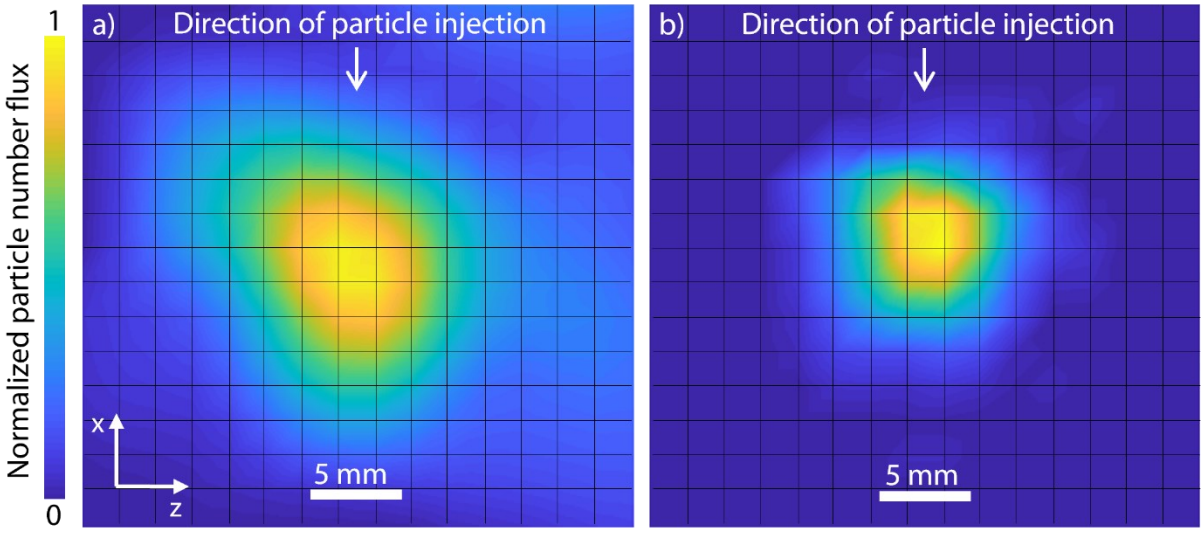

Figure 42: Normalized particle number flux detected by a) HiWatch and b) DPV in the entire free jet at a stand-off distance of y = 100 mm [BWH+20]

Figure 43 illustrates the spatial distribution of the in-flight particle velocities at a stand-off distance of y = 100 mm. The spatial distribution of the in-flight particle velocities shows that this distribution is not symmetrical about the gun axis, considering the measurement points at the upstream edge of the plasma jet. With increasing the radial distance from the side of particle injection to the bottom of the plasma jet, the particle velocities first increased to a maximum on the center and then decreased.

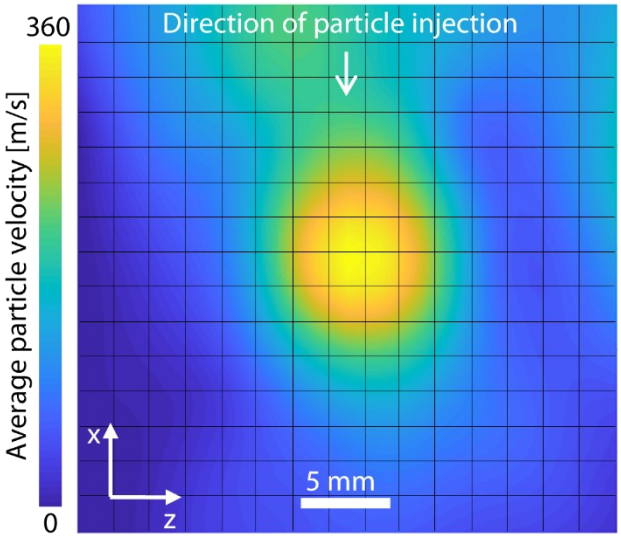

Figure 43: Spatial distribution of the in-flight particle velocities at a stand-off distance of y = 100 mm using HiWatch [BWH+20]

Due to the geometry of the plasma generator, there is a swirling plasma gas flow at the torch exit [SBD+06]. This swirling flow has consequently an influence on the in-flight particle trajectories and leads to asymmetrical particle velocity distribution [WFC00]. Moreover, this spatial distribution shows that in the area of the injection head, the particles with relatively higher velocities were measured.

Figure 44 shows the spatial distribution of the in-flight particle sizes. The particle size distribution indicates that the large particles were concentrated at the center of the free jet. This can be explained with particle momentum. Particles with larger diameters possess relatively greater momentum, which leads to a deeper penetration into the plasma jet [QFL08].

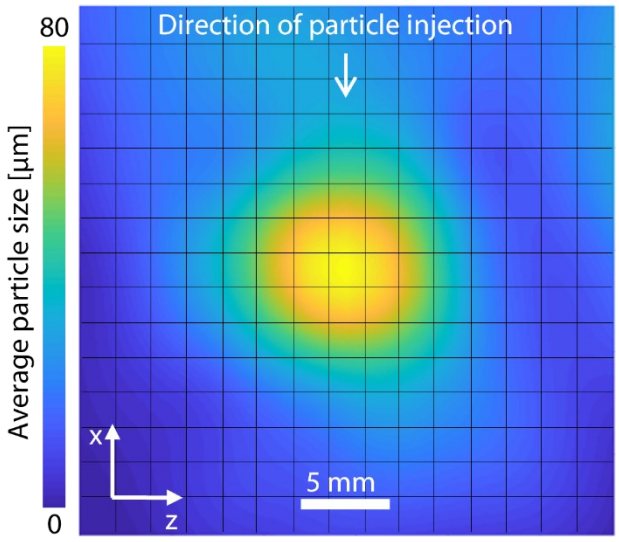

Figure 44: Spatial distribution of the in-flight particle sizes at a stand-off distance of y = 100 mm using HiWatch [BWH+20]

The median size of the captured particles is calculated to be D_{50} = 39.5 µm. This shows that the HiWatch has overestimated the particle sizes, when compared to the particle analyzer results given in Table 2 (D_{50} = 31.85 µm). One possible explanation for this, is the background subtraction algorithm, which the HiWatch system uses to increase the particle detectability. This background subtraction algorithm slightly changes the particle shapes in the recorded images and could therefore lead to misperceived particle diameters. Another explanation for this size deviation could be the angular and blocky morphology of the particles. The unregularly

shaped particles rotate in the view field of the HiWatch, while these are immobile under microscope. This leads to some calculation error in determining the circle equivalent diameter of the particles. Moreover, the larger particles could be a sign of consolidated particles in the plasma jet, consisting of multiple smaller particles that pack together. In addition, smaller particles can be captured harder than large ones by the diagnostic system.

Figure 45 displays the spatial distribution of the in-flight particle temperatures on a transverse section of the plasma jet at a stand-off distance of y = 100 mm. The results show that the particles with highest temperature were positioned in the center of the plasma jet, where the largest and fastest particles were also located. Figure 45 also reveals a homogenous heat treatment of the powder particles in the plasma jet by the three-cathode plasma generator, resulting in a uniform deposition pattern.

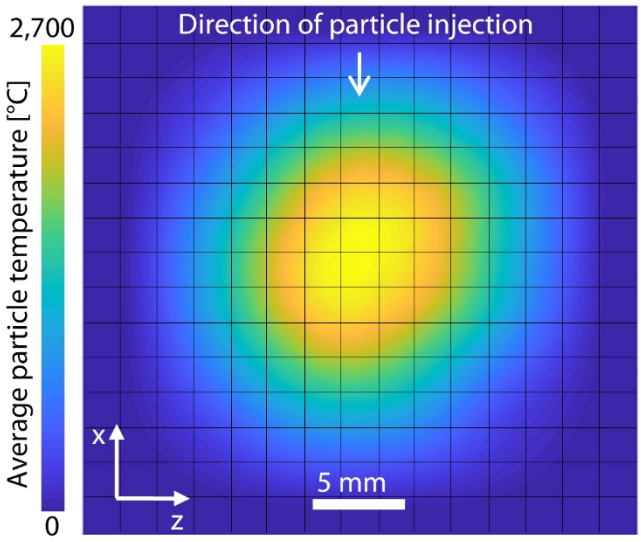

Figure 45: Spatial distribution of the in-flight particle temperatures at a stand-off distance of y = 100 mm using DPV [BWH+20]

The spatial distributions of the number of particles with velocities above v = 200 m/s, sizes greater than D = 50 µm and temperatures above T = 2,000 °C are shown in Figure 46-a, b and c respectively. These thresholds in particle properties are determined based on the LDE results in the next section. The results reveal that mostly the center of the free jet has a dense crowd of particles with velocities, sizes and temperatures above the defined thresholds.

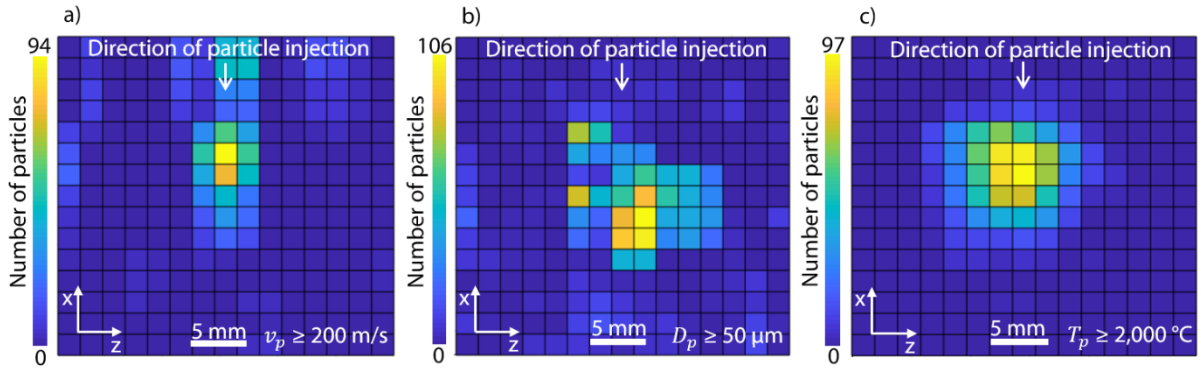

Figure 46: Spatial distribution of the number of particles in case of a) velocities above v_p = 200 m/s, b) sizes above D_p = 50 µm and c) temperatures above T_p = 2,000 °C according to [BWH+20]

5.4 Calculation of LDE

Experimental footprints were generated as a reference to investigate the LDE of the particles. By comparing the height of the experimental footprint with the above measured particle properties, only limited conclusions in terms of the particle DE can be drawn. Therefore, a methodology is introduced to investigate the correlations between the in-flight particle properties and their LDE on the substrate. For this purpose, the spatial distribution of the in-flight PMFR from Chapter 4 has been considered. Figure 47 shows the spatial distribution of the PMFR resulting from the three-cathode plasma gun and alumina spray powder.

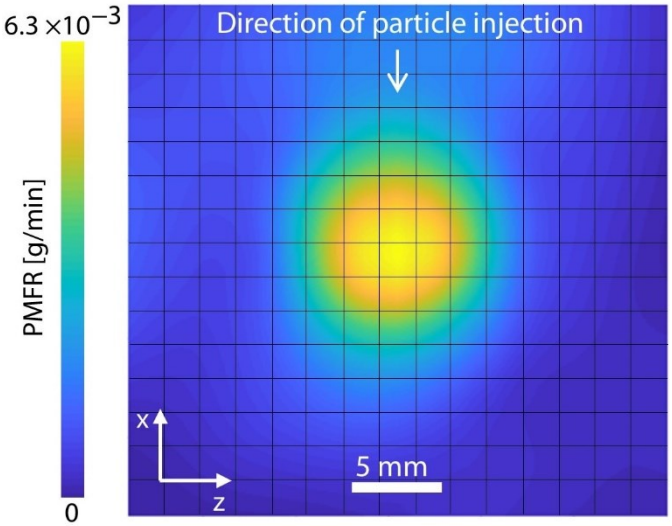

Figure 47: Spatial distribution of the in-flight PMFR at a stand-off distance of y = 100 mm

For the next step to calculate the LDE, the values of the height profile of the respective experimental footprint measured by the laser-scanning microscope were used to calculate the mass of the feedstock material deposited on the substrate locally. As mentioned earlier, the entire measuring area of the free jet transverse section was 27 × 30 mm², containing 225 measurement points on a grid of 15 × 15. The same segmentation was done on the substrate by dividing the xz-plane of the footprint height profile in 225 elements, see Figure 48-a. The mass of the deposited feedstock material on each element (m_e) is estimated based on Eq. 15.

$$m_e = H_e\, A_e\, \rho \qquad \text{Eq. 15}$$

- m_e Deposited mass on each element
- H_e Average height of the footprint on each element
- A_e Area of each element
- ρ Density of the feedstock material

The common porosity range of plasma sprayed ceramic coatings vary between 5-10 % [VDS+07]. As it is impractical to measure the porosity of the footprint for each measurement element, zero porosity is assumed for the whole domain. Consequently, it should be clarified that the calculated LDE might be overestimated in some places due to zero porosity assumption.

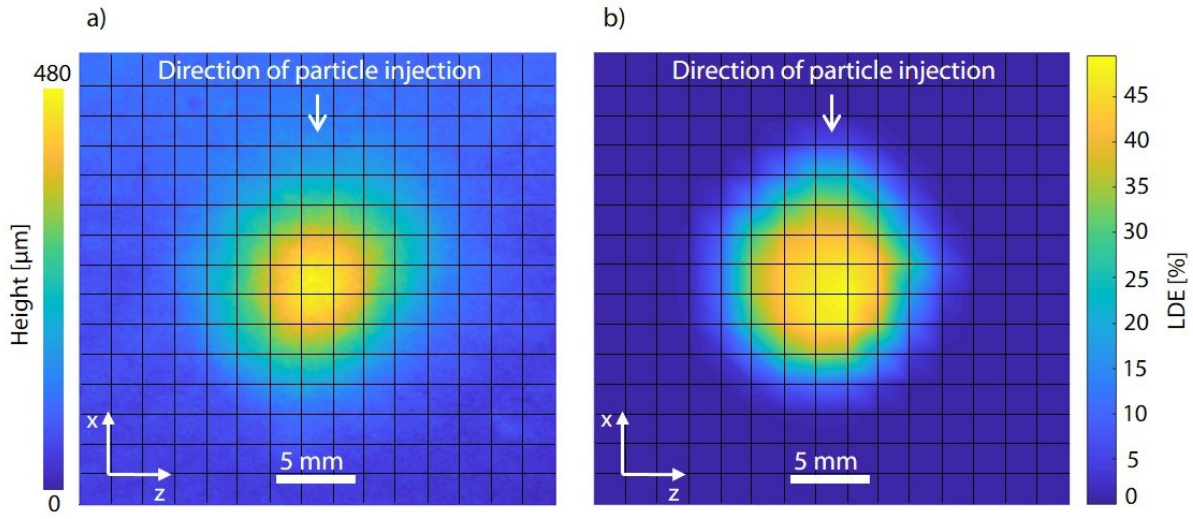

Figure 48: a) Segmented height profile of the experimental footprint in xz-plane under laser-scanning microscope and b) spatial distribution of LDE in the entire jet [BWH+20]

The LDEs of the particles for each element are calculated in percentage terms based on Eq. 16.

$$LDE = \frac{m_e}{\dot{m}\, t}\, 100 \qquad \text{Eq. 16}$$

- m_e Deposited mass on each element
- ṁ Particle mass flow rate (PMFR)
- t Time for generation of experimental footprint

It must be pointed out that the calculated LDE is an estimation of the absolute DE based on the norm [DIN17]. Figure 48-b shows the distribution of the calculated LDE in the entire free jet. It is evident that the particles at the free jet center, on the contrary to the outer part of the free jet, revealed a higher LDE.

5.5 Correlations between Particle Properties & LDE

In this section, the correlations between the particle properties in the plasma jet and the calculated LDE on the substrate are investigated. To do this, first different pairs of particle properties are visualized with their corresponding LDE values. Afterwards, a nonlinear regression model using SVM has been developed to investigate the relationships between the particle properties and LDE.

The plot of the particle velocities, particle sizes and LDE is presented in Figure 49. The results demonstrate that the large particles with relatively high particle velocities showed a higher LDE. With the assumption of LDE > 25 % for a relatively good deposition efficiency, it can be concluded that the particles with a minimum velocity of roughly v_p = 200 m/s in combination with a minimum size of roughly D_p = 50 µm deposited well on the substrate. The ratio of the radiated heat to the latent heat, which is proportional to the surface to volume ratio, suggests overheating of larger particles compared to the smaller ones [BÖK+20]. This fact explains the result that the particles with larger diameters showed a higher LDE, since they are melted better in the plasma jet.

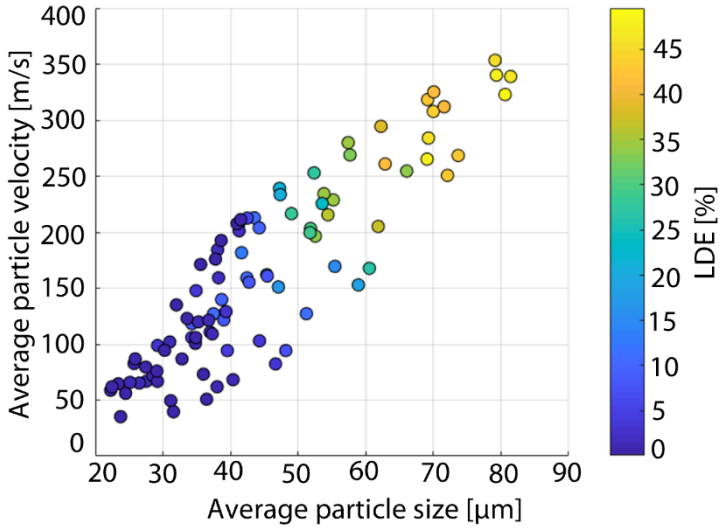

Figure 49: Plot of the particle velocities, particle sizes and LDE [BWH+20]

Figure 50 illustrates the correlations among the particle velocities, particle temperatures and LDE. It is evident that some particles, despite having relatively small velocities, have deposited on the substrate. The plasma jet allowed these particles to reach the minimum temperature for deposition. This concludes that particle temperature is an important factor for evaluating the LDE of ceramic particles. Following this, the particles needed roughly a temperature of T_p = 2,000 °C and a velocity of v_p = 200 m/s to deposit well on the substrate.

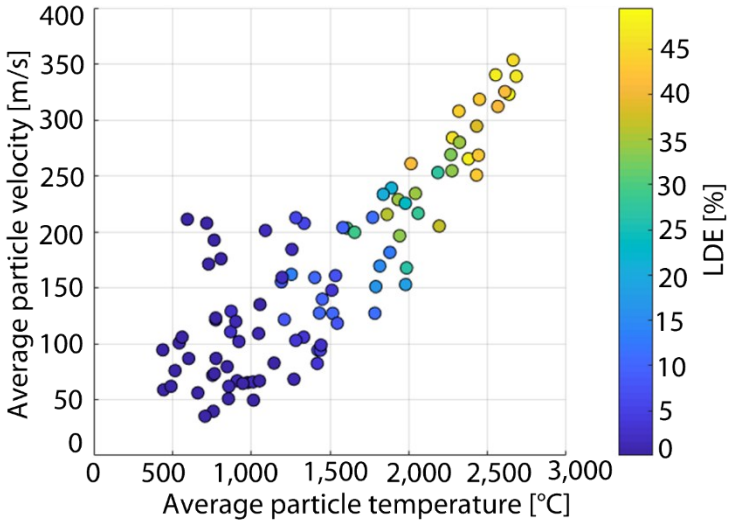

Figure 50: Plot of the particle velocities, particle temperatures and LDE [BWH+20]

The particle sizes and particle temperatures together with their corresponding LDE are plotted in Figure 51. The particles with relatively larger diameters, exhibited a better LDE than the smaller particles surrounding the free jet. This observation can be explained through the fact that the cascaded design of the three-cathode plasma gun allows larger particles to stay in the high temperature core of the plasma jet, which results the best LDE in the free jet [SRL+08, BÖ16]. The results show that the particles with a minimum diameter of almost D_p = 50 µm in combination of a minimum temperature of almost T_p = 2,000 °C had a good chance to deposit on the substrate. This temperature threshold is near the melting temperature of the alumina, which amounts to T_m = 2,072 °C.

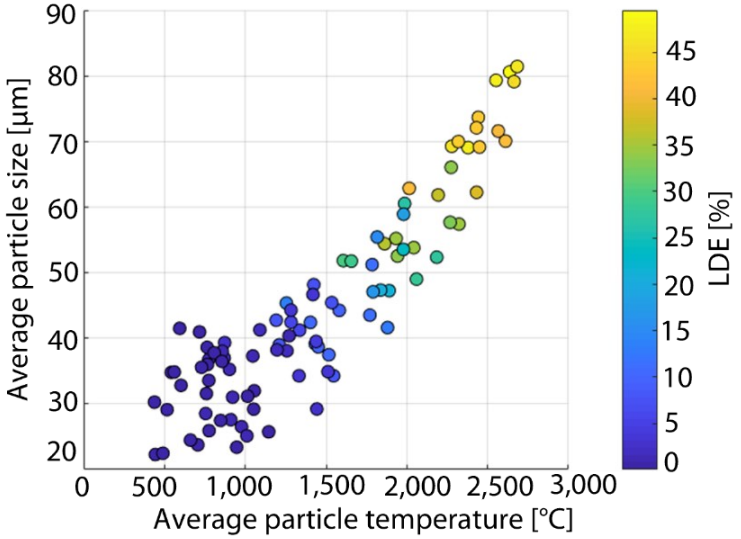

Figure 51: Plot of the particle sizes, particle temperatures and LDE [BWH+20]

In order to reveal the interdependencies between the particle properties and the calculated LDE quantitatively, a nonlinear regression model is developed. The particle sizes, velocities and temperatures are considered as input variables and LDE is considered as a response variable. In this model, SVM method with a Gaussian kernel function is employed in the MATLAB environment to predict the correlations between the input and response variables. The accuracy metrics of the model, namely root mean square error (RMSE) and coefficient of determination, are calculated to be RMSE = 2.85 [%] and R-Squared = 0.97 respectively. Figure 52 shows the 3D scatter plot of the variables resulted from the regression model. These results confirm nonlinear interdependencies among the particle properties and the LDE values.

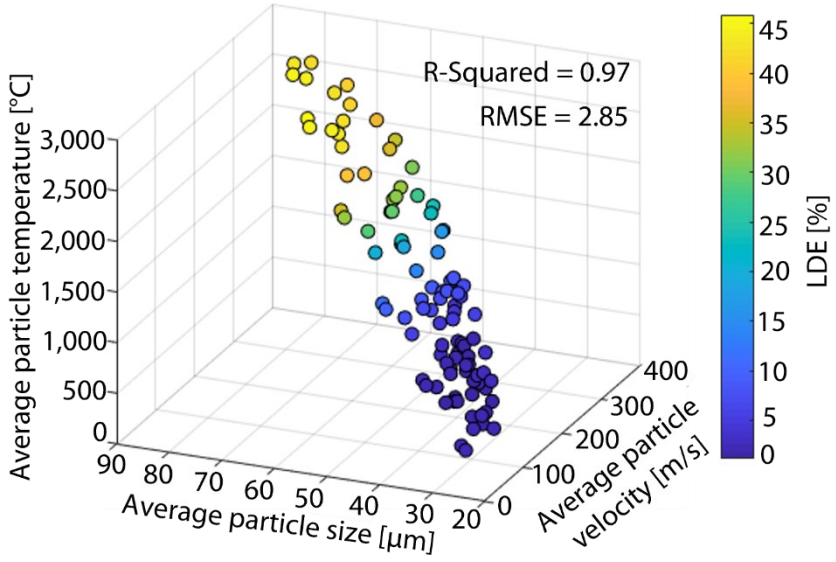

Figure 52: Nonlinear regression of the particle properties and LDE using SVM [BWH+20]

5.6 Conclusion

In this chapter a methodology was presented to determine the spatially resolved deposition efficiencies on the substrate, namely local deposition efficiency. Particle diagnostic experiments were carried out using a three-cathode plasma generator and alumina as feedstock powder. This type of plasma generator has been considered for LDE determination, since it offers higher process stability that minimizes process-related fluctuations during the particle diagnostic measurements. The spatial distribution of the in-flight PMFR, presented in Chapter 4, and the local deposited mass on the substrate were employed to calculate LDE. The spatial distribution of the particle properties showed that the larger particles with higher velocities and temperatures penetrated deeply in the center of the plasma jet. Subsequently, these particles revealed relatively higher LDE compared with the particles at the periphery of the free jet.

The developed methodology for determination of LDE improves the understanding of particle adhesion conditions on the substrate. Moreover, the results of this technique have provided relatively large data sets of particle properties and LDE, covering the entire free jet transverse section. These data sets are used later in Chapter 7 as training data for the ANFIS model to find the correlations between particle properties and DE. An approach to produce data sets of particle properties along with their corresponding process parameters by using simulations of the plasma jet is discussed in the next chapter.

6 Prediction of Particle Properties using Support Vector Machine

The coating process in plasma spraying is associated with many complex physical phenomena. Due to the large number of parameters involved in this coating technology as well as the nonlinear relationships between these parameters, precise control and optimization of the process is a lengthy and expensive undertaking. Not all of the influencing parameters can be controlled, because on the one hand the effect of many variables on the coating process is not quantitatively measurable, and on the other hand the technical possibilities for an adequate process monitoring are still lacking. Therefore, employing computer-aided methods, such as ML approaches, is essential to quantify these complex relationships and subsequently enhance the process reproducibility.

In this chapter, SVM models are presented to predict in-flight particle properties from process parameters in plasma spraying. To train the SVM models, different data sets from a CFD model of the plasma jet have been employed. The motivation of using simulation results is the opportunity to cover a broad range of process parameters, while providing that much experimental data is barely possible. The increasingly sophisticated CFD models in plasma spraying have the drawback of requiring considerable calculation time. Developing ML algorithms with simulation data sets is at the same time a promising possibility for substitution of the computationally expensive CFD simulations.

A precise prediction of the properties of each *individual* particle in the stochastic process of plasma spraying cannot be anticipated using the ML methods at hand. This is due to the randomness of the particle behavior caused by the turbulence of the plasma flow and the collisions of the particles with each other and with the inner wall of the narrow particle injector. Therefore, the final particle properties are highly sensitive to their initial position. However, the accurate prediction of *average* particle properties serves as a key performance indicator in plasma spraying and can significantly help, for example, in investigating the interrelationships between process parameters and DE. Hence, the objective of the SVM models is to accurately predict the average particle behavior depending on different sets of process parameters.

To develop the SVM models, several data sets comprising various process parameters as well as in-flight particle velocities, temperatures and positions were extracted from a CFD model of the plasma jet. The data preparation was carried out using two different Design of Experiments

(DoE) methods, namely Central Composite Design (CCD) and Latin Hypercube Sampling (LHS), to cover a set of representative process parameters for training the ML models. Afterwards, the prepared data were fed into SVM models to predict the particle properties. The results presented in this chapter have been already published in [BWH+21].

6.1 Numerical Modeling

The simulation data sets of this work are obtained from a former numerical model, performed at the IOT at RWTH Aachen. To resolve different physical phenomena and reduce the model complexity of the entire system, the plasma spraying process is divided into two sub-processes that are modeled separately: the plasma generator model and the plasma jet model. In the plasma generator model, the flow characteristics at the plasma generator outlet including the temperature and velocity profiles of the plasma gas as well as the profiles of turbulent kinetic energy and turbulent eddy dissipation are determined. By using these determined profiles as a boundary condition at the inlet of the plasma jet model, the two sub-models are coupled. The computational domain and the boundary conditions of the plasma generator model are presented in Figure 53. The geometry of the torch nozzle has a threefold axial symmetry. Hence, one-third of the whole geometry was used as the computational domain.

A two-equation Shear Stress Transport (SST) turbulence model was used to simulate the turbulence inside the plasma generator as well as in the plasma jet. For an accurate description of the plasma-particle interaction in plasma spraying, the influences of the plasma on the particles and vice versa were considered in the plasma jet model in a two-way coupled manner [BÖ17]. Furthermore, a validation of the plasma generator and the plasma jet models was conducted by comparing numerical results to experimental data [BÖS+16, BÖS+17]. A detailed description of the numerical modeling used for data generation can be found in [Öte16, BÖ16].

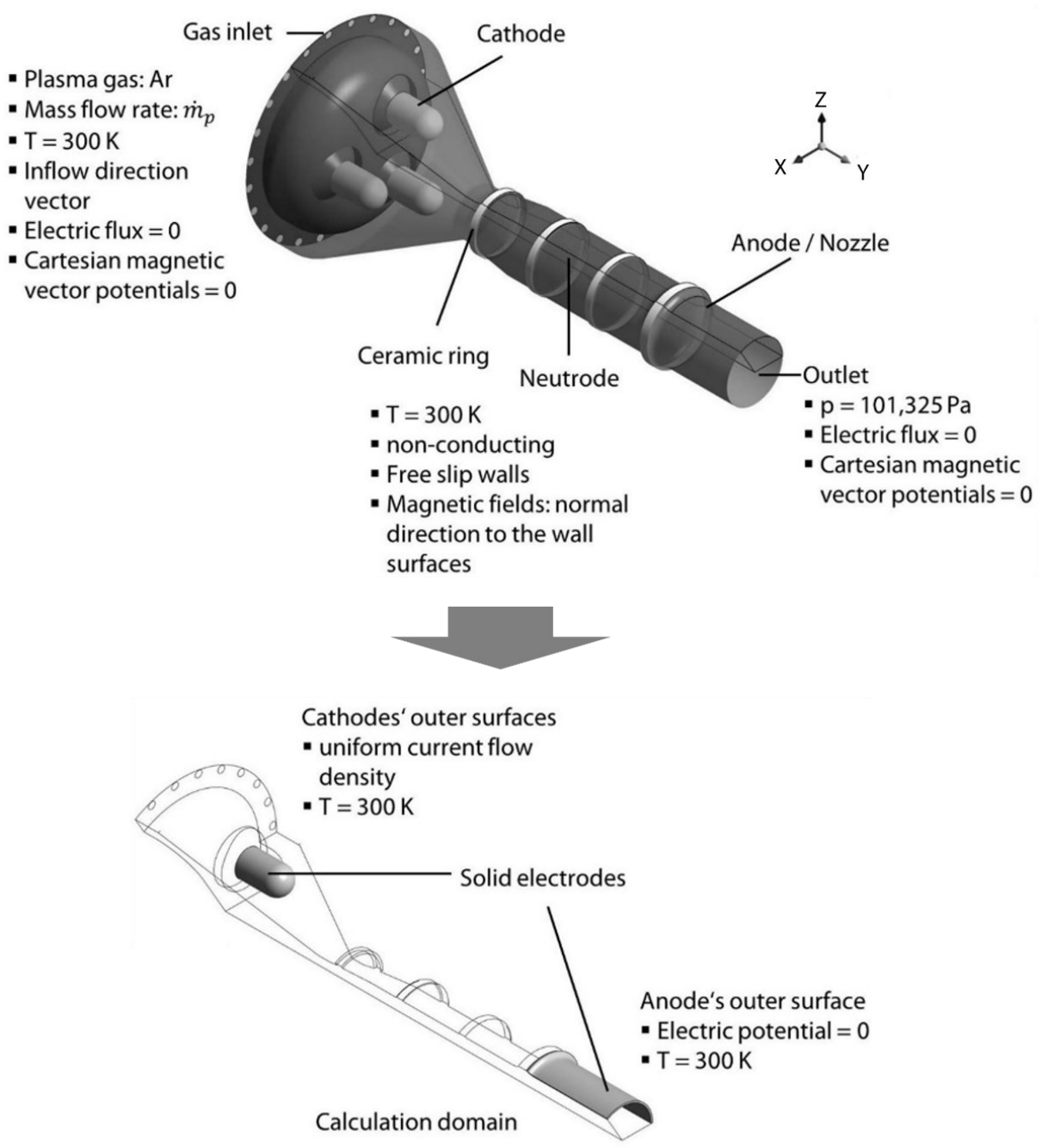

Figure 53: Computational domain and boundary conditions of the plasma generator model [BÖS+17]

Figure 54 shows the simulated particle trajectories and their temperatures inside the plasma jet exemplary for one simulation. For each simulation, a virtual clipping plane was defined to export the particle properties at specific stand-off distances. The particle properties include the in-flight particle coordinates on the clipping plane, the particle velocities and temperatures. The

simulation models were created in ANSYS CFX version 20.2 (ANSYS, Inc., Canonsburg, USA). For each simulation, the calculated number of particle trajectories was set to 2,000. Alumina was used as the feedstock material for the simulations. Further details regarding the procedure of preparing the simulation data are described in the next section.

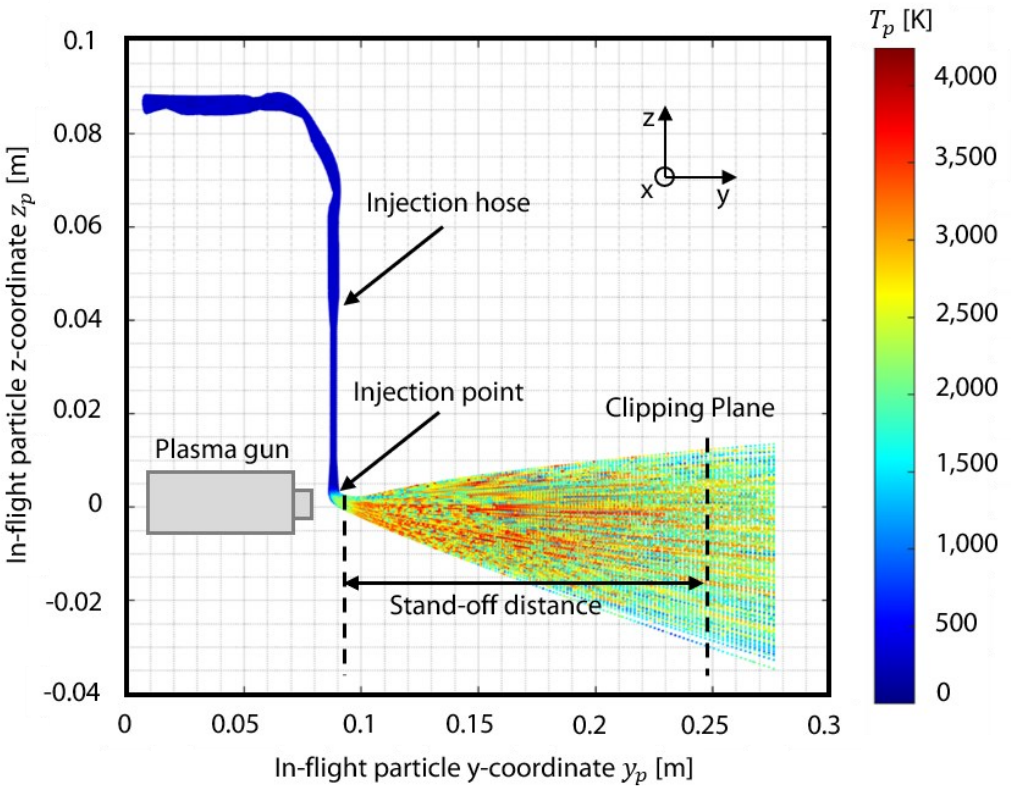

Figure 54: Exemplary simulated particle trajectories and their temperatures in plasma jet [BWH+21]

6.2 Data Preparation

Simulations often involve larger number of variables compared to physical experiments. It is necessary to find a set of input parameters, namely the design matrix, so that potentially the best-fitting predictive model can be constructed on the resulting data sets formed by the design matrix [FLS05]. Furthermore, this allows understanding the cause-and-effect relationships in the system by changing the designed input variables and observing the resulting changes in the system output [Mon13]. Therefore, two different DoE methods, CCD and LHS, were employed to cover a set of representative input process parameters for the simulations. The parameter setup for the CCD and LHS methods are given in Table 7.

Table 7: Parameter setup for the DoE methods

Parameter [unit]	Interval
Primary gas flow [SLPM]	40 - 60
Electric current [A]	400 - 540
Carrier gas flow [SLPM]	3.5 - 7
Powder feed rate [g/min]	10 - 30
Particle size distribution [µm]	-35 +15; -55 +35; -75 +55
Stand-off distance [mm]	100 - 180

Totally six different process parameters were considered for the DoE approach: primary gas flow (Argon), electric current, carrier gas flow, powder feed rate, particle size distribution at the injection point and stand-off distance. The particle sizes were divided into three different fractions to cover the broad spectrum of the possible particle size distributions in plasma spraying. As part of an automated data preparation pipeline, the DoE was built in the MATLAB environment and was linked with the CFX Command Language (CCL) to implement the DoE parameters in the simulation models. This structure was then connected to the batch job scheduler using shell scripts on the RWTH compute cluster. Therefore, several sets of process parameters with corresponding particle properties were acquired from the CFD simulations and were prepared as training data for the SVM models automatically. Overall, 45 simulations were carried out for the CCD data sets and another 45 simulations for the LHS data sets. In the following, both DoE methods and the structure of the data for the simulations are briefly described.

6.2.1 Central Composite Design (CCD)

CCD is based on a two-level full or fractional factorial design with 2k additional points between the axes, where k is the number of independent variables. It has also a set of repeated points at the centroid labeled with N_0. Figure 55 shows a geometric view of a CCD for a two-factor full factorial design. CCD is used widely in constructing second-order response surface models [MMA09].

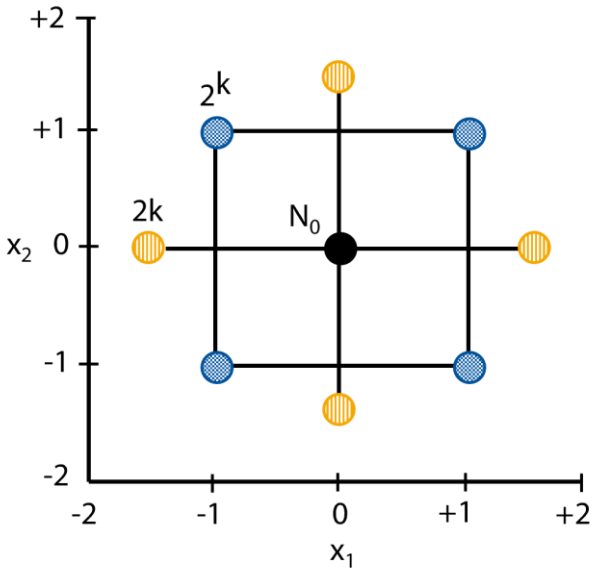

Figure 55: Geometric view of central composite design for k = 2 factors [BWH+21]

Random errors are inevitable in physical experiments and the output may be different even with the same experimental settings. In the contrary, the computer experiments are deterministic and multiple trials result in identical outputs. Hence, carrying out several runs at the centroid is only meaningful in physical experiments [FLS05]. For data preparation, the number of computational experiments was set to 45, which corresponds to a CCD with 6-factor fractional design ($2^{k-1} + 2k + N_0$).

6.2.2 Latin Hypercube Sampling (LHS)

LHS is one of the most popular space-filling designs that aims at reducing the variance of sample mean [SZ16]. It is a stratified sampling technique that divides the multidimensional experimental domain into N strata of equal marginal probability, where N is the number of sample points. Each stratum contains only one sample point along each space dimension, and then the technique samples once from each stratum. [FLS05].

The so-called *maximin distance* criteria can be applied as an optimality factor for construction of LHS to further decrease the variance of the sample mean. A maximin LHS maximizes the minimum distance between each pair of experimental points within the experimental domain, see Figure 56.

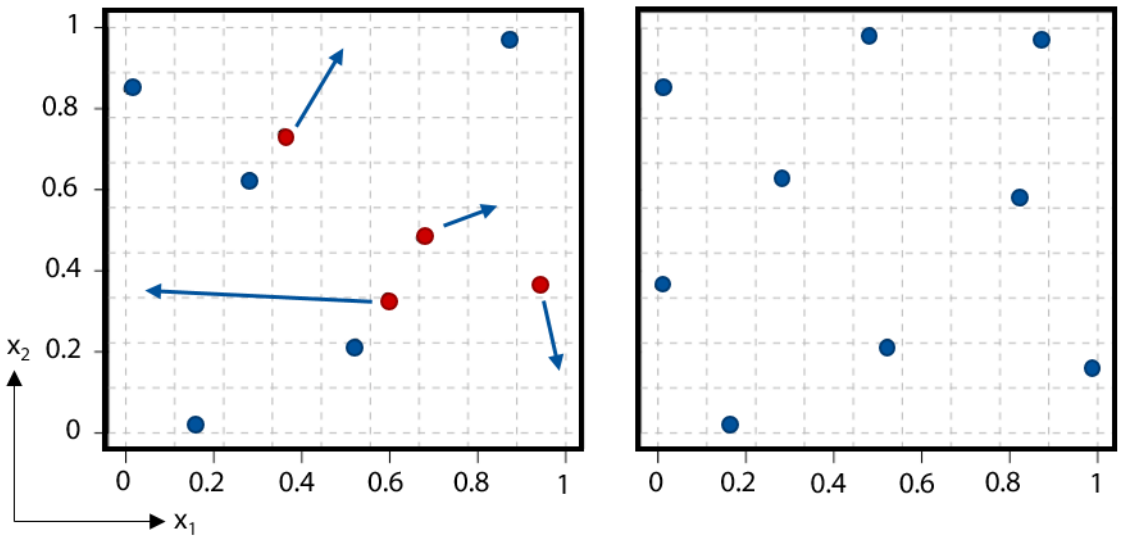

Figure 56: Transformation of a 2D LHS (left) to a maximin LHS (right) [BWH+21]

This optimality criterion ensures that the experimental points are spread out uniformly through the domain and therefore, no point lies too far away from a design point [JH08]. This results in an enhancement of the prediction accuracy of the constructed model. LHS is a very suitable and powerful DoE technique for computer experimentation, which can serve various numbers of runs and input variables. To ensure the comparability of the results, the same number of runs as the CCD method was used for the LHS method.

6.2.3 Structure of Training Data

As mentioned earlier, for each of the DoE methods introduced in the above sections, 45 simulations were performed respectively with different input process parameters, see Table 7. For instance, the simulation data sets gathered from the LHS method for the parameters primary gas flow, electric current, carrier gas flow, powder feed rate, particle size distribution and stand-off distance, respectively, are:

1. 40.36 SLPM, 461.6 A, 6.39 SLPM, 28.8 g/min, -35 +15 µm, 126 mm
2. 40.36 SLPM, 532.9 A, 5.72 SLPM, 15.6 g/min, -35 +15 µm, 153 mm
3. 41.37 SLPM, 473.8 A, 4.04 SLPM, 12.0 g/min, -35 +15 µm, 169 mm

⋮

45. 59.87 SLPM, 470.3 A, 4.04 SLPM, 18.0 g/min, -75 +55 µm, 144 mm

The CCD simulation data were also structured into 45 simulations. The complete list of process parameters from both LHS and CCD methods are presented in the Appendix (page 124-127). The outputs of the simulations are the in-flight particle properties of the 2,000 simulated particle trajectories per simulation respectively. However, regarding the different process parameters within each simulation, not all of the 2,000 simulated particle trajectories can reach the specified stand-off distance. Hence, the exact number of output data per simulation for the 45 CCD or LHS simulations is not the same and can vary between 1,500 and 2,000 particle trajectories. The inputs and outputs of each simulation were provided with indices to be able to assign the particles of each simulation for the ML models.

The DoE methods provide the representative simulation data sets for training the ML models. The inputs of the prediction models are the process parameters listed in Table 7. The outputs are the particle properties including the in-flight particle temperatures T_p [K] and velocities v_p [m/s] as well as the in-flight particle x-coordinates x_p [m] and z-coordinates z_p [m] at specific stand-off distances on the virtual substrate (clipping plane).

The results from the LHS and CCD methods were each partitioned into one training data set and one test data set. From each of the respective 45 simulations, 75 % of the data were used as training data and the remaining 25 % as test data. As described earlier, the number of particles per simulation may differ and thus, the overall number of particles in the training and test data sets for the CCD and LHS methods is different. The training data for CCD contain 64,858 particles and the test data include 21,612 particles, while these numbers amount to 64,728 and 21,566 for the LHS respectively. Even the models are trained and tested with the whole training and test data out of the 45 simulations respectively, the allocation of the particles to each simulation is still known by use of the indices as data labels. This is utilized later in the evaluation of the results.

The simulation data sets for each DoE method consist of approximately 90,000 particles, resulting in a total simulation data sets of 180,000 particles. It is worth mentioning that generating this much data through experiments is extremely resource-intensive, both in terms of time and energy consumption. In addition, the experiments, involving the utilization of gas, powder, and energy, lead to a substantial carbon footprint. This underscores the importance of

using computational methods, particularly Digital Shadows, as a more sustainable alternative to classical process development approaches.

6.3 SVM Setup

SVM is a supervised-learning algorithm that uses structural risk minimization, and therefore exhibits great generalization features. SVM employs a symmetrical loss function, which equally penalizes high and low errors. An important property of the SVM regression is that its computational complexity does not depend on the dimension of the input space. SVM automatically determines the model complexity by choosing the number of support vectors, unlike ANN, which controls model complexity by restricting the feature set. Furthermore, since SVM solves the convex optimization problem analytically, it always returns the same optimal hyperplane parameter [AK15]. Please refer to Chapter 2 for an in-depth description of SVM.

The implementation of the SVM regression algorithm was carried out using the Statistics and Machine Learning Toolbox of MATLAB. In order to make the inputs and targets insensitive to the scales and magnitudes on which they are processed, a preprocessing step has been carried out to standardize the training data sets. The standardization was done based on the so-called z-score method, in which the corresponding standardized data have a mean value of zero and a standard deviation of one. Hence, the shape of the original data set is retained.

Four single-output SVM models, corresponding to the four outputs, for each of the two DoE methods, LHS and CCD, were developed. For training the regression models, Gaussian kernels $k(x_i, x_j)$ based on Eq. 17 were employed, where γ represents the kernel scale.

$$k(x_i, x_j) = \exp\left(-\frac{\|x_i - x_j\|^2}{2\gamma^2}\right) \qquad \text{Eq. 17}$$

The training of the SVM models was conducted with different kernel scales, as given in Table 8, to choose the best prediction accuracy. The term P in Table 8 denotes the number of predictors, which equals to $P = 6$ in this case. Furthermore, a 10-fold cross-validation was used to analyze the level of generalization and prevent possible overfitting.

Table 8: Kernel scales of different Gaussian kernels applied for training the SVM models

Kernel type	Kernel scale
Fine Gaussian	$\gamma = \sqrt{\frac{P}{32}}$
Medium Gaussian	$\gamma = \sqrt{\frac{P}{2}}$
Coarse Gaussian	$\gamma = \sqrt{8P}$

6.4 Prediction of Particle Properties

In this section, the results of the ML models based on simulation models, namely metamodels, are presented and discussed. For each data set produced by different experimental designs, separate prediction models were trained. Then, the target values on the virtual substrate, which are the particle temperatures, velocities and positions (x and z-coordinates) were tested by the corresponding predefined test data sets.

Due to the data labeling, the assignment of the particles to their particular simulation is known. Hence, for a qualitative comparison of ML and simulation results, the average particle behavior per simulation can be investigated. Exemplarily, the mean particle temperatures $\bar{T}_{p,i}$ per simulation $i \in [1,45]$ are computed by

$$\bar{T}_{p,i} = \frac{1}{n_i} \sum_{j=1}^{n_i} T_{p,i,j} \qquad \text{Eq. 18}$$

- $\bar{T}_{p,i}$ Mean particle temperature of simulation i
- n_i Number of test particles of simulation i
- $T_{p,i,j}$ Temperature of particle j of simulation i

The mean value over all 45 simulations is then computed by

$$\bar{T}_p = \frac{1}{45}\sum_{i=1}^{45} \bar{T}_{p,i} \qquad \text{Eq. 19}$$

and denoted by "*grandmean*" in the following. The means and grandmeans of the particle velocities and positions are computed analogously.

For a quantitative evaluation of the ML results, two statistical measures are considered. To evaluate the prediction accuracy of the individual particle properties, the mean absolute percentage error (MAPE) is calculated. Given N data points, the MAPE is defined by

$$MAPE = \frac{1}{N}\sum_{i=1}^{N} \left|\frac{t_i - p_i}{t_i}\right| \qquad \text{Eq. 20}$$

- $MAPE$ Mean Absolute Percentage Error
- N Number of data points
- t_i Target values
- p_i Prediction values

Furthermore, the R-squared value, for N data points, target values t_i with mean $\bar{t}$ and predictions p_i defined by

$$R_{sq} = 1 - \frac{\sum_{i=1}^{N}(t_i - p_i)^2}{\sum_{i=1}^{N}(t_i - \bar{t})^2} \qquad \text{Eq. 21}$$

is calculated to evaluate the prediction accuracy of the average particle properties.

Figure 57-a shows the results of the mean particle temperatures $\bar{T}_{p,i}$ per simulation $i \in [1,45]$, see Eq. 18, from the CCD data sets. The mean values predicted by the SVM model shown in red are denoted with "Mean SVM", while the corresponding target values from the simulation model displayed in blue are labeled with "Mean Sim.". The grandmeans according to Eq. 19 are also plotted in Figure 57. In the same way, the results of the mean predicted particle temperatures from the LHS data sets are depicted in Figure 57-b.

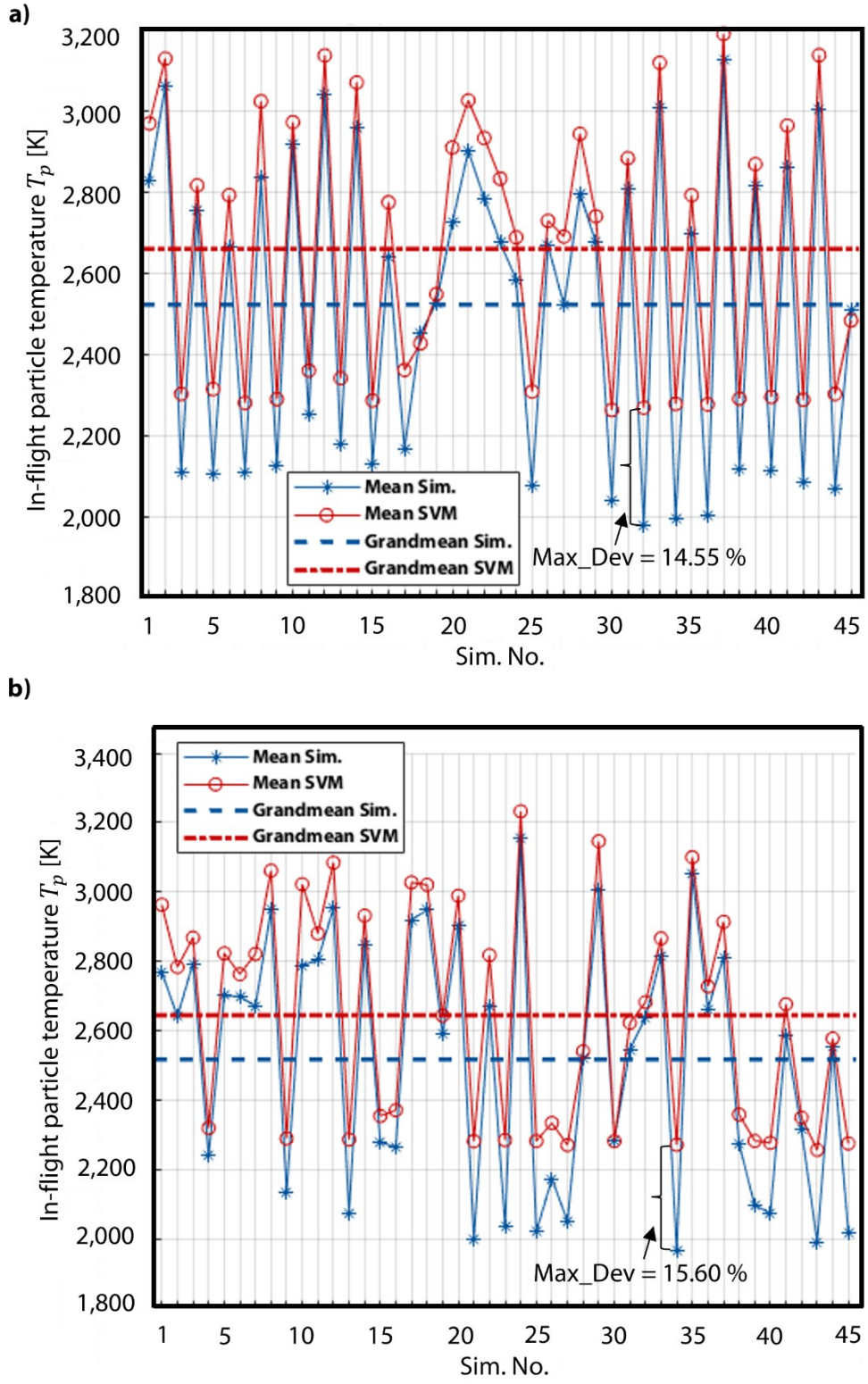

Figure 57: Results of the SVM model for mean particle temperatures per simulation from a) CCD and b) LHS data sets according to [BWH+21]

The results demonstrate that the developed metamodels have high accuracy in predicting the mean in-flight particle temperatures of the 45 simulations out of the input process parameters. Furthermore, it is observed that the developed SVM models have slightly better performance in predicting the particle properties with higher temperatures than the lower ones. In other words, in cases where the particles penetrated deeply into the plasma jet, thus resulting in higher temperatures and velocities, the models could find better relationships between the input process parameters and the particle properties. This has been observed for both CCD and LHS data sets in the SVM metamodels. The maximum deviations between the targets and the predicted values for particle temperatures in case of the CCD and LHS data sets are calculated to be $Max\_Dev_{T,CCD} = 14.55$ % and $Max\_Dev_{T,LHS} = 15.60$ %.

Figure 58-a shows the findings of the mean predicted particle velocities from the CCD data sets, while Figure 58-b shows the results from the LHS data sets. Analogously, the predicted values are shown in red and their corresponding target values are displayed in blue. The figures show that the mean in-flight particle velocities could be accurately replicated with the SVM models. When comparing the lower and upper ranges of particle velocities, it is also evident from these figures that the metamodels exhibit a slightly better performance in predicting particle velocities within the upper range. In comparison to particle temperatures, the model grandmeans for particle velocities show a better agreement with the grandmeans of the simulation. The maximum deviations between the targets and the predicted values for particle velocities in case of the CCD and LHS data sets are calculated to be $Max\_Dev_{v,CCD} = 10.10$ % and $Max\_Dev_{v,LHS} = 9.23$ %.

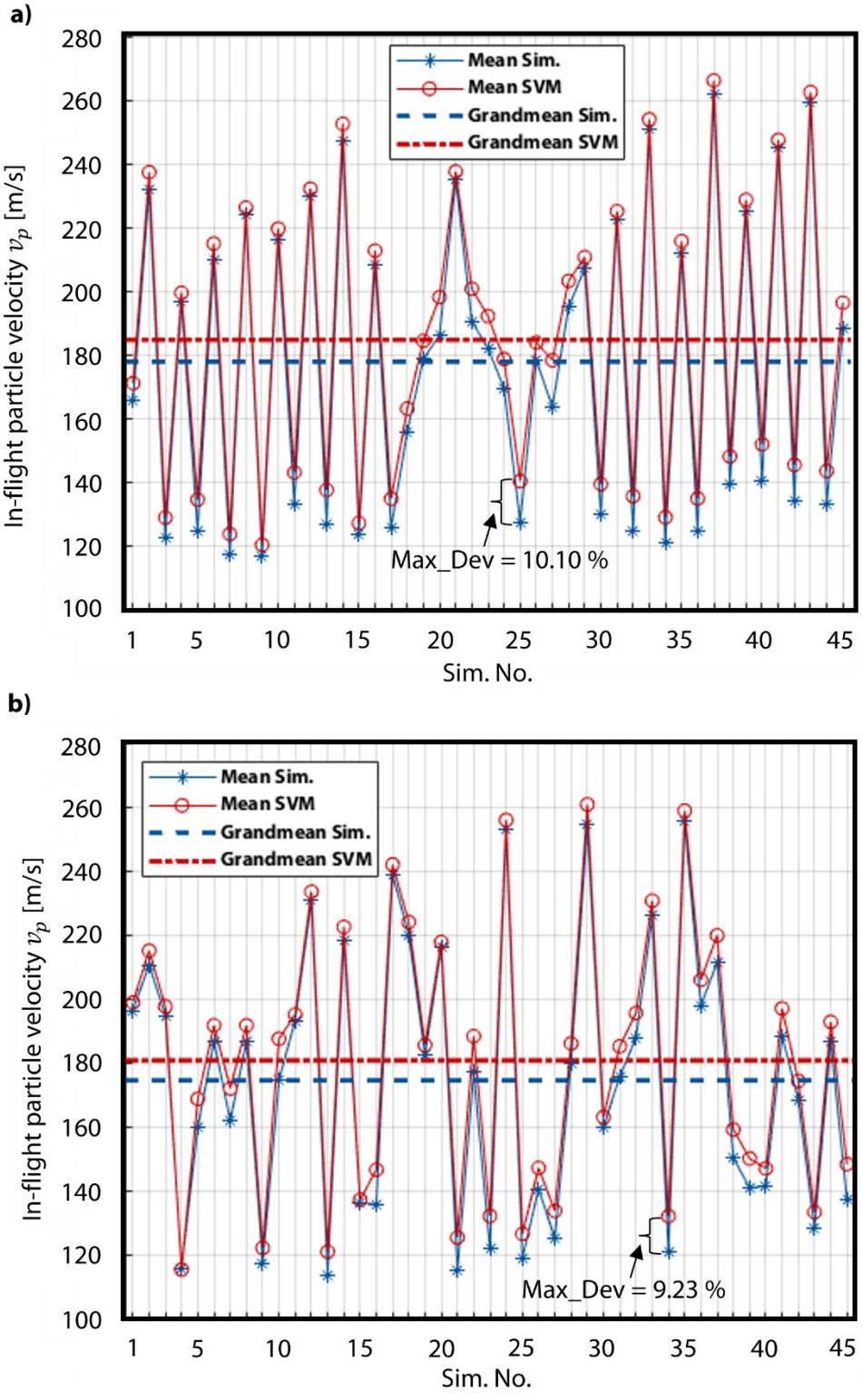

Figure 58: Results of the SVM model for mean particle velocities per simulation from the a) CCD and b) LHS data sets according to [BWH+21]

The predicted and target values of the individual particle velocities exemplarily from the LHS data sets are shown in Figure 59. For a clear presentation, only 250 data points from the total 45 simulations are randomly selected. It is evident that the metamodel can replicate the trend of the particle velocities in the plasma jet. The prediction of the mean particle velocities and temperatures is more accurate than the prediction of the individual particle properties. As mentioned earlier, this can be explained with the stochastic nature of the plasma spraying process and the turbulence of the plasma flow. Therefore, predicting the behavior of each single particle is very difficult because it depends on many factors that influence each other. In addition, the individual particles substantially collide with each other and with the inner wall of the narrow particle injector, resulting in a random initial distribution of the particles. These collisions cause the final particle properties to be very sensitive to the initial position, i.e., small differences in the initial position can have a large influence on the final particle positions, velocities, and temperatures on the substrate. Hence, it is possible that two particles of nearly the same size and for the same process parameters exhibit different temperatures or velocities. As a consequence, prediction of the average particle behavior is more precise and reliable.

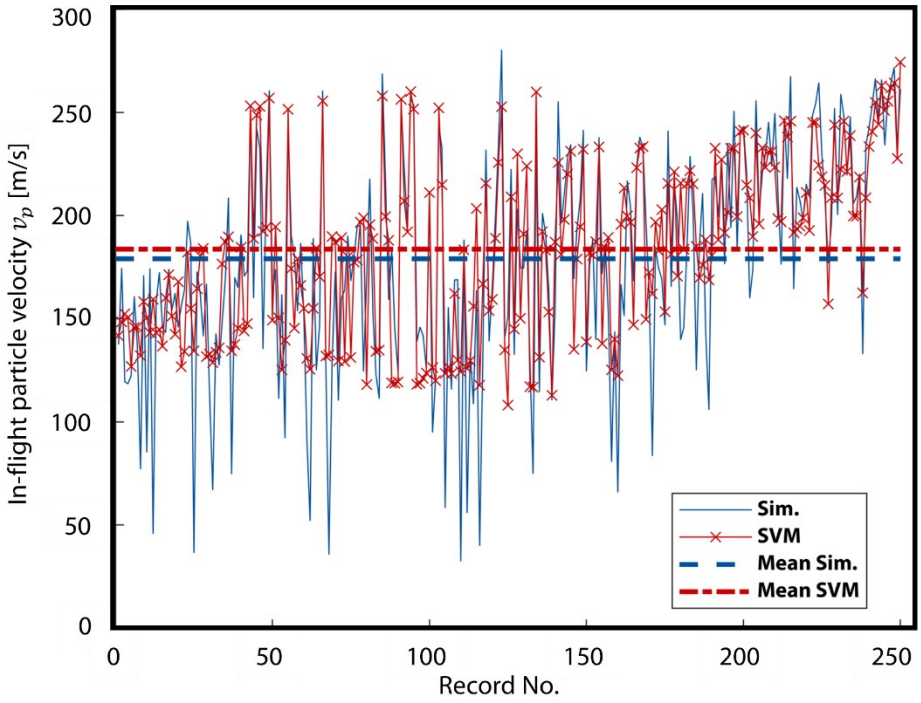

Figure 59: Exemplary trend of the predicted particle velocities by SVM model from LHS data sets [BWH+21]

Table 9 presents the statistical values MAPE (Eq. 20) and R-squared (Eq. 21) for the prediction of single and average particle properties by the SVM models from different DoE methods. The performance of the SVM models, in terms of the prediction accuracy of average particle properties, remains consistent for both CCD and LHS data sets. However, when it comes to prediction of single particle properties, the LHS experimental design shows a slight improvement in prediction accuracy compared to CCD. This confirms the suitability of the LHS for computational experiments. Furthermore, it should be emphasized again that due to the stochastic nature of the plasma spraying process, the prediction of single particle properties cannot be guaranteed using the ML methods at hand.

Table 9: Statistical values for prediction of single and average particle properties by SVM models from different DoE methods [BWH+21]

Statistic parameter	MAPE		R-squared	
Property	Single particle temperature	Single particle velocity	Mean particle temperature	Mean particle velocity
CCD	19.78 %	22.75 %	0.82	0.97
LHS	18.49 %	21.11 %	0.82	0.97

Figure 60 shows the distribution of the predicted particle coordinates by the SVM models from LHS data sets exemplarily for one simulation. For this sample simulation, the process parameters of primary gas flow, electric current, carrier gas flow, powder feed rate, particle size distribution and stand-off distance are respectively: 48.43 SLPM, 413.40 A, 4.71 SLPM, 18.60 g/min, -35 +15 µm and 121 mm. It is clear that the predictions of the single particle coordinates are much less accurate than the particle velocities and temperatures. As previously mentioned, this is due to the fact that the behavior of single particles is to some extent random in a plasma spraying process, while the essence of ML is to learn and predict regular data. In contrast, the SVM models predict the mean particle coordinates per simulation more accurately with R-squared values of 0.86 and 0.88 for x and z-coordinates, respectively. The accurate prediction of the mean particle coordinates can be used as a tool to find the position of the maximum particle intensity in the free jet. This information can, for instance, aid in adjusting injection settings or positioning a particle diagnostic device accordingly [BWK+20].

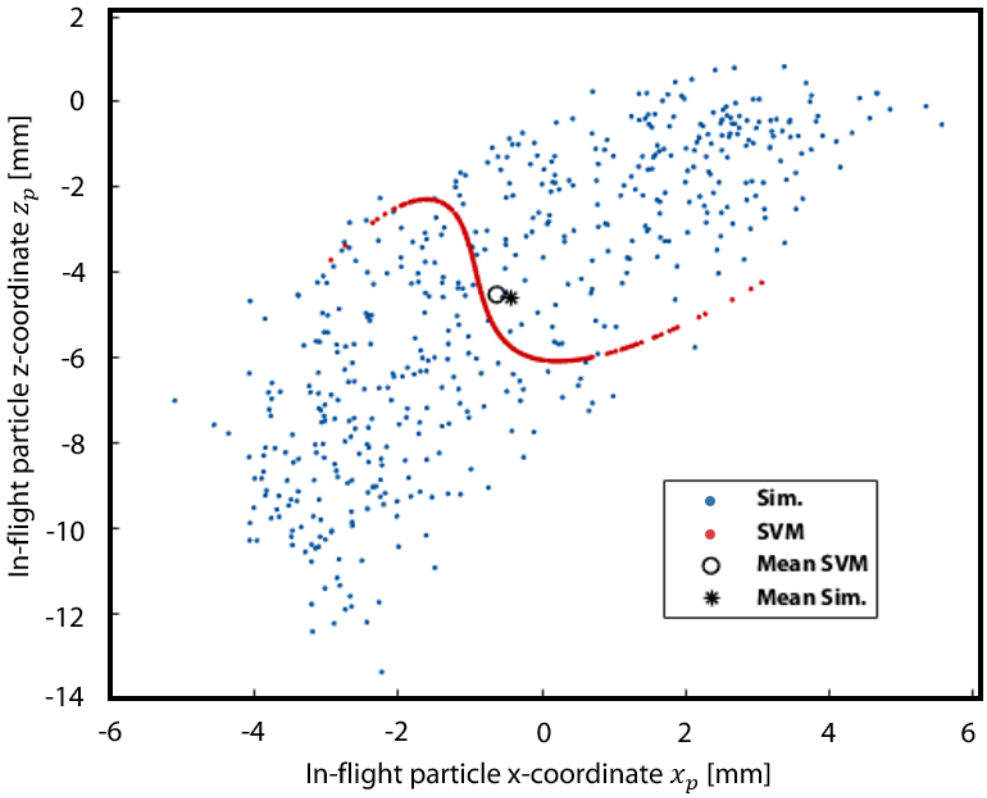

Figure 60: Exemplary distribution of the predicted particle coordinates by SVM models from LHS data sets for one simulation [BWH+21]

The average prediction time of the SVM metamodels for the predefined test data sets was calculated to be about 4.2 s, which is dramatically faster than one CFD simulation of the plasma jet with an average calculation time of 3 hours. Therefore, by using the ML metamodels, the computationally intensive CFD simulations of the plasma jet can be sidestepped for average values of the particle properties.

6.5 Conclusion

The aim of this chapter was to take the primary steps towards creating a Digital Shadow for the plasma spraying process to predict the in-flight particle properties based on input process parameters. The data sets for training the ML models were acquired from a CFD model of the plasma jet. Contrarily to experiments, simulations allow the efficient generation of wide-ranged process data, which not only improves the model's prediction accuracy, but also speeds up the process development. CCD and LHS experimental designs were employed to cover a set of representative process parameters by reducing the number of tests, while selecting the most

valuable sample data. The developed metamodels with SVM are able to replicate the average particle properties with high accuracy, while reducing the computational cost dramatically. The results showed that the average particle properties could be predicted by the metamodels much more accurately than the behavior of single particles. This phenomenon is expected, since the plasma spraying is a stochastic process that involves many influencing factors. Thus, the behavior of single particles is much more random in comparison to average particle behavior. The results of the metamodels from the LHS data sets showed a minor enhancement in terms of the prediction accuracy, which confirmed the suitability of space-filling designs for computational experiments. In the following chapter, the SVM models are integrated in an expert system for prediction of DE in plasma spraying.

7 Expert System for Prediction of Deposition Efficiency

High deposition efficiency (DE) has always been one of the main aims in the development of plasma spraying process in order to create cost-effective coatings in industrial production. DE is one of the key performance indicators for the productivity and consequential sustainability of the APS process. Increasing DE is a difficult task in the process development of plasma spraying due to the nonlinear and complicated interdependencies of the contributing elements. Hence, this chapter is dedicated to develop an expert system to predict DE in plasma spraying. In the following, the architecture of the expert system is described in detail. After description of the system architecture and its training approaches, a test case is considered to present the results of the developed expert system for prediction of DE. The results of this chapter have been already published in [BHD22].

7.1 Architecture of Expert System

The overall architecture of the expert system is depicted in Figure 61. This expert system consists of two blocks: Block A) SVM-models from Chapter 6 are used to predict the in-flight particle properties from different process parameters based on simulation data sets. Block B) an ANFIS model is developed to predict DE from the in-flight particle properties based on experimental data sets of LDE from Chapter 5. The setups of the SVM and ANFIS models are described in the following subsections.

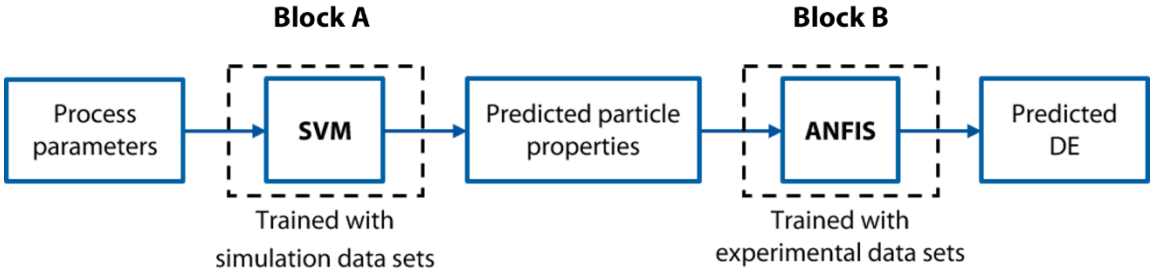

Figure 61: Architecture of the expert system for prediction of deposition efficiency [BHD22]

7.2 Block A: SVM

As discussed in Chapter 6, the training setup of the SVM models is illustrated in Figure 62. In a first step, former CFD models of a multi-arc APS process, developed at the IOT at the RWTH Aachen University, are used to generate the training data for the SVM models. In Figure 62, the

use of data from the already developed models is referred to as data recycling. The benefit of using simulation data is that a wide range of process parameters can be covered, while providing that much experimental data is hardly possible. In the next step, DoE is implemented to cover a set of representative input process parameters for the SVM models. As part of an automated data preparation pipeline, several sets of process parameters with the corresponding particle properties are acquired from the CFD simulations and prepared as training and test data for the SVM models.

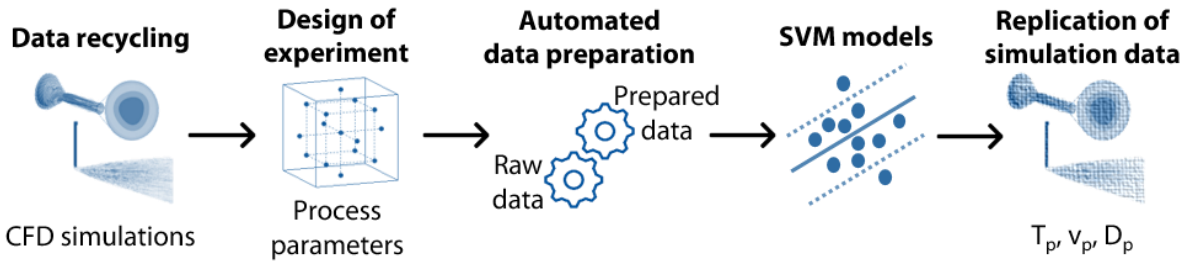

Figure 62: Architecture of Block A of the expert system: Training setup of the SVM models to predict in-flight particle properties [BHD22]

The training inputs of the prediction models are the process parameters listed in Table 7 in the previous chapter. These include primary gas flow (Argon), electric current, carrier gas flow, powder feed rate, particle size distribution at the injection point and stand-off distance. The outputs of the SVM models are the particle properties including the in-flight particle temperatures T_p [K], velocities v_p [m/s] and sizes D_p [µm] at specific stand-off distances. These particle properties are used then as inputs for the next block of the expert system to predict LDE. Please note that the prediction of particle size is considered here as an additional output of the SVM models compared to the previous chapter. This is because the LDE data sets obtained in Chapter 5 were correlated with these three particle properties, in particular temperature, velocity and size. The results of the SVM models for different process parameters were given in Chapter 6.

7.3 Block B: Neuro-Fuzzy System

The training setup of the Block B of the expert system is shown in Figure 63. The training data consist of experimental data from Chapter 5. These data include the in-flight particle sizes and velocities measured by the HiWatch as well as the in-flight particle temperatures measured by

the DPV-200. Besides of these particle properties, the corresponding data sets of the spatially resolved deposition efficiencies on the substrate, namely local deposition efficiency (LDE), are used to train the neuro-fuzzy system. As discussed in Chapter 5, LDE was calculated based on spatial distribution of the particle mass flow rate in the free jet and the mass of the deposited feedstock material locally on the substrate. The motivation for using spatially resolved deposition efficiency is that a relatively broad database of particle properties and LDE can be obtained, while providing that much data for the global DE together with the corresponding in-flight particle diagnostic measurements is hardly practical.

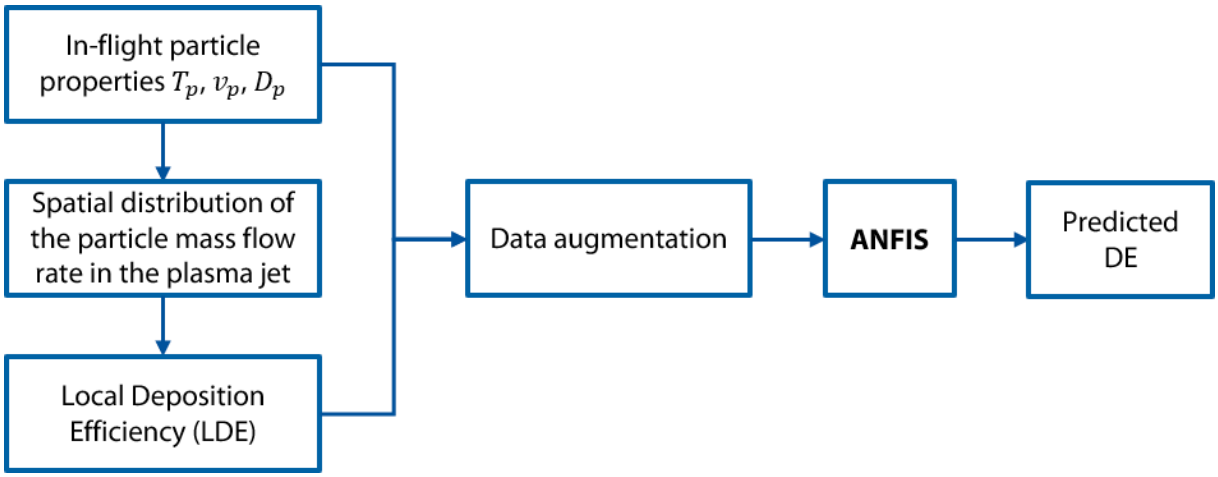

Figure 63: Architecture of Block B of the expert system: Training setup of the ANFIS model to predict DE according to [BHD22]

Please note that the SVM model developed in Chapter 5 served to investigate the nonlinear interdependencies among the in-flight particle properties and LDE values. In this chapter, it is proposed to replace the SVM model illustrated in Figure 52 with a neuro-fuzzy system. We have already a collection of input/output data of particle properties and LDE from a specific set of process parameters, see Table 6 in Chapter 5. The ANFIS technique is chosen due to its ability to handle highly nonlinear mappings by its adaptive parameters that customize the membership functions. This makes ANFIS a powerful tool for generalizing the characteristics of a data collection to similar scenarios, in our case from one set of process parameters to similar sets of process parameters in APS. Hence, in this block of the expert system, an ANFIS model is proposed to leverage its adaptive interpretation capabilities to generalize our data collection and to finally predict DE from particle properties for different sets of process parameters.

As shown in Figure 63, before developing the ANFIS model to predict DE, the training data were augmented using the k-nearest neighbor (k-NN) algorithm to enhance the model accuracy in terms of automatic generation of the rule base and membership functions. This technique uses k closest training data to a particular sample point in our experimental database to increase the diversity and the amount of data before training the ANFIS model. In the following sections, first the implemented data augmentation is described in detail. Subsequently, the setup of the ANFIS model and the results of LDE prediction are presented. Finally, the results of the developed expert system for predicting global DE are outlined as part of a test case.

7.4 Data Augmentation

The amount of training data needed for an ANFIS model may be less than what is required for a classical neural network. However, the size of the training data should still be sufficient to account for all possible cases, depending on the number of premise and consequent parameters [ASA+12]. As Jang stated in [Jan93], the quantity and quality of data play a crucial role in the learning processes used to establish the membership functions (MFs). In this work, to enhance the automatic tuning of MFs, the 100 experimental data sets for particle properties and LDE from Chapter 5 were increased by a factor of 1.5 before training the ANFIS model. This led to a total of 150 data sets used to train the ANFIS model. The k-nearest neighbor (k-NN) method is utilized for data augmentation, where k is set to 5. This method finds the k closest, most similar, neighbors to the sample point being investigated, by minimizing a distance function. For this purpose, the Euclidean distance [Pet09] is considered based on Eq. 22.

$$E(X_i, Y_s) = \sqrt{(x_{ij} - y_{sj})^2 + (x_{ij} - y_{sj})^2 + \cdots + (x_{IJ} - y_{SJ})^2} \qquad \text{Eq. 22}$$

$$i = 1, 2, \ldots, I\ ,\ s = 1, 2, \ldots, S\ ,\ j = 1, 2, \ldots, J$$

- X Input vector of original data
- Y Input vector to be classified
- I Length of the vector X
- S Length of the vector Y
- J Total number of features

In this work, the features of the input vectors consist of particle temperatures, velocities and sizes, therefore J is equal to 3. To apply the k-NN method, 50 initial data sets of particle properties are first generated randomly within the oriented bounding box (OBB) of the original data, as shown in Figure 64. OBB is the box with the smallest dimension, in our case a volume, circumscribing all the points in the input space [O'R85]. The next step involves identifying the five nearest original data to these initial sample data using Eq. 22.

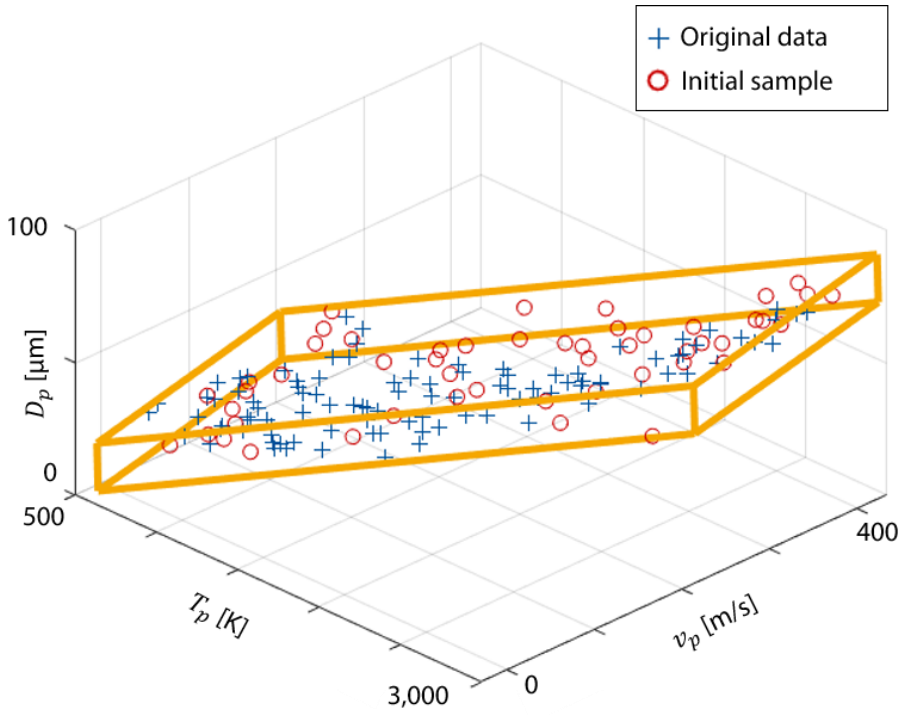

Figure 64: Initial sample data of particle properties in the oriented bounding box of the original data to be used for the k-NN method [BHD22]

The final augmented data are obtained by calculating the average of the nearest neighbors, as demonstrated in Figure 65. In this figure, one exemplary initial point is linked to its nearest neighbors with black dashed lines and to its final resulting k-NN point with a green line. Furthermore, the particle properties in this figure are normalized for the purpose of comparing the distances between the points.

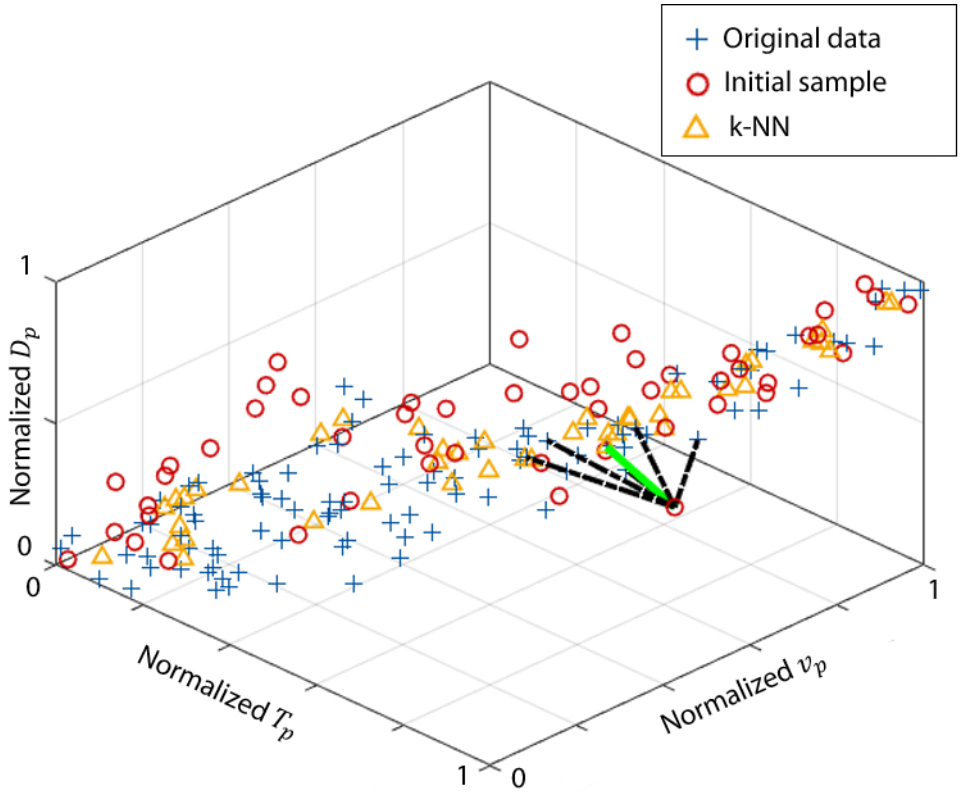

Figure 65: Plot of the particle properties for the original data, initial sample data and the corresponding augmented data by k-NN [BHD22]

Similarly, the LDE of the generated data sets of particle properties are obtained by averaging the LDE of the corresponding nearest neighbors of the original data. Figure 66 displays the entire data sets, comprising both the augmented and original data, as an example in a 2D plot of temperature versus velocity. In this figure, the corresponding LDE values are given in color map. The overall data sets are utilized to develop the ANFIS model.

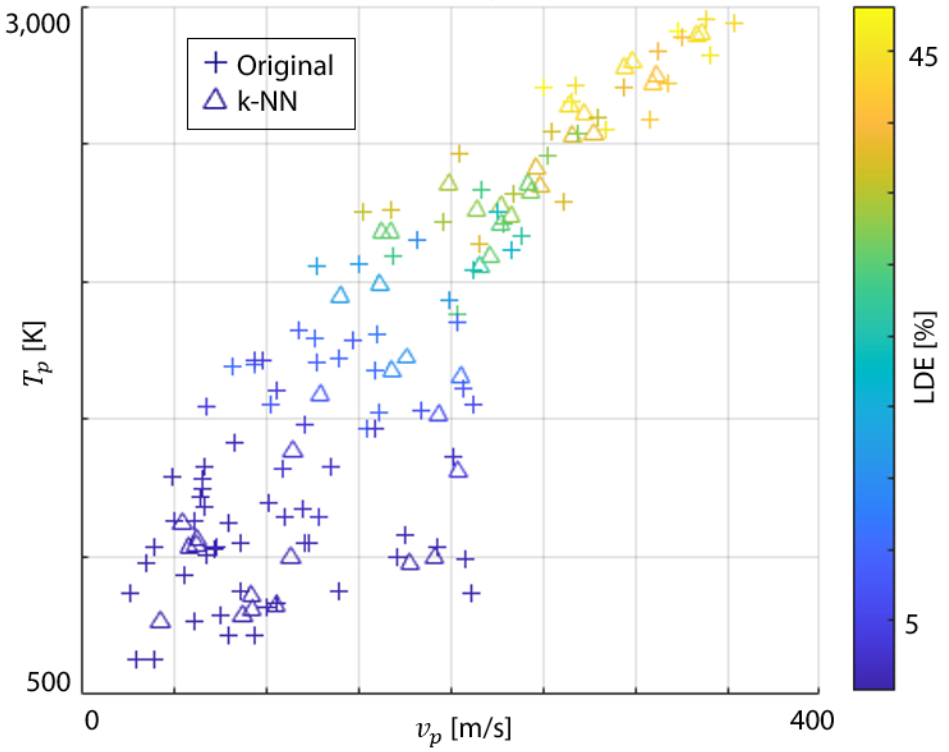

Figure 66: Overall data sets, including the original and augmented data, exemplarily in a 2D plot of temperature versus velocity with the corresponding LDE values [BHD22]

7.5 ANFIS Model

The increasing interest in the field of artificial neural networks injected a new driving force into the architecture of FL systems, arising a novel synergy called *neuro-fuzzy* systems. An adaptive network framework, which unites both neural networks and fuzzy models, forms the foundation of neuro-fuzzy systems [JS95]. Such system employs a learning algorithm developed from or motivated by ANN to establish its parameters, fuzzy sets and fuzzy rules, by processing of data sets. The fuzzy models within the adaptive network framework are known as the Adaptive Neuro-Fuzzy Inference System (ANFIS), which may have several advantages over neural networks. Please refer to Chapter 2 for a comprehensive description of ANFIS.

In this work, the adaptive parameters of the ANFIS model are adjusted using a data-driven hybrid learning algorithm. The hybrid approach combines backpropagation for the parameters linked to the input membership functions or premise parameters, and least squares estimation (LSE) for the parameters associated with the output membership functions or consequent

parameters [Jan93]. The mathematical description of the hybrid learning algorithm is given in the appendix (page 128-129).

Figure 67 displays the block diagram of the optimization algorithm used to optimize the FIS parameters. As illustrated in this figure, the optimization algorithm generates potential FIS parameter sets during training. The fuzzy system is updated with each parameter set and then the input training data are employed for evaluation. The cost for each solution is calculated by the difference between the output of the fuzzy system and the expected output values from the training data.

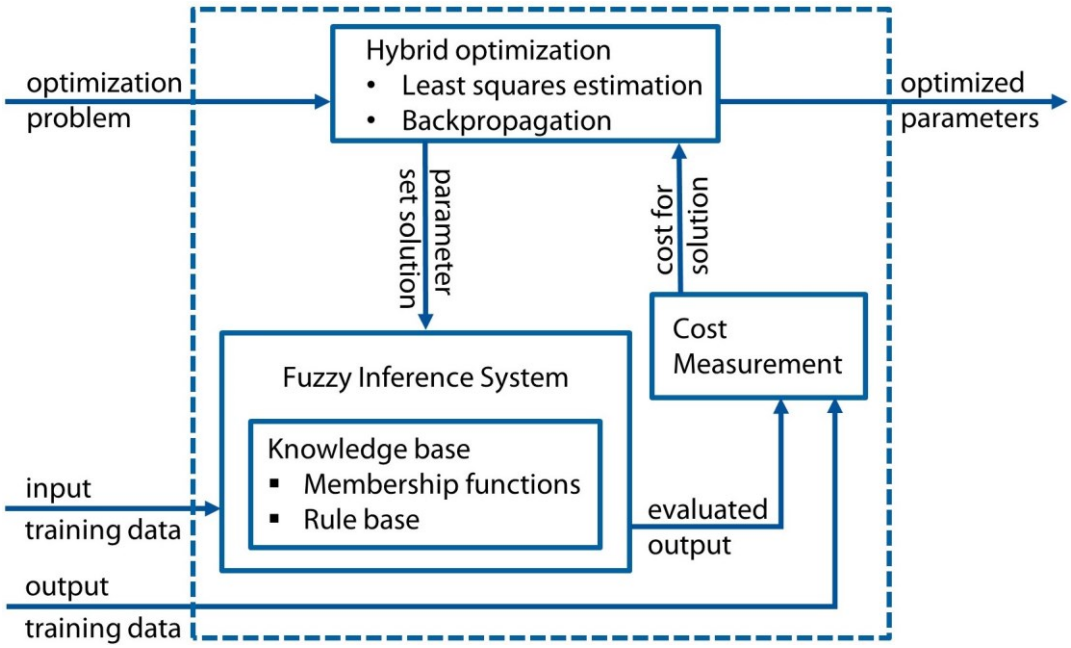

Figure 67: Block diagram of tuning fuzzy inference system [BHD22]

The ANFIS model to predict DE from particle properties is developed in the MATLAB program version R2021b (The MathWorks, Inc., Massachusetts, USA). The 150 total data sets, including augmented and original data, are split into two distinct groups, such that 80 % of the data are used as training data and the remaining 20 % as test data. This division results in 120 data sets for training and 30 data sets for testing. To model the data behavior with the fewest possible rules, the input-output training data are first clustered using Fuzzy c-means (FCM) clustering technique [BEF84]. This method is employed to classify multidimensional data points into a certain number of different clusters. Each data point in FCM belongs to a cluster to some degree

that is specified by a membership grade. FCM begins by estimating initial cluster centers, which are meant to represent the average location of each cluster. In addition, FCM assigns a membership grade to each data point for each cluster. FCM then iteratively updates the cluster centers and the membership grades of each data point to arrive at the optimal cluster locations within the data set. The use of FCM clustering helps to minimize the number of rules in an ANFIS model, as the rules are partitioned based on the fuzzy qualities associated with each of the data clusters.

In this work, FCM clustering method is utilized to classify the training data into four clusters. The FCM information is then used to create a Sugeno-type ANFIS model, where the MFs reflect the fuzzy qualities of each cluster. Figure 68 depicts the block diagram of the developed ANFIS. The Sugeno-type inference system contains four rules corresponding to the four pre-defined clusters. The inputs of the model include particle temperatures, velocities and sizes, while LDE is its single output. Each input is characterized by a Gaussian MF per each fuzzy cluster, leading to a total of four MFs for each input. The output variable, on the other hand, has one linear MF for each fuzzy cluster.

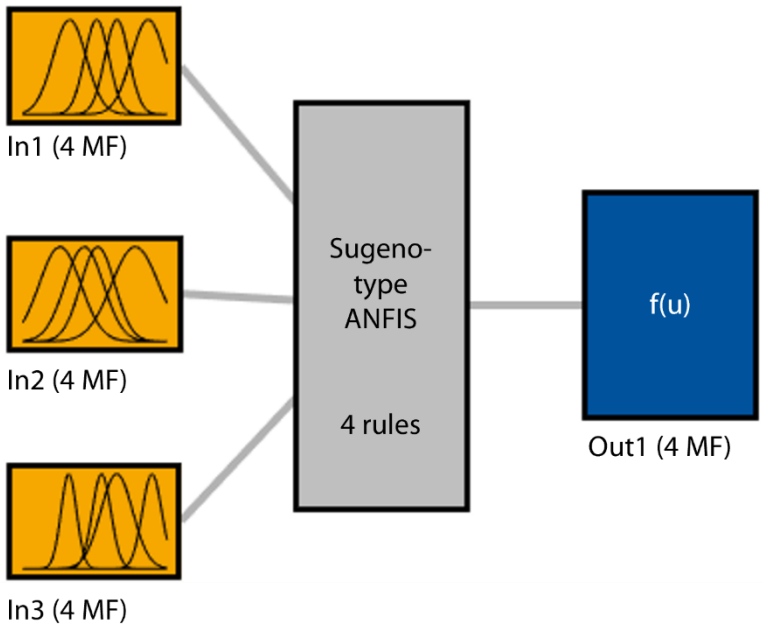

Figure 68: Block diagram of the developed ANFIS [BHD22]

The diagrams in Figure 69 display the membership functions of the inputs. The four Gaussian MFs for each input, corresponding to the fuzzy clusters, are depicted in each diagram. The ranges of the input particle properties can also be seen on the x-axis of the diagrams shown in Figure 69. These ranges represent the typical scope of particle properties in APS.

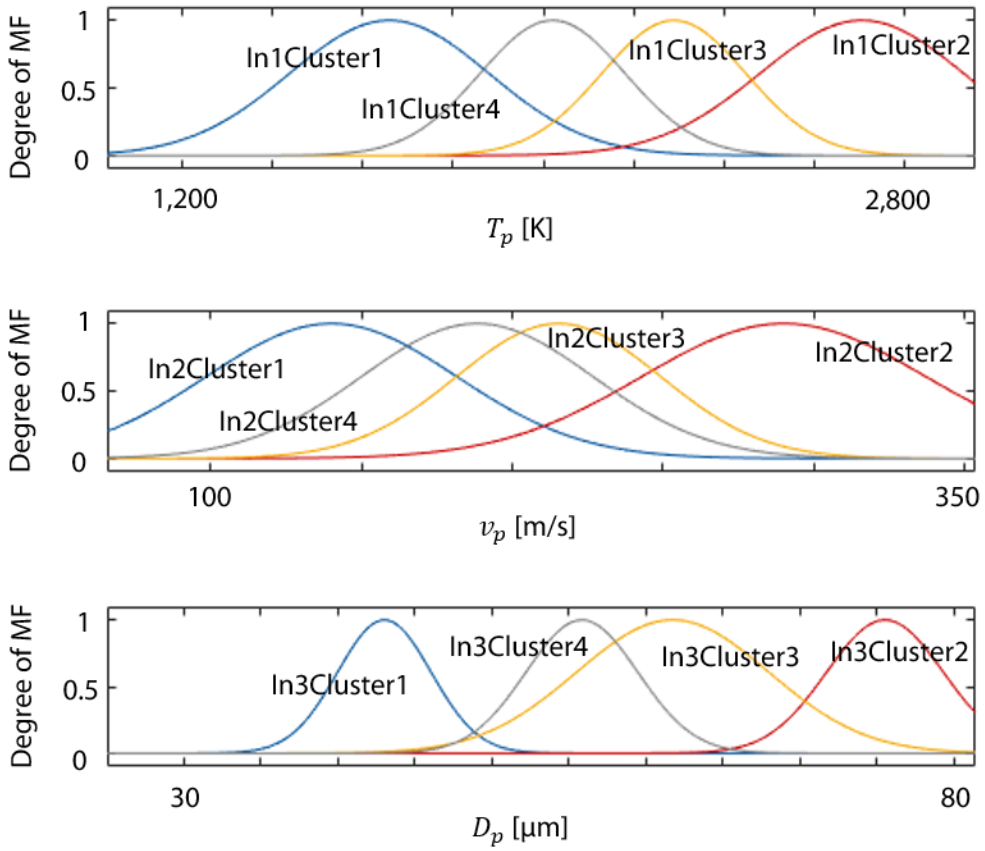

Figure 69: Input membership functions of the ANFIS model [BHD22]

In the following, the results of the developed ANFIS model in Block B of the expert system are presented. As mentioned above, totally 150 data sets of particle properties and LDEs are available, which include the 100 original experimental data from Chapter 5 and the 50 augmented data from section 7.4 of this chapter. These data are separated into two unique groups, with 120 data sets for training and 30 data sets for testing the ANFIS model. Table 10 shows the results of the developed ANFIS model for the 30 test data sets. The average particle temperatures ($\bar{T}_p$), velocities ($\bar{v}_p$) and sizes ($\bar{D}_p$) of the test cases with their corresponding experimental local deposition efficiencies (LDE_{exp}) and predicted values by ANFIS (LDE_{ANFIS}) are listed in Table 10.

Table 10: Results of the ANFIS model for the 30 test sets [BHD22]

Test index	$\bar{T}_p$ [K]	$\bar{v}_p$ [m/s]	$\bar{D}_p$ [µm]	LDE_{exp} [%]	LDE_{ANFIS} [%]
1	1568.09	167.69	42.56	8.78	9.42
2	1564.87	91.36	40.24	6.09	6.44
3	1786.35	167.36	44.23	11.91	13.94
4	2052.55	216.13	51.43	27.28	26.57
5	2893.08	333.54	78.40	44.44	44.34
6	2368.36	202.91	59.69	36.36	35.86
7	2054.55	152.27	50.87	22.11	21.07
8	2152.31	226.81	54.97	32.04	32.18
9	1921.74	196.62	48.83	21.20	21.05
10	2135.98	159.40	52.33	26.55	24.00
11	1671.47	168.11	44.63	14.36	12.19
12	2289.24	189.54	56.96	33.65	33.95
13	2179.66	207.15	53.72	31.00	29.63
14	2535.18	271.78	61.26	36.28	35.91
15	1818.67	141.26	40.83	11.61	12.26
16	1863.90	123.12	46.57	13.59	15.28
17	2644.25	294.00	67.78	43.14	43.20
18	1826.92	152.03	45.47	13.43	14.84
19	1640.27	155.41	42.12	10.32	10.15
20	2690.62	306.01	68.09	41.88	42.34
21	1964.10	210.62	47.31	20.42	18.81
22	2535.89	277.67	61.83	38.08	35.94
23	2846.40	329.43	75.96	43.96	43.77
24	1750.51	121.38	37.02	8.50	8.80
25	1501.95	101.55	37.82	4.5	4.44
26	2239.33	233.01	55.45	32.97	31.98
27	2902.06	336.19	78.11	44.58	43.93
28	2582.08	248.92	65.19	40.15	39.28
29	1954.29	176.83	49.53	20.72	21.07
30	1977.95	198.33	50.81	24.47	25.31

Figure 70 shows the predicted LDE values versus their experimental targets for the 30 test data sets. Each test index in this figure corresponds to a combination of particle properties listed in Table 10. The ANFIS model is able to predict LDE accurately with RMSE of approximately 1.1 [%]. When investigating the data points plotted in Figure 70 and their corresponding values from Table 10, it can be concluded that the deposition efficiency tends to increase with increasing particle size, velocity, and temperature. However, this behavior is nonlinear. The accuracy metric mentioned above (RMSE ≈ 1.1 [%]) for the prediction of LDE indicates that this nonlinearity is well analyzed by the ANFIS model for the typical range of particle properties in APS. As investigated in Chapter 5, the particles with relatively larger diameters have greater momentum, which leads to a deeper penetration into the plasma jet. Furthermore, the cascaded design of the three-cathode plasma gun allows larger particles to stay in the high temperature core of the plasma jet [BÖ16], contributing positively to both their melting ratio and velocity to achieve the best DE in the plasma jet.

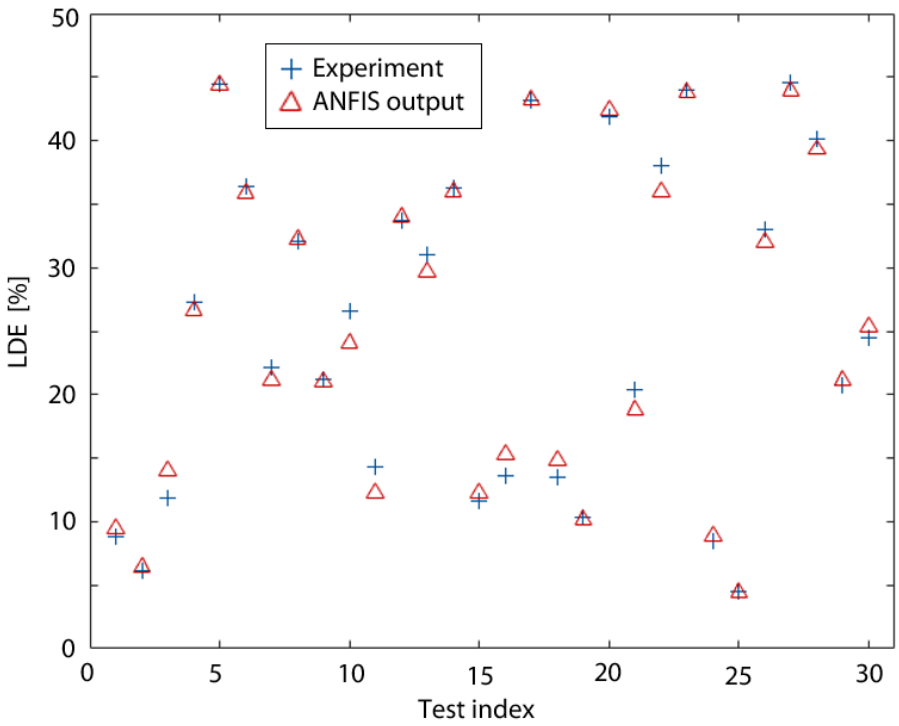

Figure 70: Results of the predicted LDE by ANFIS model for 30 test sets [BHD22]

7.6 Test Case

In Block A of the introduced expert system, the in-flight particle properties are predicted by the SVM models. As described earlier, the SVM models are trained based on simulations of the plasma jet with different process parameters. It was then shown in the Block B of the expert system that the developed ANFIS model is able to predict LDE from the particle properties accurately with the RMSE of about 1.1 [%]. In this section, the concept of predicting the global DE by the developed expert system trained with the LDE data sets is demonstrated with a test case. To present the results of the expert system for this test case, the process parameters listed in Table 11 are considered, using the three-cathode gun TriplexPro™-210 and the feedstock material Al_2O_3 with a particle size distribution of -45 +22 μm. It should be mentioned that the process parameters of this test case are the same as those used in Chapter 5, Table 6.

Table 11: Process parameters of the test case to predict global DE using the expert system

Parameter [unit]	Value
Current [A]	500
Argon [SLPM]	60
Carrier gas (Ar) [SLPM]	5.5
Powder feed rate [g/min]	11
Spray distance [mm]	100

Figure 71 shows the results of the average particle temperatures and velocities for SVM, simulation and the corresponding experimental measurements. The data for the experimental case were obtained from the measurements in Chapter 5. The particle sizes and velocities were captured with the HiWatch, while the particle temperatures were measured with the DPV-2000. The comparison of the average particle properties confirms the previous validation of the simulation models and demonstrates the accurate replication of the simulation data with SVM. The SVM models can predict mean particle velocities with R-squared of $R_{sq,v} \approx 0.97$ and mean particle temperatures with $R_{sq,T} \approx 0.82$, indicating more accuracy in prediction of particle velocities. This can be explained by the strong correlation of the particle velocity with the particle size distribution and its drag force. According to [FHB14], in general and for a constant drag coefficient, the particle velocity is proportional to the square root of the ratio of the distance traveled, divided by the particle diameter. On the other hand, the influencing factors

on the particle temperatures are much more complicated, as radiation, heat transfer, particle vaporization and other physicochemical mechanisms play a dominant role. Hence, considering the particle size distribution as one of the inputs of the ML models, it is expected to have a better prediction accuracy for the particle velocities.

It must be pointed out that the experimental measurements of particle velocities are more precise than that of particle temperatures. This is due to the non-homogeneous temperature distribution within the particles. The particle diagnostic devices are only able to measure the surface temperature of the particles. Furthermore, the relatively cold particles, which are not adequately illuminated, cannot be detected by the diagnostic systems. On the other hand, the simulation results and the corresponding predicted values by SVM show the average particle temperature based on the governing heat transfer equations of the particles. This indicates that the measured value for the particle temperature is subject to some uncertainties as a reference.

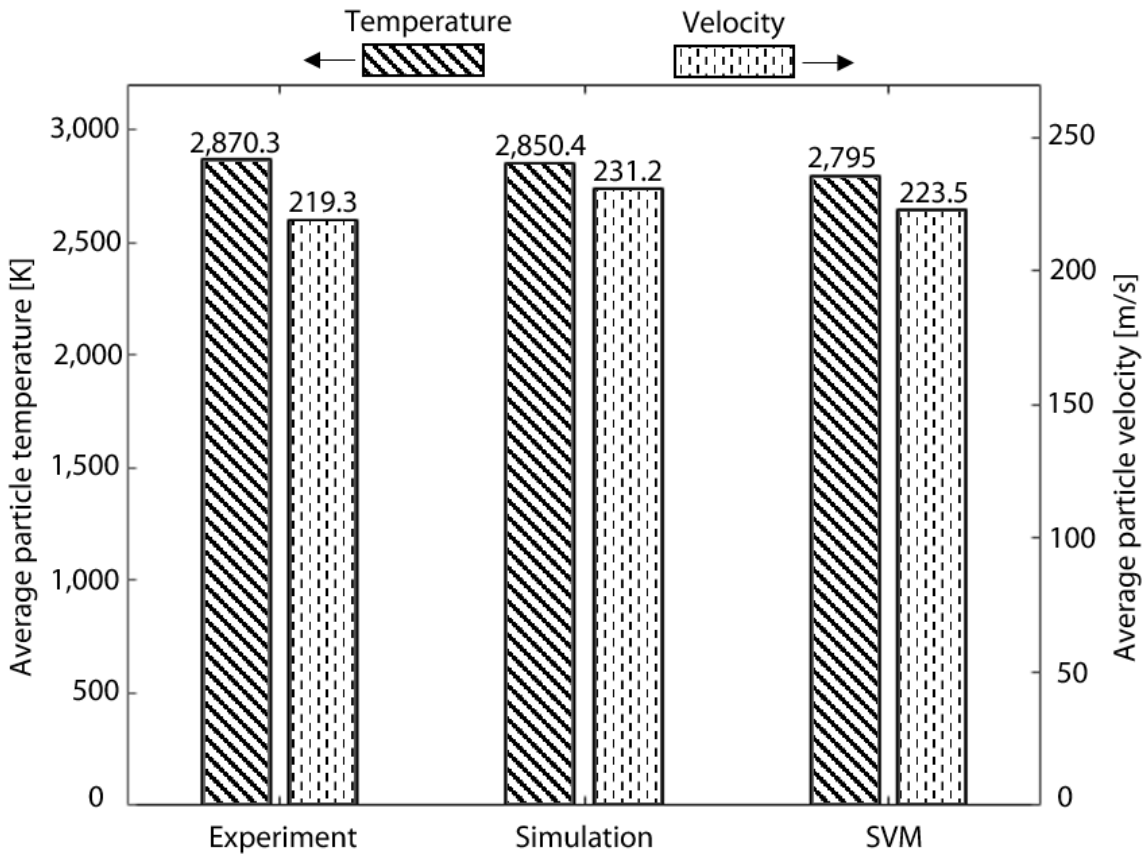

Figure 71: Results of the mean particle properties for experiment, simulation and SVM using the process parameters listed in Table 11 [BHD22]

The results of the mean particle properties predicted by the SVM models in Block A are fed into the ANFIS model in Block B to predict the global DE. The bar chart shown in Figure 72 makes a comparison between the predicted DE and the measured DE for the test case utilizing the process parameters listed in Table 11. The experimental measurements to determine the global DE for the bar chart shown in Figure 72 (left bar) were performed based on the norm [DIN17]. The DE was measured by weighing a specimen before and after coating with respect to the total mass of sprayed material during the coating process. The result of the predicted DE is in a good agreement with the corresponding experimental target. This demonstrates the proof of concept that the developed expert system is capable of predicting the global DE based on the norm, while being trained with spatially resolved deposition efficiencies on the substrate. This confirms the motivation of using LDE data sets to develop and fine-tune such an expert system, while providing that much experimental data for the global DE is hardly practical.

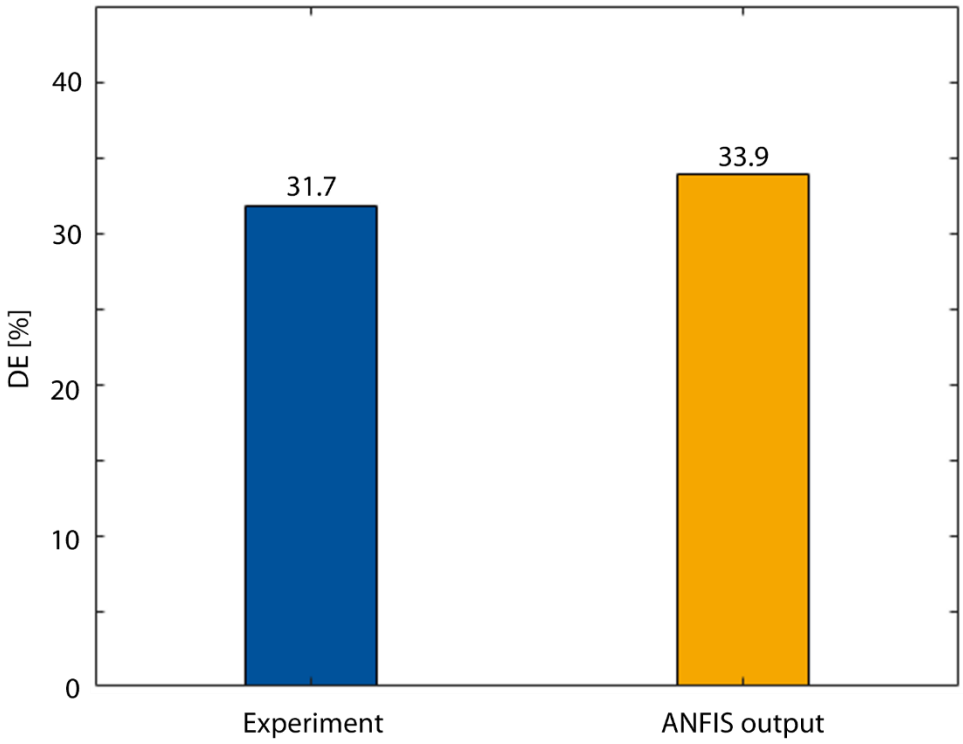

Figure 72: Comparison of the experimental DE and its corresponding predicted DE by ANFIS using the SVM results for the process parameters listed in Table 11 [BHD22]

7.7 Conclusion

Deposition efficiency (DE) serves as a key performance indicator in plasma spraying, which is tailored by dozens of intrinsic and extrinsic influencing factors. Due to the nonlinear and complex interdependencies of these influencing factors, increasing DE has always been a challenging undertaking in the process development of plasma spraying. Hence, employing modern computer-aided algorithms is inevitable to navigate these challenges. This chapter aimed to tackle this task by developing an expert system to predict DE using state-of-the-art AI techniques. The developed expert system consists of two subsystems: one for predicting particle properties from process parameters using a support vector machine, and another for predicting DE from particle properties using an adaptive neuro-fuzzy inference system. The developed expert system can predict LDE accurately with RMSE of about 1.1 [%] through the combination of ANFIS and SVM models. The results revealed that DE tends to rise with increasing particle size, velocity, and temperature, whereas this behavior is nonlinear. Furthermore, the concept to predict global DE from spatially resolved DE on the substrate was demonstrated. It should be pointed out that the DE may depend also on other parameters, such as powder feed rate, torch traverse velocity or spraying distance in general. Additionally, the developed expert system can contribute to the acceleration of the coating development process in APS.

8 Summary and Outlook

In the context of manufacturing technology, the so-called Digital Shadow combines domain-specific models with data-driven techniques inferred by autonomous agents to create a sufficiently accurate image of the production processes including all relevant data. This concept is primarily realized by the integration of the Artificial Intelligence (AI) methods, with the aim of system optimization, controlling as well as prognostics. With respect to the aforementioned definition, this dissertation is devoted to the development of the primary steps towards a Digital Shadow in plasma spraying with the ultimate goal of improving the process efficiency.

Deposition efficiency (DE) is a major performance measure in plasma spraying, which is influenced by a variety of internal and external variables. Because of the nonlinear and complicated interdependencies of the contributing factors, enhancing DE has always been a difficult task in the plasma spraying process development. To address this issue, modern AI methods were used in this work to develop and combine domain-specific models to predict DE. For this purpose, both simulation and experimental data from the entire process chain of APS were employed to train AI models, and combine them in the frame of a so-called expert system. These data include machine or process parameters, in-flight particle properties and deposition efficiency on the substrate.

The developed expert system consists of two subsystems: one for predicting in-flight particle properties from process parameters using support vector machine (SVM) technique, and another for predicting DE from particle properties using an adaptive neuro-fuzzy inference system (ANFIS). To tackle the problem of insufficient data for training the aforementioned AI models two approaches were pursued: 1) A method was developed for in situ determination of spatially resolved deposition efficiencies on the substrate, namely local deposition efficiency (LDE). By using LDE, sufficient amount of data for learning algorithms could be generated, while providing that much data for ex situ measurements of global DE and their corresponding particle properties would be impractical. 2) Simulation data for in-flight particle properties were generated by recycling the simulation models of the plasma jet already developed at IOT. The combination of these two strategies provided the aggregated and purpose-driven data sets required for a Digital Shadow in plasma spraying.

The developed SVM models based on simulation models, namely metamodels, are able to replicate the average particle properties for different process parameters with high accuracy, while reducing the computational cost dramatically. The SVM models can predict mean particle velocities with R-squared of $R_{sq,v} \approx 0.97$ and mean particle temperatures with $R_{sq,T} \approx 0.82$, indicating more accuracy in prediction of particle velocities. The developed expert system can predict LDE from particle properties accurately with RMSE of about 1.1 [%] through the combination of ANFIS and SVM models. The results indicated that DE tends to increase with rising particle size, velocity, and temperature, illustrating a non-linear behavior. This nonlinearity is captured well by the developed predictive models. Moreover, the concept of predicting the global DE based on the spatially resolved deposition efficiencies on the substrate was demonstrated by a test case.

The developed expert system can be used as a tool to adjust the process parameters to produce sustainable and cost-effective coatings. Moreover, it can contribute to the acceleration of the coating development process in APS. Future works could be directed towards establishing an iterative feedback loop based on experimental data sets that encompass global DE and the corresponding in-flight particle properties. This iterative approach aims to improve both the accuracy and range of predictions made by the Digital Shadow. In this regard, the developed expert system also needs to be trained with DEs higher than 50 %. The concept of the iterative feedback loop is depicted in Figure 73. Furthermore, the data generation module can be connected to a database for real-time process optimization. With live data acquisition and controlling, a full-scale Digital Shadow in plasma spraying can be achieved.

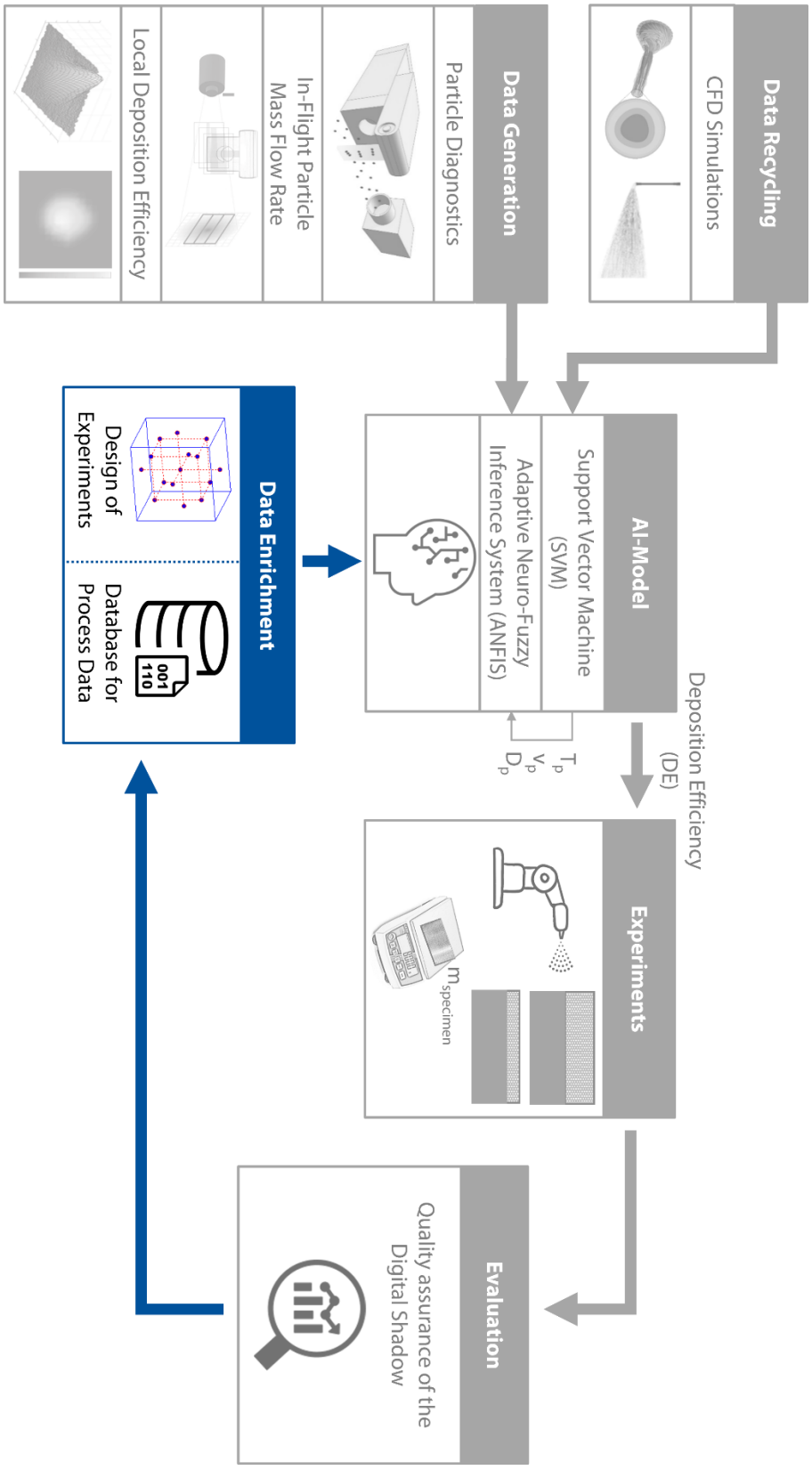

Figure 73: Concept of creating an iterative feedback loop based on experimental data sets and connecting the Digital Shadow with a database

The in situ determination of the LDE in this work was conducted by several grid measurements of the in-flight particle properties using the HiWatch diagnostic system. To avoid the time-consuming grid measurements at various focal planes of the free jet, a Particle Image Velocimetry (PIV) method could be developed. This method involves a pulsed laser and a high-speed camera to detect particles near the substrate. The schematic representation of this concept is shown in Figure 74. The different laser options together with the moving table allow to capture the particles at once and therefore, the LDE can be determined with less effort. Furthermore, the rebounding flow of the non-deposited particles near the substrate has an influence on the incoming particle flow in the free jet. It is supposed that the spatial distribution of the particle flow near the substrate is broader than that in the free jet. The effect of the bouncing flow of the non-deposited particles on the LDE can be also considered by this concept.

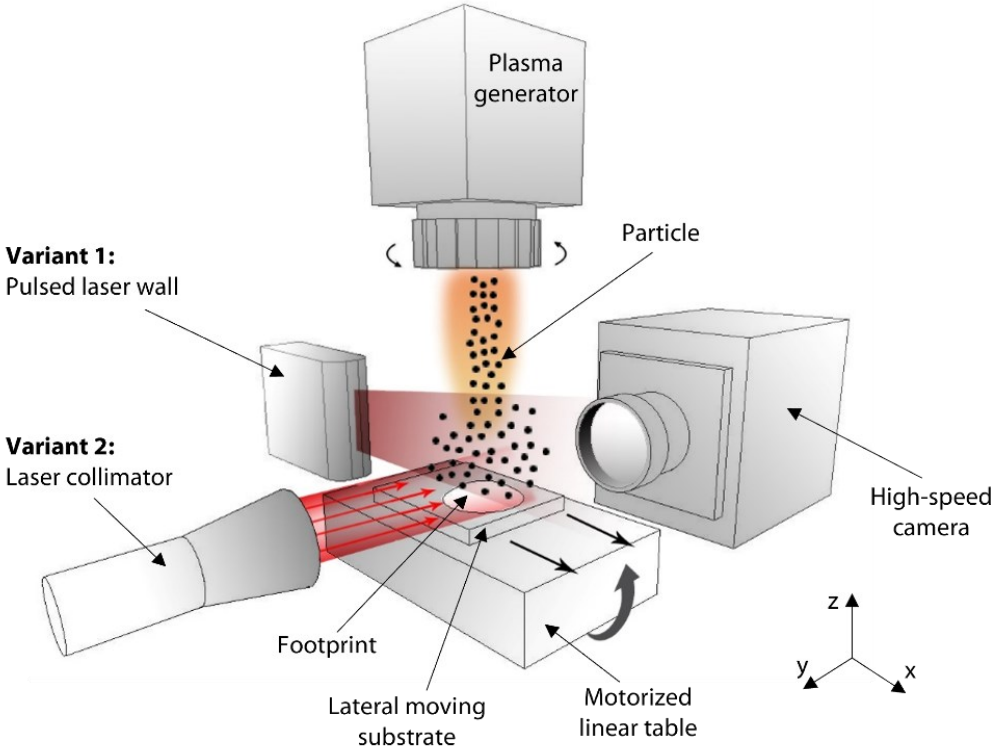

Figure 74: Schematic illustration of an experimental setup with a high-speed camera and a laser for in situ determination of LDE without lengthy grid measurements

9 References

[AK15] M. Awad, R. Khanna, Efficient Learning Machines, Berkeley, CA: Apress, 2015, ISBN 978-1-4302-5989-3

[Alp10] E. Alpaydın, Introduction to machine learning, Cambridge, Mass.: MIT Press, 2. ed., 2010, ISBN 978-0-262-01243-0

[ARP88] J. A. Anderson, E. Rosenfeld, A. Pellionisz, Neurocomputing: MIT Press, 1988, ISBN 0262510758

[AS09] R. Akerkar, P. Sajja, Knowledge-based systems: Jones & Bartlett Publishers, 2009, ISBN 1449612946

[ASA+12] A. Al-Hmouz, J. Shen, R. Al-Hmouz, J. Yan, Modeling and Simulation of an Adaptive Neuro-Fuzzy Inference System (ANFIS) for Mobile Learning, IEEE Transactions on Learning Technologies 5 **3** (2012), 226–237

[BBD+21] F. Becker, P. Bibow, M. Dalibor, A. Gannouni, V. Hahn, C. Hopmann, M. Jarke, I. Koren, M. Kröger, J. Lipp, J. Maibaum, J. Michael, B. Rumpe, P. Sapel, N. Schäfer, G. J. Schmitz, G. Schuh, A. Wortmann, A Conceptual Model for Digital Shadows in Industry and Its Application, in: A. Ghose,J. Horkoff,V. E. Silva Souza,J. Parsons,J. Evermann Conceptual Modeling, Cham: Springer International Publishing, 2021, 271–281, ISBN 978-3-030-89021-6

[BBZ+11] K. Bobzin, N. Bagcivan, L. Zhao, I. Petkovic, J. Schein, K. Hartz-Behrend, S. Kirner, J.-L. Marqués, G. Forster, Modelling and diagnostics of multiple cathodes plasma torch system for plasma spraying, Frontiers of Mechanical Engineering (2011)

[BCF19] B. R. Barricelli, E. Casiraghi, D. Fogli, A Survey on Digital Twin: Definitions, Characteristics, Applications, and Design Implications, IEEE Access 7 (2019), 167653–167671

[BDJ+22] P. Brauner, M. Dalibor, M. Jarke, I. Kunze, I. Koren, G. Lakemeyer, M. Liebenberg, J. Michael, J. Pennekamp, C. Quix, B. Rumpe, W. van der Aalst, K. Wehrle, A. Wortmann, M. Ziefle, A Computer Science Perspective on Digital Transformation in Production, ACM Transactions on Internet of Things 3 **2** (2022), 1–32

[BEF84] J. C. Bezdek, R. Ehrlich, W. Full, FCM: The fuzzy c-means clustering algorithm, Computers & Geosciences 10 **2-3** (1984), 191–203

[BGA+21] T. Bergs, S. Gierlings, T. Auerbach, A. Klink, D. Schraknepper, T. Augspurger, The Concept of Digital Twin and Digital Shadow in Manufacturing, Procedia CIRP 101 **3** (2021), 81–84

[BGV92] B. E. Boser, I. M. Guyon, V. N. Vapnik, A training algorithm for optimal margin classifiers, in: D. Haussler Proceedings of the fifth annual workshop on Computational learning theory - COLT '92, New York, New York, USA: ACM Press, 1992, 144–152, ISBN 089791497X

[BHD22] K. Bobzin, H. Heinemann, S. R. Dokhanchi, Development of an Expert System for Prediction of Deposition Efficiency in Plasma Spraying, Journal of Thermal Spray Technology (2022)

[BM12] A. Behera, S. C. Mishra, Prediction and Analysis of Deposition Efficiency of Plasma Spray Coating Using Artificial Intelligence Method, Open Journal of Composite Materials 02 **02** (2012), 54–60

[BN06] C. M. Bishop, N. M. Nasrabadi, Pattern recognition and machine learning: Springer, 2006

[BÖ16] K. Bobzin, M. Öte, Modeling Multi-Arc Spraying Systems, Journal of Thermal Spray Technology 25 **5** (2016), 920–932

[BÖ17] K. Bobzin, M. Öte, Modeling Plasma–Particle Interaction in Multi-Arc Plasma Spraying, Journal of Thermal Spray Technology 26 **3** (2017), 279–291

[Bob13] K. Bobzin, Oberflachentechnik fur den Maschinenbau: John Wiley & Sons, 2013, ISBN 3527681493

[BÖK+20] K. Bobzin, M. Öte, M. A. Knoch, I. Alkhasli, Macroscopic Modeling of an Agglomerated and Sintered Particle in Air Plasma Spraying, Journal of Thermal Spray Technology 29 **1-2** (2020), 13–24

[BÖK+20] K. Bobzin, M. Öte, M. A. Knoch, H. Heinemann, Influence of the Injector Head Geometry on the Particle Injection in Plasma Spraying, Journal of Thermal Spray Technology 29 **4** (2020), 534–545

[BÖS+16] K. Bobzin, M. Öte, J. Schein, S. Zimmermann, K. Möhwald, C. Lummer, Modelling the Plasma Jet in Multi-Arc Plasma Spraying, Journal of Thermal Spray Technology 25 **6** (2016), 1111–1126

[BÖS+17] K. Bobzin, M. Öte, J. Schein, S. Zimmermann, Numerical Study on Plasma Jet and Particle Behavior in Multi-arc Plasma Spraying, Journal of Thermal Spray Technology 26 **5** (2017), 811–830

[BV17] E. Bakan, R. Vaßen, Ceramic Top Coats of Plasma-Sprayed Thermal Barrier Coatings: Materials, Processes, and Properties, Journal of Thermal Spray Technology 26 **6** (2017), 992–1010

[BWH+20] K. Bobzin, W. Wietheger, H. Heinemann, S. R. Dokhanchi, Determination of local deposition efficiency based on in-flight particle diagnostics in plasma spraying, Surface and Coatings Technology 399 (2020), 126118

[BWH+21] K. Bobzin, W. Wietheger, H. Heinemann, S. R. Dokhanchi, M. Rom, G. Visconti, Prediction of Particle Properties in Plasma Spraying Based on Machine Learning, Journal of Thermal Spray Technology 30 **7** (2021), 1751–1764

[BWK+20] K. Bobzin, W. Wietheger, M. A. Knoch, S. R. Dokhanchi, Estimation of Particle Mass Flow Rate in Free Jet Using In-Flight Particle Diagnostics in Plasma Spraying, Journal of thermal spray technology JTST (2020). doi:10.1007/s11666-020-01027-4 / pages 11 Seiten (2020)

[Dav04] J. R. Davis, Handbook of thermal spray technology: ASM International, 2004, ISBN 0871707950

[DGH+01] J.-L. Dorier, M. Gindrat, C. Hollenstein, A. Salito, M. Loch, G. Barbezat, Time-resolved imaging of anodic arc root behavior during fluctuations of a DC plasma spraying torch, IEEE Transactions on Plasma Science 29 **3** (2001), 494–501

[DIN17] DIN e.V. **17836:2017-04,** Thermisches Spritzen - Bestimmung der Auftragrate beim thermischen Spritzen Beuth Verlag, Berlin, DIN e.V., 2017

[DPB13] S. Datta, D. K. Pratihar, P. P. Bandyopadhyay, Hierarchical adaptive neuro-fuzzy inference systems trained by evolutionary algorithms to model plasma spray coating process, Journal of Intelligent & Fuzzy Systems 24 **2** (2013), 355–362

[Ern07] F. B. G. Ernst, Qualitätskontrolle auf Basis optischer Prozessdiagnostik und neuronaler Netze beim thermischen Spritzen, Zugl.: Aachen, Techn. Hochsch., Diss., 2007, Aachen: Shaker, 2007, ISBN 3832262458

[Ert11] W. Ertel, Introduction to Artificial Intelligence, London: Springer London, 2011, ISBN 978-0-85729-298-8

[FHB14] P. L. Fauchais, J. V. Heberlein, M. I. Boulos, Thermal Spray Fundamentals, From Powder to Part, Boston, MA, s.l.: Springer US, 2014, ISBN 978-0-387-68991-3

[FLS05] K.-T. Fang, R. Li, A. Sudjianto, Design and Modeling for Computer Experiments: Chapman and Hall/CRC, 2005, ISBN 9780429143762

[FMV+06] P. Fauchais, G. Montavon, M. Vardelle, J. Cedelle, Developments in direct current plasma spraying, Surface and Coatings Technology 201 **5** (2006), 1908–1921

[FV10] P. Fauchais, M. Vardelle, Sensors in Spray Processes, Journal of Thermal Spray Technology 19 **4** (2010), 668–694

[GAU+20] T. Gurgenc, O. Altay, M. Ulas, C. Ozel, Extreme learning machine and support vector regression wear loss predictions for magnesium alloys coated using various spray coating methods, Journal of Applied Physics 127 **18** (2020), 185103

[GMC05] S. Guessasma, G. Montavon, C. Coddet, Velocity and temperature distributions of alumina–titania in-flight particles in the atmospheric plasma spray process, Surface and Coatings Technology 192 **1** (2005), 70–76

[GMG+03] S. Guessasma, G. Montavon, P. Gougeon, C. Coddet, Designing expert system using neural computation in view of the control of plasma spray processes, Materials & Design 24 **7** (2003), 497–502

[Hay09] S. S. Haykin, Neural networks and learning machines, New York: Pearson, 3. ed., 2009, ISBN 978-0-13-147139-9

[HG08] A. Hamam, N. D. Georganas, A comparison of Mamdani and Sugeno fuzzy inference systems for evaluating the quality of experience of Hapto-Audio-Visual applications, in: 2008 IEEE International Workshop on Haptic Audio visual Environments and Games, IEEE, 2008, 87–92, ISBN 978-1-4244-2668-3

[Hol14] A. Holzinger, Biomedical Informatics, Cham: Springer International Publishing, 2014, ISBN 978-3-319-04527-6

[Jan93] J.-S. Jang, ANFIS: adaptive-network-based fuzzy inference system, IEEE Transactions on Systems, Man, and Cybernetics 23 **3** (1993), 665–685

[JH08] V. R. Joseph, Y. Hung, Orthogonal-maximin Latin hypercube designs, Statistica Sinica (2008), 171–186

[JLC07] M.-D. Jean, B.-T. Lin, J.-H. Chou, Design of a fuzzy logic approach based on genetic algorithms for robust plasma-sprayed zirconia depositions, Acta Materialia 55 **6** (2007), 1985–1997

[JMM96] A. K. Jain, J. Mao, K. M. Mohiuddin, Artificial neural networks: a tutorial, Computer 29 **3** (1996), 31–44

[JS95] J.-S. Jang, C.-T. Sun, Neuro-fuzzy modeling and control, Proceedings of the IEEE 83 **3** (1995), 378–406

[KKT+18] W. Kritzinger, M. Karner, G. Traar, J. Henjes, W. Sihn, Digital Twin in manufacturing: A categorical literature review and classification, IFAC-PapersOnLine 51 **11** (2018), 1016–1022

[KMB+11] A.-F. Kanta, G. Montavon, C. C. Berndt, M.-P. Planche, C. Coddet, Intelligent system for prediction and control: Application in plasma spray process, Expert Systems with Applications 38 **1** (2011), 260–271

[KMV+08] A.-F. Kanta, G. Montavon, M. Vardelle, M.-P. Planche, C. C. Berndt, C. Coddet, Artificial Neural Networks vs. Fuzzy Logic: Simple Tools to Predict and Control Complex Processes—Application to Plasma Spray Processes, Journal of Thermal Spray Technology 17 **3** (2008), 365–376

[Kro08] A. Krogh, What are artificial neural networks?, Nature biotechnology 26 **2** (2008), 195–197

[Lan06] K. Landes, Diagnostics in plasma spraying techniques, Surface and Coatings Technology 201 **5** (2006), 1948–1954

[Lee90] C. C. Lee, Fuzzy logic in control systems: fuzzy logic controller. I, IEEE Transactions on Systems, Man, and Cybernetics 20 **2** (1990), 404–418

[LFK+14] H. Lasi, P. Fettke, H.-G. Kemper, T. Feld, M. Hoffmann, Industry 4.0, Business & Information Systems Engineering 6 **4** (2014), 239–242

[LFS09] J. L. Marqués, G. Forster, J. Schein, Multi-Electrode Plasma Torches: Motivation for Development and Current State-of-the-Art, The Open Plasma Physics Journal 2 **1** (2009), 89–98

[LPK+13] T. Liu, M. P. Planche, A. F. Kanta, S. Deng, G. Montavon, K. Deng, Z. M. Ren, Plasma Spray Process Operating Parameters Optimization Based on Artificial Intelligence, Plasma Chemistry and Plasma Processing 33 **5** (2013), 1025–1041

[Lug02] Lugscheider, E., Handbuch der thermischen Spritztechnik, Technologien - Werkstoffe - Fertigung, Düsseldorf: Verl. für Schweißen und Verwandte Verfahren DVS-Verl., 2002, ISBN 3-87155-186-4

[MA75] E. H. Mamdani, S. Assilian, An experiment in linguistic synthesis with a fuzzy logic controller, International Journal of Man-Machine Studies 7 **1** (1975), 1–13

[MMA09] R. H. Myers, D. C. Montgomery, C. M. Anderson-Cook, Response surface methodology, Process and product optimization using designed experiments, Hoboken, NJ: Wiley, 3. ed., 2009, ISBN 978-0-470-17446-3

[Mon13] D. C. Montgomery, Design and analysis of experiments, Hoboken, NJ: Wiley, 8. ed., 2013, ISBN 978-1118-14692-7

[Mon14] L. Monostori, Cyber-physical Production Systems: Roots, Expectations and R&D Challenges, Procedia CIRP 17 (2014), 9–13

[MP43] W. S. McCulloch, W. Pitts, A logical calculus of the ideas immanent in nervous activity, The Bulletin of Mathematical Biophysics 5 **4** (1943), 115–133

[MVS07] G. Mauer, R. Vaßen, D. Stöver, Comparison and Applications of DPV-2000 and Accuraspray-g3 Diagnostic Systems, Journal of Thermal Spray Technology 16 **3** (2007), 414–424

[MVS11] G. Mauer, R. Vaßen, D. Stöver, Plasma and Particle Temperature Measurements in Thermal Spray: Approaches and Applications, Journal of Thermal Spray Technology 20 **3** (2011), 391–406

[Nia20] I. Niankara, Research Data Recycling through Open Sharing and Reuse: A Case Study of Sustainable Digital Good Consumption in the Sharing Economy:, 2020

[NN23a] NN, The MathWorks, Inc., Statistics and Machine Learning Toolbox™ User's Guide, Retrieved February 05, 2023, from https://de.mathworks.com/help/stats/machine-learning-in-matlab.html (23a)

[NN23b] NN, Oerlikon Metco's Powder Feeder Data Sheet, Retrieved February 05, 2023, from https://www.oerlikon.com/metco/en/products-services/thermal-spray-equipment/thermal-spray-components/feeders/?tab=volumetric (23b)

[NTA+18] H. F. Nweke, Y. W. Teh, M. A. Al-garadi, U. R. Alo, Deep learning algorithms for human activity recognition using mobile and wearable sensor networks: State of the art and research challenges, Expert Systems with Applications 105 (2018), 233–261

[O'R85] J. O'Rourke, Finding minimal enclosing boxes, International Journal of Computer & Information Sciences 14 **3** (1985), 183–199

[Öte16] M. Öte, Understanding multi-arc plasma spraying, Dissertation:, 2016, ISBN 978-3-8440-4598-7

[Paw08] L. Pawłowski, The science and engineering of thermal spray coatings, Chichester, England, Hoboken, NJ: Wiley, 2nd ed., 2008, ISBN 978-0-471-49049-4

[Pet09] L. Peterson, K-nearest neighbor, Scholarpedia 4 **2** (2009), 1883

[PGN+15] A. H. Pakseresht, E. Ghasali, M. Nejati, K. Shirvanimoghaddam, A. H. Javadi, R. Teimouri, Development empirical-intelligent relationship between plasma spray parameters and coating performance of Yttria-Stabilized Zirconia, The International Journal of Advanced Manufacturing Technology 76 **5-8** (2015), 1031–1045

[QFL08] F. Qunbo, W. Fuchi, W. Lu, Study of Flying Particles in Plasma Spraying, Journal of Materials Engineering and Performance 17 **5** (2008), 621–626

[RHO+15] J. Ríos, J. C. Hernandez, M. Oliva, F. Mas, Product avatar as digital counterpart of a physical individual product: Literature review and implications in an aircraft, Transdisciplinary Lifecycle Analysis of Systems (2015), 657–666

[Ric87] E. Rich, Artificial intelligence, New York: McGraw-Hill, 6th print, 1987, ISBN 0070522618

[RN16] S. J. Russell, P. Norvig, Artificial intelligence, A modern approach, Boston, Columbus, Indianapolis: Pearson, Third edition, Global edition, 2016, ISBN 978-0-13-604259-4

[SBD+06] K. E. Schneider, V. Belashchenko, M. Dratwinski, S. Siegmann, A. Zagorski, Thermal spraying for power generation components: John Wiley & Sons, 2006, ISBN 3527609385

[SBR+16] G. Schuh, M. Blum, J. Reschke, M. Birkmeier, Der Digitale Schatten in der Auftragsabwicklung, Zeitschrift für wirtschaftlichen Fabrikbetrieb 111 **1-2** (2016), 48–51

[SBR+16] G. Schuh, T. Bauernhansl, G. Reinhart, J. Krüger, WGP-Standpunkt Industrie 4.0, Wissenschaftliche Gesellschaft für Produktionstechnik WGP eV (2016)

[SC04] J. Shawe-Taylor, N. Cristianini, Kernel methods for pattern analysis: Cambridge university press, 2004, ISBN 0521813972

[See05] K. Seemann, Vorhersage von Prozess- und Schichtcharakteristiken beim atmosphärischen Plasmaspritzen mittels statistischer Modelle und neuronaler Netze, Zugl.: Aachen, Techn. Hochsch., Diss., 2005, Aachen: Mainz, 1. Aufl., 2005, ISBN 3861307324

[SL12] Y. Shao, R. S. Lunetta, Comparison of support vector machine, neural network, and CART algorithms for the land-cover classification using limited training data points, ISPRS Journal of Photogrammetry and Remote Sensing 70 (2012), 78–87

[SRL+08] J. Schein, M. Richter, K. D. Landes, G. Forster, J. Zierhut, M. Dzulko, Tomographic Investigation of Plasma Jets Produced by Multielectrode Plasma Torches, Journal of Thermal Spray Technology 17 **3** (2008), 338–343

[SS04] A. J. Smola, B. Schölkopf, A tutorial on support vector regression, Statistics and computing 14 **3** (2004), 199–222

[SS11] H. Seetha, R. Saravanan, On improving the generalization of SVM classifier, Computer Networks and Intelligent Computing (2011), 11–20

[SS18] B. Scholkopf, A. J. Smola, Learning with kernels: support vector machines, regularization, optimization, and beyond: MIT Press, 2018, ISBN 0262536579

[SSV+09] S. Sampath, V. Srinivasan, A. Valarezo, A. Vaidya, T. Streibl, Sensing, Control, and In Situ Measurement of Coating Properties: An Integrated Approach Toward Establishing Process-Property Correlations, Journal of Thermal Spray Technology 18 **2** (2009), 243–255

[Suz11] K. Suzuki, Artificial Neural Networks - Methodological Advances and Biomedical Applications, Erscheinungsort nicht ermittelbar: IntechOpen, 2011, ISBN 978-953-307-243-2

[SWL+16] G. Schuh, P. Walendzik, M. Luckert, M. Birkmeier, A. Weber, M. Blum, Keine Industrie 4.0 ohne den Digitalen Schatten, Zeitschrift für wirtschaftlichen Fabrikbetrieb 111 **11** (2016), 745–748

[SZ16] M. D. Shields, J. Zhang, The generalization of Latin hypercube sampling, Reliability Engineering & System Safety 148 (2016), 96–108

[TPT22] A. Tsantekidis, N. Passalis, A. Tefas, Recurrent neural networks, in: Deep Learning for Robot Perception and Cognition, Elsevier, 2022, 101–115, ISBN 9780323857871

[TS85] T. Takagi, M. Sugeno, Fuzzy identification of systems and its applications to modeling and control, IEEE Transactions on Systems, Man, and Cybernetics SMC-15 **1** (1985), 116–132

[TZL+19] F. Tao, H. Zhang, A. Liu, A. Y. C. Nee, Digital Twin in Industry: State-of-the-Art, IEEE Transactions on Industrial Informatics 15 **4** (2019), 2405–2415

[ULS17] T. H.-J. Uhlemann, C. Lehmann, R. Steinhilper, The Digital Twin: Realizing the Cyber-Physical Production System for Industry 4.0, Procedia CIRP 61 (2017), 335–340

[Vap99] V. Vapnik, The nature of statistical learning theory: Springer science & business media, 1999, ISBN 0387987800

[VDS+07] R. Venkataraman, G. Das, S. R. Singh, L. C. Pathak, R. N. Ghosh, B. Venkataraman, R. Krishnamurthy, Study on influence of porosity, pore size, spatial and topological distribution of pores on microhardness of as plasma

sprayed ceramic coatings, Materials Science and Engineering: A 445-446 (2007), 269–274

[VMT+15] A. Vardelle, C. Moreau, N. J. Themelis, C. Chazelas, A Perspective on Plasma Spray Technology, Plasma Chemistry and Plasma Processing 35 **3** (2015), 491–509

[VSY+09] M. Vijay, V. Selvarajan, S. Yugeswaran, P. V. Ananthapadmanabhan, K. P. Sreekumar, Effect of Spraying Parameters on Deposition Efficiency and Wear Behavior of Plasma Sprayed Alumina-Titania Composite Coatings, Plasma Science and Technology 11 **6** (2009), 666–673

[WFC00] R. L. Williamson, J. R. Fincke, C. H. Chang, A Computational Examination of the Sources of Statistical Variance in Particle Parameters During Thermal Plasma Spraying, Plasma Chemistry and Plasma Processing 20 **3** (2000), 299–324

[WM13] T. Wiederkehr, H. Müller, Acquisition and Optimization of Three-Dimensional Spray Footprint Profiles for Coating Simulations, Journal of Thermal Spray Technology 22 **6** (2013), 1044–1052

[WRT+10] D. Wroblewski, G. Reimann, M. Tuttle, D. Radgowski, M. Cannamela, S. N. Basu, M. Gevelber, Sensor Issues and Requirements for Developing Real-Time Control for Plasma Spray Deposition, Journal of Thermal Spray Technology 19 **4** (2010), 723–735

[Wu15] Z. Wu, Empirical modeling for processing parameters' effects on coating properties in plasma spraying process, Journal of Manufacturing Processes 19 (2015), 1–13

[WXZ+17] Y. J. Wang, J. Y. Xu, Q. H. Zhao, Y. Wang, B. Gao, Effects of various power process parameters on deposition efficiency of plasma-sprayed Al2O3-40% wt.TiO2 coatings, IOP Conference Series: Materials Science and Engineering 213 (2017), 12042

[XH17] J. Xue, M. Huang, Optimization of Plasma Spray Process VIA Orthogonal Test Design Method, SVM, and Improved PSO, International Journal of Materials, Mechanics and Manufacturing 5 **3** (2017), 153–158

[Zad65] L. A. Zadeh, Fuzzy sets, Information and Control 8 **3** (1965), 338–353

[ZWK+20] J. Zhu, X. Wang, L. Kou, L. Zheng, H. Zhang, Prediction of control parameters corresponding to in-flight particles in atmospheric plasma spray employing convolutional neural networks, Surface and Coatings Technology 394 (2020), 125862

10 Appendix

List of process parameters for the 45 simulations from the CCD method

Sim. No.	Primary gas (Ar) [SLPM]	Electric current [A]	Carrier gas [SLPM]	Powder feed rate [g/min]	Particle size [µm]	Stand-off distance [mm]
1	40.02	470.00	5.38	19.80	-55 +35	140
2	45.74	440.60	4.37	15.60	-35 +15	123
3	45.74	440.60	4.37	15.60	-75 +55	157
4	45.74	440.60	4.37	24.00	-35 +15	157
5	45.74	440.60	4.37	24.00	-75 +55	123
6	45.74	440.60	6.05	15.60	-35 +15	157
7	45.74	440.60	6.05	15.60	-75 +55	123
8	45.74	440.60	6.05	24.00	-35 +15	123
9	45.74	440.60	6.05	24.00	-75 +55	157
10	45.74	499.40	4.37	15.60	-35 +15	157
11	45.74	499.40	4.37	15.60	-75 +55	123
12	45.74	499.40	4.37	24.00	-35 +15	123
13	45.74	499.40	4.37	24.00	-75 +55	157
14	45.74	499.40	6.05	15.60	-35 +15	123
15	45.74	499.40	6.05	15.60	-75 +55	157
16	45.74	499.40	6.05	24.00	-35 +15	157
17	45.74	499.40	6.05	24.00	-75 +55	123
18	50.11	400.00	5.38	19.80	-55 +35	140
19	50.11	470.00	3.36	19.80	-55 +35	140
20	50.11	470.00	5.38	10.20	-55 +35	140
21	50.11	470.00	5.38	19.80	-35 +15	140
22	50.11	470.00	5.38	19.80	-55 +35	100
23	50.11	470.00	5.38	19.80	-55 +35	140
24	50.11	470.00	5.38	19.80	-55 +35	180
25	50.11	470.00	5.38	19.80	-75 +55	140
26	50.11	470.00	5.38	30.00	-55 +35	140
27	50.11	470.00	7.06	19.80	-55 +35	140
28	50.11	540.00	5.38	19.80	-55 +35	140
29	54.15	440.60	4.37	15.60	-35 +15	157

Sim. No.	Primary gas (Ar) [SLPM]	Electric current [A]	Carrier gas [SLPM]	Powder feed rate [g/min]	Particle size [µm]	Stand-off distance [mm]
30	54.15	440.60	4.37	15.60	-75 +55	123
31	54.15	440.60	4.37	24.00	-35 +15	123
32	54.15	440.60	4.37	24.00	-75 +55	157
33	54.15	440.60	6.05	15.60	-35 +15	123
34	54.15	440.60	6.05	15.60	-75 +55	157
35	54.15	440.60	6.05	24.00	-35 +15	157
36	54.15	440.60	6.05	24.00	-75 +55	123
37	54.15	499.40	4.37	15.60	-35 +15	123
38	54.15	499.40	4.37	15.60	-75 +55	157
39	54.15	499.40	4.37	24.00	-35 +15	157
40	54.15	499.40	4.37	24.00	-75 +55	123
41	54.15	499.40	6.05	15.60	-35 +15	157
42	54.15	499.40	6.05	15.60	-75 +55	123
43	54.15	499.40	6.05	24.00	-35 +15	123
44	54.15	499.40	6.05	24.00	-75 +55	157
45	59.87	470.00	5.38	19.80	-55 +35	140

List of process parameters for the 45 simulations from the LHS method

Sim. No.	Primary gas (Ar) [SLPM]	Electric current [A]	Carrier gas [SLPM]	Powder feed rate [g/min]	Particle size [µm]	Stand-off distance [mm]
1	40.36	461.60	6.39	28.80	-35 +15	126
2	40.36	532.90	5.72	15.60	-35 +15	153
3	41.37	473.80	4.04	12.00	-35 +15	169
4	40.70	520.20	6.73	23.40	-75 +55	158
5	42.04	411.50	5.04	20.40	-55 +35	131
6	43.39	402.90	4.37	15.60	-35 +15	164
7	42.71	453.30	5.38	28.20	-55 +35	147
8	42.71	524.90	3.70	10.20	-55 +35	159
9	43.72	482.70	6.73	24.60	-75 +55	123
10	44.06	488.30	6.39	10.20	-55 +35	112
11	45.40	400.20	5.38	23.40	-35 +15	133
12	45.07	446.80	5.72	21.60	-35 +15	116
13	44.40	467.30	5.72	24.60	-75 +55	172
14	46.41	440.40	5.04	10.80	-35 +15	156
15	45.74	534.20	6.73	13.80	-75 +55	100
16	46.75	517.00	4.71	12.60	-75 +55	127
17	47.42	528.60	5.72	21.60	-35 +15	137
18	48.43	413.40	4.71	18.60	-35 +15	121
19	47.76	451.10	4.04	28.80	-35 +15	174
20	49.10	417.40	6.39	27.60	-35 +15	118
21	49.44	421.50	6.05	26.40	-75 +55	107
22	48.77	507.50	5.72	30.00	-55 +35	151
23	50.11	432.70	5.38	15.00	-75 +55	128
24	50.11	538.70	3.70	24.00	-35 +15	102
25	51.46	424.70	6.05	22.20	-75 +55	139
26	51.12	513.70	5.04	16.80	-75 +55	143
27	52.13	427.60	4.37	29.40	-75 +55	112
28	51.79	464.50	3.70	19.20	-55 +35	139
29	52.80	436.30	7.06	17.40	-35 +15	106

Sim. No.	Primary gas (Ar) [SLPM]	Electric current [A]	Carrier gas [SLPM]	Powder feed rate [g/min]	Particle size [µm]	Stand-off distance [mm]
30	53.14	439.40	3.36	26.40	-55 +35	164
31	52.47	479.30	4.37	19.20	-55 +35	177
32	54.48	475.50	4.71	12.60	-55 +35	154
33	53.81	501.20	5.04	21.00	-35 +15	167
34	54.82	418.90	4.04	25.80	-75 +55	142
35	55.49	494.40	3.70	14.40	-35 +15	109
36	55.83	504.30	4.71	22.20	-55 +35	135
37	56.17	523.20	5.38	13.20	-55 +35	119
38	56.84	406.40	6.05	27.00	-55 +35	170
39	56.84	484.80	4.04	11.40	-75 +55	115
40	58.18	497.80	6.39	17.40	-75 +55	105
41	57.85	510.60	6.05	14.40	-55 +35	175
42	58.52	446.20	4.37	25.20	-55 +35	179
43	59.19	457.00	6.73	16.20	-75 +55	161
44	59.19	491.60	6.73	19.80	-55 +35	150
45	59.87	470.30	4.04	18.00	-75 +55	144

Hybrid learning algorithm

The adaptive parameters of the ANFIS model in this study are tuned using a data-driven hybrid learning algorithm. The hybrid method consists of backpropagation for the parameters associated with the input membership functions or premise parameters, and least squares estimation (LSE) for the parameters associated with the output membership functions or consequent parameters.

In the forward pass of the hybrid learning algorithm, the premise parameters are fixed and the consequent parameters are identified by the LSE technique. Let X be an unknown vector with the size of M whose elements are consequent parameters, and let B be the vector of training data with the size of P, then it can be shown that the matrix equation $AX = B$ can be obtained in the adaptive network, where the dimension of $A\ is\ P \times M$. The LSE technique estimates the vector of consequent parameters by minimizing the squared error $\|AX - B\|^2$. The least squares estimate of X, denoted by X^*, is given by

$$X^* = (A^T A)^{-1} A^T B$$

where A^T is the transpose of A.

In the backward pass, the error rates propagate backward and the premise parameters are updated by the gradient descent method, while the consequent parameters are fixed. The error measure for the p-th ($1 \leq p \leq P$) entry of training data can be obtained as the sum of squared errors according to

$$E_p = \sum_{m=1}^{\#(L)} (T_{m,p} - O_{m,p}^L)^2$$

where $T_{m,p}$ is the m-th component of p-th target output vector, and $O_{m,p}^L$ denotes the m-th component of actual output vector produced by the p-th input vector. The overall error E can be calculated by

$$E = \sum_{p=1}^{P} E_p$$

The set of premise parameters can be obtained through the backpropagation procedure that implements gradient descent in E over the parameter space. Let α be a premise parameter of the given adaptive network, then the update formula for the parameter α is

$$\Delta\alpha = -\eta \frac{\partial E}{\partial \alpha}$$

In the above equation, η is the learning rate, which depends on the length of each gradient transition in the parameter space. Please refer to [Jan93] for further detail regarding the hybrid learning algorithm in an adaptive network.

11 Index

11.1 List of Figures

11.2 List of Tables

11.3 List of Equations

11.4 List of Abbreviations

AI	Artificial Intelligence
ANFIS	Adaptive Neuro-Fuzzy Inference System
ANN	Artificial Neural Network
APS	Atmospheric Plasma Spraying
CCD	Central Composite Design
CCL	CFX Command Language
CFD	Computational Fluid Dynamics
CPPS	Cyber-Physical Production Systems
DC	Direct Current
DE	Deposition efficiency
DoE	Design of Experiment
DS	Digital Shadow
DT	Digital Twin
FCM	Fuzzy c-Means
FIS	Fuzzy Inference System
FL	Fuzzy Logic
FNN	Feedforward Neural Network
GA	Genetic Algorithm
HPC	High-Performance Computing
IOT	Surface Engineering Institute
KBS	Knowledge-based System
k-NN	k-nearest neighbor
LDE	Local Deposition Efficiency
LHS	Latin Hypercube Sampling
LSE	Least Squares Estimation
MAPE	Mean Absolute Percentage Error
MF	Membership Function
ML	Machine Learning
OBB	Oriented Bounding Box
PDA	Phase Doppler Anemometry
PIV	Particle Image Velocimetry

PLC	Programmable Logic Controller
PMFR	Particle Mass Flow Rate
PSO	Particle Swarm Optimization Algorithm
RBF	Radial Basis Function
RMSE	Root Mean Square Error
RNN	Recurrent Neural Network
SEM	Scanning Electron Microscope
SRM	Structural Risk Minimization
SST	Shear Stress Transport
SVM	Support Vector Machine
TS	Thermal Spraying

11.5 List of Symbols

A_i	Fuzzy set of the i-th rule, ANFIS
A_e	Area of each element
b	Bias parameter, ANN or SVM
B_i	Fuzzy set of the i-th rule, ANFIS
C	Constant, SVM
c_i	Premise parameter of the i-th rule, ANFIS
D_p	Particle diameter
$E(X_i, Y_s)$	Euclidean distance, k-NN
f_i	Consequent part of the i-th rule, ANFIS
$f(x)$	True values, SVM
$g(x)$	Prediction values, SVM
H_e	Average height of the footprint on each element
h_i	Consequent parameter of the i-th rule, ANFIS
I	Length of the input vector of original data, k-NN
J	Total number of features, k-NN
$k(x_i, x_j)$	Kernel function, SVM
L	Length of a HiWatch image in spray direction
$\dot{m}$	Particle mass flow rate
m_e	Deposited mass on each element
N	Number of data points / particles
n	Number of particles in a HiWatch image
n_i	Number of test particles of simulation i
O^l	Output of the l-th layer, ANFIS
P	Number of predictors, SVM
p_k	Induced local field or activation potential of neuron k, ANN
p_i	Prediction values, SVM
q_i	Consequent parameter of the i-th rule, ANFIS
r_i	Consequent parameter of the i-th rule, ANFIS
R_{sq}	R-squared error
S	Length of the input vector to be classified, k-NN
t	Time for generation of experimental footprint

t_i	Target values, SVM
$\bar{t}$	Mean of target values, SVM
T_p	Particle temperature
$\bar{T}_p$	Mean particle temperature over all simulations; grandmean
$\bar{T}_{p,i}$	Mean particle temperature of simulation i
$T_{p,i,j}$	Temperature of particle j of simulation i
u	Activation function, ANN
v_p	Particle velocity
w	Normal vector of approximated hyperplane g, SVM
w_i	Firing strength of the i-th rule, ANFIS
$\overline{w}_i$	Normalized firing strength, ANFIS
$w_{k1},\ w_{k2}, \dots,\ w_{km}$	Neuron weights, ANN
X	Input vector of original data, k-NN
x	Input, ANFIS
x_p	Particle x-coordinate
$x_1,\ x_2, \dots,\ x_m$	Neuron inputs, ANN
Y	Input vector to be classified, k-NN
y	Input, ANFIS
y_k	Neuron output, ANN
z_p	Particle z-coordinate
α_i, α_i^*	Lagrange multipliers, SVM
$\phi(x)$	Mapping function, SVM
ε	Upper error bound, SVM
ξ_i, ξ_i^*	Slack variables, SVM
Ω	Input variable space, SVM
$\widetilde{\Omega}$	Feature space, SVM
γ	Kernel scale, SVM
a_i	Premise parameter of the i-th rule, ANFIS
ρ	Particle density
$\mu(x)$	Membership function, ANFIS

In der Schriftenreihe Oberflächentechnik des Instituts für Oberflächentechnik der RWTH Aachen sind bisher erschienen:

Band 1: Seemann, Klaus: Vorhersage von Prozess- und Schichtcharakteristiken beim atmosphärischen Plasmaspritzen mittels statistischer Modelle und neuronaler Netze

Band 2: Parco, Maria: Thermische Beschichtung von Leichtbaulegierungen aus Magnesium zum Verschleiß- und Korrosionsschutz

Band 3: Bobzin, K. (Hrsg.): Oberflächentechnik Jahrbuch 2004/2005

Band 4: Bobzin, K. (Hrsg.): 1. Aachener Oberflächentechnik Kolloquium 2006

Band 5: Nickel, Reimo: Die beschichtungsprozessabhängige Materialmodellierung von EB-PVD- und APS-Wärmedämmschichten

Band 6: Ernst, Felix: Qualitätskontrolle auf Basis optischer Prozessdiagnostik und neuronaler Netze beim Thermischen Spritzen

Band 7: Maes, Michel: Gepulste Abscheidung von (Cr,Al)N PVD-Niedertemperaturschichtsystemen für Hochleistungsbauteile

Band 8: Bobzin, K. (Hrsg.): 2. Aachener Oberflächentechnik Kolloquium 2007

Band 9: Hurevich, Vitalii: Einfluss einer Verschleißschutzschicht bei Skalierung des Bohrprozesses in den Mikrobereich

Band 10: Zwick, Jochen: Herstellung und Charakterisierung oxiddispersionsverstärkter Pulver für das Thermische Spritzen

Band 11: Comenares de Piñero, Carmen Leonor: Entwicklung nanostrukturierter PVD-Schichtsysteme für Zerspanung und Kaltumformung durch Einsatz der Pulstechnologie

Band 12: Bobzin, K. (Hrsg.): 3. Aachener Oberflächentechnik Kolloquium 2008

Band 13: Bagcivan, Nazlim: Entwicklung von EB-PVD-Wärmedämmschichten auf Lanthanzirkonatbasis und gesputterten Oxidationsschutzschichten für den Einsatz auf intermetallischen Ni-Basislegierungen

Band 14: Richardt, Katharina: Eigenschaften und Potentiale Atmosphärischer Plasmaspritzsysteme

Band 15: Bobzin, K. (Hrsg.): 4. Aachener Oberflächentechnik Kolloquium 2009

Band 16: Meeß, Rudolf: Entwicklung von Mikrowälzführungen

Band 17: Bobzin, K. (Hrsg.): 5. Aachener Oberflächentechnik Kolloquium 2010

Band 18: Immich, Heinrich Philipp: Maßgeschneiderte oxidische und nitridische PVD-Werkstoffverbunde für metallische Werkzeuge in der Stahlformgebung

Band 19: Rojas Yoris,Yelena: Entwicklung von Lotwerkstoffen zum Vakuumlöten von Nickel- und Titanaluminiden

Band 20: Stephan Bolz: Abscheidung nanostrukturierter Verschleißschutzschichten für Zerspanwerkzeuge mittels Kathodenzerstäubung

Band 21: Daniel Parkot: Simulative und plasmadiagnostische Untersuchungen des Magnetron Sputterns

Band 22: Stefania Ferrara: Entwicklung von Weichaktivloten und Transient-Liquid-Phase-Lotsystemen für Mikrolötverbindungen im Bereich der Medizin und Luft- und Raumfahrt

Band 23: Bobzin, K. (Hrsg.): 6. Aachener Oberflächentechnik Kolloquium 2011

Band 24: Nils Kopp: Reactive Air Brazing

Band 25: Mara Ewering: Synthese, thermische Stabilität und tribologisches Verhalten nanokristalliner gamma-Al_2O_3-Schichten für die Zerspanung

Band 26: Kirsten Bobzin (Hrsg.): 7. Aachener Oberflächentechnik Kolloquium 2012

Band 27: Konstantinos-Dionysios Bouzakis, Kirsten Bobzin, Berend Denkena, Marion Merklein (Eds.): Proceedings of the 10th International Conference The "A" Coatings 2013

Band 28: Thomas Warda: Thermisch gespritzte eisenbasierte Feinstpulverschicht-systeme für Verschleiß- und Korrosionsschutzanwendungen

Band 29: Sebastian Theiß: Analyse gepulster Hochleistungsplasmen zur Entwicklung neuartiger PVD-Beschichtungen für die Kunststoffverarbeitung

Band 30: Marcel Pascal Schäfer: Modellierung, Simulation und Optimierung von kerosinbetriebenen HVOF-Beschichtungssystemen

Band 31: Sabrina Michelle Puidokas: Design of Highly Stressed Brazed Joints

Band 32: Kirsten Bobzin (Hrsg.): 8. Aachener Oberflächentechnik Kolloquium 2013

Band 33: Hasan Koray Yilmaz: Untersuchung der Einflussgrößen auf das Reibverhalten von Kohlenstoffschichten in geschmierten Tribosystemen

Band 34: Raphael Weiß: Entwicklung und Untersuchung mehrlagiger PVD-Kohlenstoff-schichten als Schutz vor tribologischer und korrosiver Beanspruchung

Band 35: Ivica Petković: Modellierung und Simulation als Werkzeug zur Verbesserung des APS-Prozesses mittels Mehrlichtbogen-Plasmagenerator

Band 36: Markus Brühl: Elektromagnetische Eigenschaften von thermisch gespritzten ferromagnetischen Schichten

Band 37: Kirsten Bobzin (Hrsg.): 9. Aachener Oberflächentechnik Kolloquium 2014

Band 38: Tobias Münstermann: Synthese, Charakterisierung und Qualifizierung von MSIP-Edelmetallbeschichtungen für das Präzisionsblankpressen von Glas

Band 39: Marc-Manuel Matz: Lichtbogendrahtspritzen zur Armierung der ersten Kolbennut für moderne Verbrennungsmotoren

Band 40: Thomas Schläfer: Entwicklung von Verfahren zur Bestimmung der Haftzugfestigkeit von thermisch gespritzten Zylinderlaufbahnen

Band 41: Baycan Yildirim: Mehrlagige EB-PVD-Wärmedämmschichten auf Basis von Seltenerdoxiden

Band 42: Kirsten Bobzin (Hrsg.): 10. Aachener Oberflächentechnik Kolloquium 2015

Band 43: Ricardo Henrique Brugnara: Hochtemperaturaktive HPPMS-Verschleißschutzschichten durch Bildung reibmindernder Magnéli-Phasen im System (Cr,Al,X)N

Band 44: Mehmet Öte: Understanding Multi-Arc Plasma Spraying

Band 45: Martin Hilaire Djoufack: Tribological Evaluation of Hydrogenated a-C:H and Hydrogen-free ta-C Diamond-like Carbon Coatings in Diesel Lubricated Model Tests

Band 46: Leander Schramm: Development of a Robust Cylinder Bore Coating Process and Investigation of Different Feedstock Materials

Band 47: Kirsten Bobzin (Hrsg.): 11. Aachener Oberflächentechnik Kolloquium 2016

Band 48: Tobias Brögelmann: Reibungsreduzierung durch gradierte diamantähnliche Kohlenstoffschichten a-C:H:Zr und a-C:H:Ti in EHD-Kontakten des Automobilantriebsstrangs

Band 49: Christiane Schulz: Thermisch gespritzte ZnMgAl-Schichten als Korrosionsschutz in chloridhaltiger Atmosphäre

Band 50: Thomas Frederik Linke: Entwicklung eines thermisch gespritzten Oxidationsschutzsystems zur Erhöhung der Lebensdauer von γ-Titanaluminiden

Band 51: Kirsten Bobzin (Hrsg.): 12. Aachener Oberflächentechnik Kolloquium 2017

Band 52: Serhan Bastürk: Oxidische und sulfidische HPPMS-Beschichtungen für den Einsatz in der Zerspan- und Umformtechnik

Band 53: Stefanie Wiesner: Einfluss der Ag-Basislote auf das Alterungsverhalten reaktiv gelöteter Verbunde aus Keramik und Metall

Band 54: Kirsten Bobzin (Hrsg.): 13. Aachener Oberflächentechnik Kolloquium 2018

Band 55: Mostafa Arghavani: Elastic-Plastic Deformation and Cracking Behavior of Thin Hard Chromium-Based Coatings

Band 56: Martin Gottfried Engels: Korrelation von Plasma- und Schichteigenschaften bei der reaktiven Plasmasynthese von Hartstoffschichten

Band 57: Xifang Liao: Metallisierung von Kunststoffbauteilen mittels In-Mold-Metal-Spraying

Band 58: Martin Andreas Knoch: Korrosionsverhalten thermisch gespritzter ZnAl15-Korrosionsschutzschichten

Band 59: Kirsten Bobzin (Hrsg.): 14. Aachener Oberflächentechnik Kolloquium 2019

Band 60: Nathan C. Kruppe: Entwicklung hybrider PVD-Prozesse zur Abscheidung nanostrukturierter, oxinitridischer Hartstoffschichten

Band 61: Jan Sommer: HVAF-gespritzte FeCr25B5-Beschichtungen für den Verschleiß- und Korrosionsschutz

Band 62: Tiancheng Liang: Schichtentwicklung zum Oxidationsschutz von Titanaluminiden mittels HS-PVD

Band 63: Christian Kalscheuer: Entwicklung triboaktiver (Cr,Al,X)N-Beschichtungen für den Einsatz auf Maschinenelementen

Band 64: Matthias Thiex: Wechselwirkungen zwischen gradierten diamantähnlichen Kohlenstoffschichten und additivierten Schmierstoffen

Band 65: Tim Denis Stefan Königstein: Eisenbasierte, teilamorphe Hochleistungsbeschichtungen

Band 66: Mona Naderi: Nitride and Oxynitride High Performance PVD Hard Coatings with Laser-processed Surfaces

Band 67: Martin Welters: Potenzial der High-Speed Physical Vapour Deposition Technologie zur Abscheidung oxidischer Werkzeugbeschichtungen

Band 68: Leonid Gerdt: Beschichtungen für das Druckgießen von stoffschlüssigen Hybridbauteilen aus Aluminiumguss und Stahlblech

Band 69: Wolfgang Maximilian Wietheger: Maßgeschneiderte Gleitlagerbeschichtungen für hochbelastete Lagerstellen durch Thermisches Spritzen

Band 70: Ilkin Alkhasli: Multiscale Modelling of Plasma Spraying

Band 71: Kirsten Bobzin (Hrsg.): 15. Aachener Oberflächentechnik Kolloquium 2021

Band 72: Julian Hebing: Ti-Impfen von Ni-Basisloten zur Steigerung der Präzision im Lötgut

Band 73: Kirsten Bobzin (Hrsg.): 16. Aachener Oberflächentechnik Kolloquium 2022

Band 74: Seyed Ruhollah Dokhanchi: Towards Digital Shadow in Plasma Spraying

Atmospheric Plasma Spraying (APS) is a versatile coating technology, which offers a broad range of functional features. Deposition efficiency (DE) is a major performance measure in APS, which is determined by dozens of intrinsic and extrinsic influencing factors. Because of the nonlinear and complicated interdependencies of the contributing variables, enhancing DE has always been a challenging task in the process development of APS. Hence, employing an ensemble of computer-aided methods is inevitable to understand and control these correlations in such a complex coating technology. The concept of the so-called Digital Shadow combines domain-specific models with data-driven techniques of Artificial Intelligence (AI), inferred by autonomous agents to create a sufficiently accurate image of the production process including all relevant data. This dissertation is devoted to the development of the primary steps towards a Digital Shadow in APS with the ultimate goal of improving the process efficiency.

Modern AI methods, namely Support Vector Machine (SVM) and Adaptive Neuro-Fuzzy Inference System (ANFIS), were used in this work to predict DE. For this purpose, both simulation and experimental data from the entire process chain of APS were employed to train the AI models, and combine them in the frame of an expert system. These data include process parameters, in-flight particle properties and DE on the substrate.

The developed expert system consists of two subsystems: one for predicting in-flight particle properties from process parameters using SVM technique and another for predicting DE from particle properties using ANFIS. To tackle the problem of insufficient data for training the aforementioned AI models two approaches were pursued: 1) A method was developed for in situ determination of spatially resolved deposition efficiencies on the substrate, namely Local Deposition Efficiency (LDE). By using LDE, sufficient amount of data for learning algorithms could be generated, while providing that much data for ex situ measurements of global DE and their corresponding particle properties would be impractical. 2) Simulation data for the in-flight particle properties were generated by using the simulation models of the plasma jet already developed at IOT. The combination of these two strategies provided the aggregated and purpose driven data sets required for a Digital Shadow in APS. The developed expert system can be used as a tool to adjust the process parameters to produce sustainable and cost-effective coatings, and subsequently improves the integration of coating process into production chain.

ISBN 978-3-8440-9268-4

9 783844 092684

SHAKER VERLAG